Durham University

Durham E-Theses

Interactions of 5 GeV/c positive pions in hydrogen

Bhuiyan, Zahirul Islam

How to cite:

Bhuiyan, Zahirul Islam (1967) *Interactions of 5 GeV/c positive pions in hydrogen*, Durham theses, Durham University. Available at Durham E-Theses Online: http://etheses.dur.ac.uk/8818/

Use policy

The full-text may be used and/or reproduced, and given to third parties in any format or medium, without prior permission or charge, for personal research or study, educational, or not-for-profit purposes provided that:

- a full bibliographic reference is made to the original source
- a link is made to the metadata record in Durham E-Theses
- the full-text is not changed in any way

The full-text must not be sold in any format or medium without the formal permission of the copyright holders.

Please consult the full Durham E-Theses policy for further details.

Academic Support Office, The Palatine Centre, Durham University, Stockton Road, Durham, DH1 3LE
e-mail: e-theses.admin@durham.ac.uk Tel: +44 0191 334 6107
http://etheses.dur.ac.uk

TO

MY

LATE

PARENTS

INTERACTIONS OF 5 GEV/C POSITIVE PIONS IN HYDROGEN

A Thesis presented

by

Zahirul Islam Bhuiyan, M.Sc.

for the

Degree of Doctor of Philosophy

at the

University of Durham

December, 1967

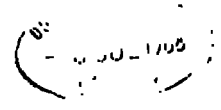

CONTENTS

PREFACE

This thesis gives an account of some of the work carried out by the author whilst at the University of Durham. The work has been carried out by the High Energy Physics Group of Durham University in collaboration with similar groups from the Universities of Bonn, Nijmegen, Paris (E.P.), Turin and Strasbourg.

The work concerns the interactions of 5 Gev/c positive pions in hydrogen and it has been divided as follows:-

(a) Six prong interactions

(b) Strange particle events

(c) Four prong interactions

(d) Two prong interactions.

The author has taken part in the first three sections of this work, in particular parts (b) and (c), and it is these parts which are described in this thesis. The author has been concerned with all stages of the analysis of the events and the investigation of the results. Specific contributions from his colleagues have been indicated.

LIST OF TABLES

LIST OF FIGURES

Chapter 1

Chapter 2

Chapter 3

Chapter 4

INTRODUCTION

Modern accelerators have provided high energy beams of particles to produce collisions with nuclear matter. The detection of these collisions in the bubble chamber and their analysis by advanced computer techniques have made great contributions to the understanding of strong interactions.

During the last few years the interactions of pi mesons with protons in hydrogen bubble chambers have been studied in a number of experiments, notably the π^+P collisions at the incident pion momenta of 4 GeV/c (A-B-B-B-H-L-M Collaboration, 1965) and 8 Gev/c (A-B-C Collaboration, 1964). The aim of the present experiment (5 GeV/c π^+P) has been to study the interactions more fully in an experiment of high statistics. The study of the four-prong events and the two-prong V^o events (with at least one visible V^o decay) which are the subject matter of this thesis is based on a sample of about 24000 and 1011 measured events.

In Chapter 1 a review is given of inelastic collisions with particular reference to some previous experiments on pion-proton interactions. The theoretical models which have been proposed to interpret the interaction mechanisms are discussed.

The second and third chapters contain a description of the beam and the bubble chamber as used in this experiment and the methods used to analyse the four-prong events.

Results of the observation of resonances in the four-prong channels are described in chapter 4.

Finally, the analysis of the two-prong V^{o} events are presented in chapter 5.

There is a short conclusion.

CHAPTER 1

A Review of Inelastic Collisions

1.1 Interaction Cross-sections

The collisions between pions and protons at existing accelerator energies often result in the production of a multiplicity of secondary particles. Their numbers are usually in the range of 2-4 but these may extend up to 8 at current energies. Despite the increase in multiplicity (i.e. opening of new reaction channels) with energy the total and elastic reaction cross-sections in πP collisions tend to be constant as shown in figures 1 and 2. Consequently the relative contribution of high multiplicity interactions increases with energy. However at 5 Gev (this experiment) this contribution is small.

The great majority of these secondary particles are pions. The cross-section for the production of K mesons and hyperons in πP collisions is only a small fraction of the total production cross-section. In the 8 Gev/c $\pi^+ P$ experiment (Brandt et al, 1966) it is found that the total cross-section for the production of the various strange particles is only about 12% of the total production cross-section. In the present experiment the fraction of events with one or two visible V^0 decays is about 2% of the total number of events. Figure 3 shows a plot of the cross-sections for the production of strange particles in πP collisions at various incident momenta of the pion.

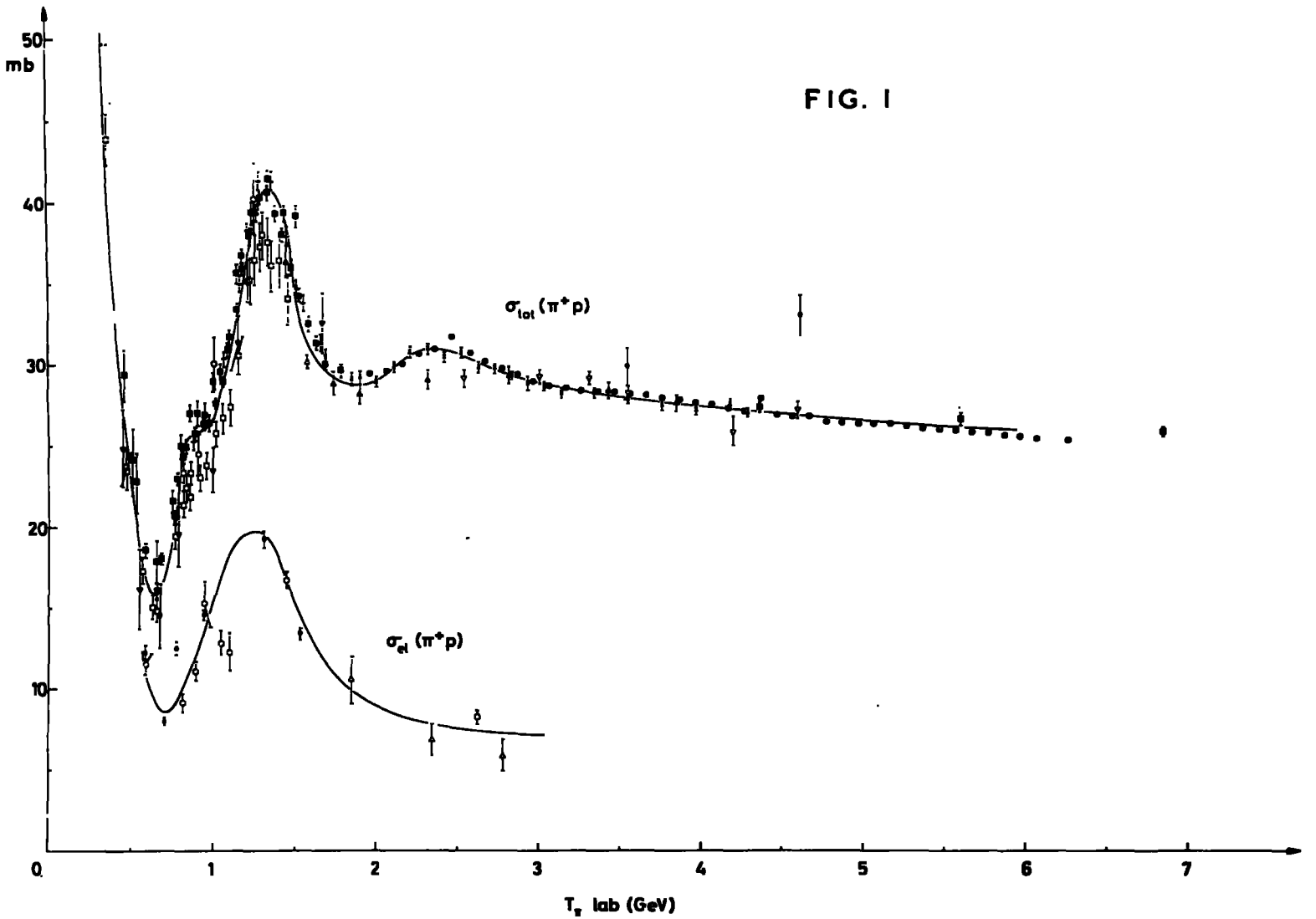
mb
50
40
30
20
10
0
1
2
3
4
5
6
7
$\sigma_{tot}(\pi^+p)$
$\sigma_{el}(\pi^+p)$
T_π lab (GeV)

FIG. 1

FIG. 2

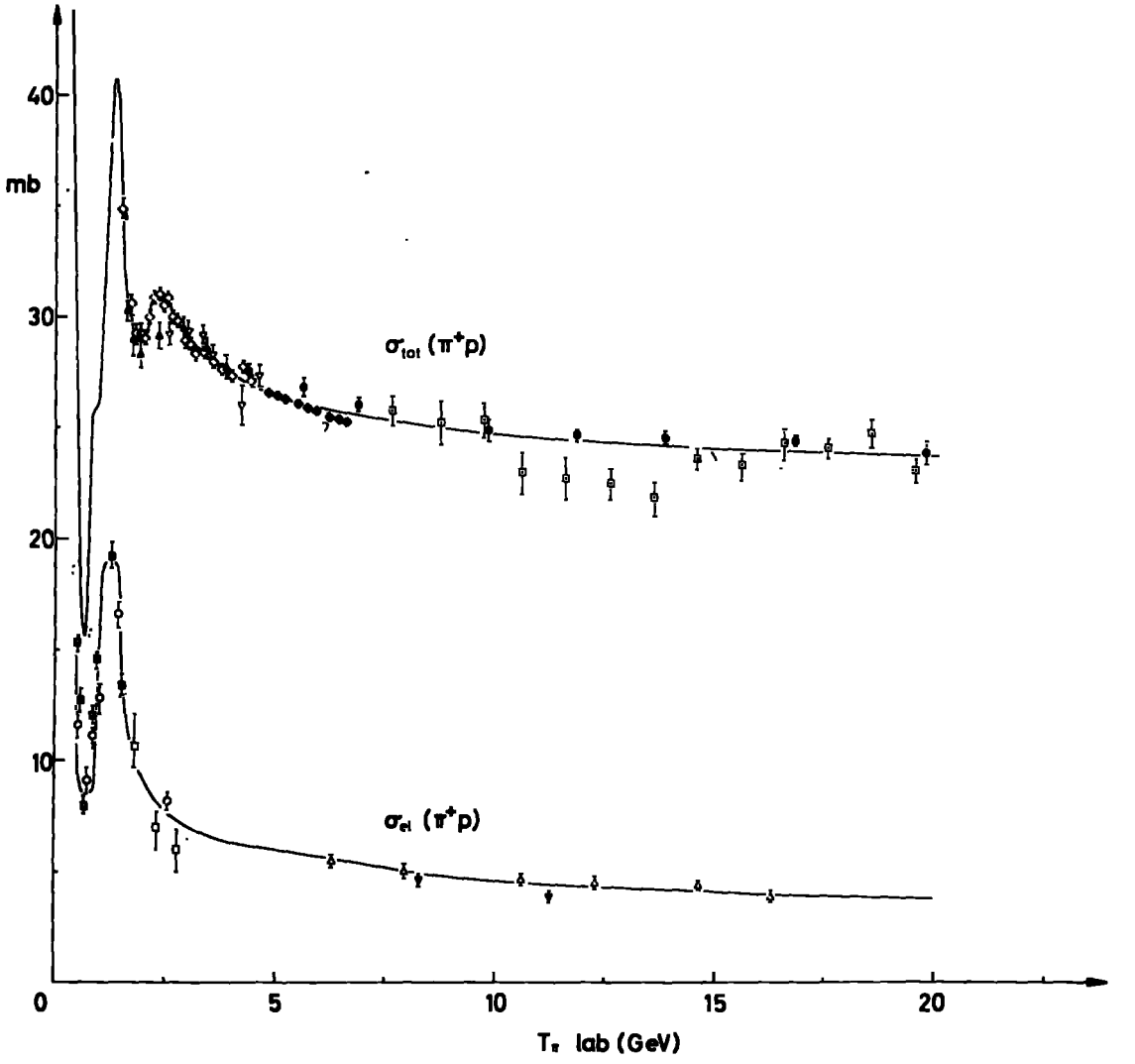

FIG. 3

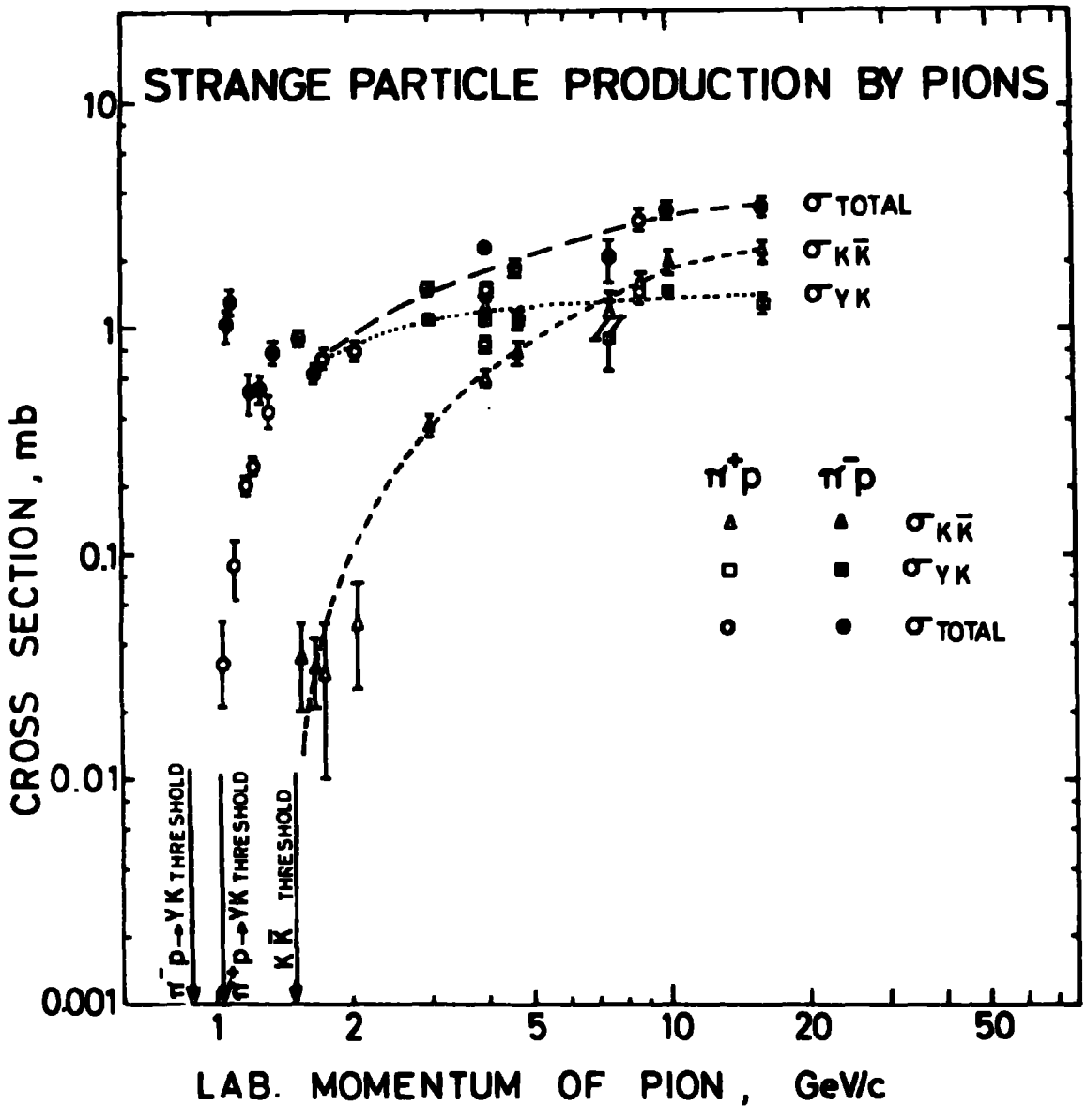
STRANGE PARTICLE PRODUCTION BY PIONS
CROSS SECTION, mb
LAB. MOMENTUM OF PION, GeV/c
10
1
0.1
0.01
0.001
1
2
5
10
20
50
σ TOTAL
σ KK̄
σ YK
π⁺p
π⁻p
σ KK̄
σ YK
σ TOTAL
π⁻p→YK THRESHOLD
π⁺p→YK THRESHOLD
KK̄ THRESHOLD

1.2 Resonances

A prominent feature in the final states of the interactions is the presence of mesonic and baryonic resonances such as the ρ, ω, η, K^*, N^*, Y^* and others. These are unstable with lifetimes so short ($\sim 10^{-22}$ sec) that they appear to decay at the point of production.

Prior to the bubble chamber, nucleonic isobars such as the $N^*(1236)$ and $N^*(1686)$ were detected in total cross-section measurements for πP collisions. Large enhancements as seen in figure 1 were recognised as due to resonances. Besides giving the indication of a structure (i.e. presence of resonances) the total cross-section measurements for π^+P and π^-P collisions also allowed the determination of the isospin of the nucleonic resonances. At high energies the height of the enhancements above the background decreases and the width increases (figure 2) so that in total cross-section measurements the resonances tend to be lost in the background.

With the bubble chamber techniques resonances are detected by the Kinematical correlations in their decay products which are the observed secondary particles of the interactions. In the majority of the cases the reaction proceeds by the production of a resonance in association with other secondary particles. However, sometimes the entire reaction takes place through the production of two resonances only, "quasi two body" which leads to simpler interpretation of the reaction mechanism.

1.3 Quasi Two Body States

During the last few years it has been observed that the high energy interactions frequently produce quasi two body states or resonances which then decay into the observed secondary particles. The cross-section for the production of these quasi two body states decreases with increasing energy due to the increasing number of secondary particles. Thus in K^+P interactions, the fraction of quasi two body states which is very high at lower energies decreases to about 25% of the total inelastic cross-section when the incident K^+ momentum rises to 5 GeV/c. Similarly in the 8 GeV/c π^+P interactions the fraction of quasi two body states is about 8% of the total inelastic events while in the 11 GeV/c π^-P interactions, the fraction falls to about 5% (Morrison, 1966). These estimates tend to be underestimated at higher energies due to the difficulties of recognising new resonances.

However, if one looks at a certain reaction channel the fraction of two-body states are found to be very high. For example, in the 8 GeV/c π^+P interaction in the channel

$$\pi^+P \rightarrow P\pi^+\pi^+\pi^-$$

where the production of N^{*++}, ρ, f^o, A_1 and A_2 have been reported (Aachen-Berlin-Cern Collaboration, 1964), the fraction of quasi two body states is found to be as high as 50%.

1.4 Interaction models

The secondary particles of high energy collisions have given rise to complex theoretical problems regarding their production mechanism and final state behaviour. High multiplicity interactions with six or more particles in the final states suggest that a good working model might be the statistical model. On the other hand, since these particles are frequently produced through intermediate resonances the quasi two body states might be equally important. In fact, the production of quasi two body states has provided new theoretical approaches on simpler lines to some aspects of high energy interactions and techniques have been developed to interpret these reactions in terms of a number of theoretical models. None of these models, however, can be said to satisfy completely every aspect of experimental observations, each model has its own area of success.

In the following sections summaries are given of the several models of interactions.

(i) The statistical model

The statistical model was first introduced by Fermi (1950) to describe multipion production in nucleon-nucleon collisions. It is a general description of the production mechanism in that the two incident particles are assumed to interact strongly in a small volume so as to form an intermediate state which decays into particles of various kinds and depending on the available energy

gives rise to a large number of final states. Each of the final states can be arrived at in a large number of different ways in a statistical manner. The cross-section σ for any final state f from an initial state i is related to the matrix element M_{fi} by

$$\sigma \propto |M_{fi}|^2 \; F$$

where F is the phase space integral. The matrix elements M_{fi} contain all the unknown dynamical effects pertaining to the production process. The simplest assumption made is that M_{fi} is a constant determined by the total energy E of the system and is independent of the individual momenta of the final state particles. Under this assumption, the cross-section, the individual momenta of the particles and many other features of the interaction are determined by the phase space factor F alone.

The statistical model which predicts isotropic angular distributions of the secondary particles gives a reliable description of high multiplicity interactions and of 'central collision' processes which are characterised by a large momentum transfer to the proton, and it is observed that as the number of produced pions increases the angular distributions approach more towards isotropy (Bartke, 1966). The model becomes unrealistic in the description of peripheral collision processes.

(ii) The Peripheral Model

An important feature of πP and KP collisions in the energy range 1 to 8 Gev is the observation that the secondary particles produced in an appreciable fraction of the events are emitted strongly forwards or backwards in the centre of mass system. This feature is more frequent in single pion production processes. In multipion production processes this feature becomes less apparent as the pion multiplicity increases and the forward-backward collimation of the secondary particles is observed mostly through the production of quasi two body states. All these production processes are characterised by a low momentum transfer to the target nucleon and are described in terms of a peripheral nature of the collision between the incident meson and the pion cloud surrounding the nucleon. The process is described by the Feynman diagram shown in figure 4(A). Here, the incident particles a and b interact with each other by the exchange of a virtual particle e in the Yukawa potential field. Referring to the above diagram, the square of the four-momentum transfer, Δ^2 (= -t) between c and a or between d and b is given by

$$\Delta^2 = -(\underline{p}_c - \underline{p}_a)^2 = -(\underline{p}_d - \underline{p}_b)^2$$
$$= -(m_c^2 + m_a^2) + E_c E_a - 2\vec{P}_c\vec{P}_a \cos\theta^*$$

where $\underline{p}_i$, $\vec{P}_i$, E_i and m_i are the four-momentum, three momentum, energy and mass of the particle or particle group i and θ^* is the production angle. The momentum transfer Δ^2 can be interpreted as the negative square of the virtual mass of the exchanged particle e. In the

FIG. 4. FEYNMAN DIAGRAMS

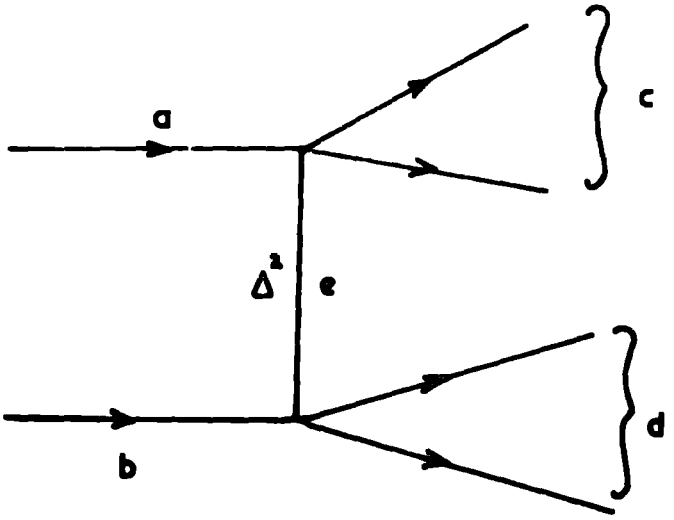

A) Simple peripheral model

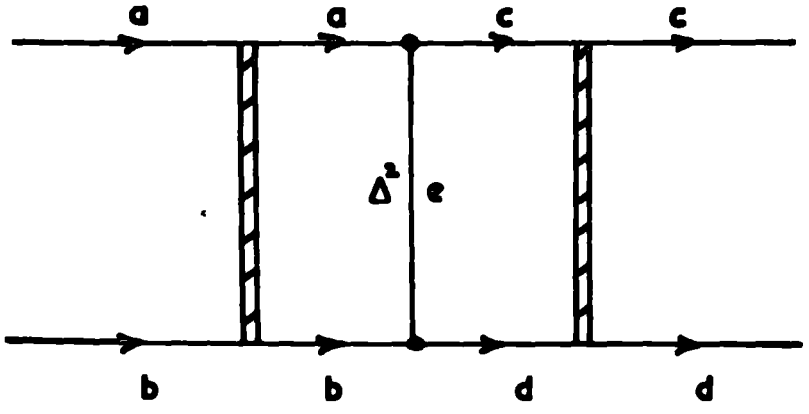

B) Peripheral model with absorption

physical region Δ^2 is positive and the exchanged particle is 'off the mass-shell'.

The matrix element for this type of production process is given by

$$M = M_I \ (\Delta^2, m_c) \ \frac{1}{\Delta^2 + m_e^2} \ M_{II} \ (\Delta^2, m_d)$$

where M_I and M_{II} are the vertex functions at the vertices I and II, and m_e is the mass of the exchanged particle. The structure of a vertex function depends on the coupling of the three particles meeting at the vertex. The square of the matrix element M gives the differential cross-section. For example, the differential cross-section for one pion exchange (OPE) for the reaction $\pi P \rightarrow \rho P$ is found to have the following form (Jackson, 1965),

$$\frac{d\sigma}{d\Delta^2} = \frac{\pi}{4 m_\rho^2 m_n^2 p^2} \cdot \frac{g^2}{4\pi} \cdot \frac{G^2}{4\pi} \cdot \frac{\Delta^2[(m_\rho - m_n)^2 + \Delta^2][(m_\pi + m_\rho)^2 + \Delta^2]}{(\Delta^2 + m_\pi^2)^2}$$

where m_π, m_ρ, m_n are the masses of the pion, the ρ meson and the nucleon respectively, p is the incident pion momentum in the laboratory, $\frac{g^2}{4\pi}$ and $\frac{G^2}{4\pi}$ are the coupling constants for the mesonic and baryon vertices respectively. The dominance of small momentum transfers in peripheral processes comes largely from the propagator $\frac{1}{(\Delta^2 + m_e^2)^2}$.

In π-P and KP collisions where a single pion is produced, the OPE model has been extensively used to describe the observed peripheralism. In such cases the process may be regarded as a collision between two spinless particles. The angular distribution

of scattering in the C.M. of the pair of mesons leads to conclusions about J^P of the di meson states involved in the collision. The angular distribution uniquely determines the angular momentum states. For pure states the angular distributions are isotropic for $J = 0$, $\text{Cos}^2\theta$ for $J = 1$ and $(3\ \text{Cos}^2\theta - 1)^2$ for $J = 2$ where θ is the angle between identical ingoing and outgoing mesons in the centre of mass of the resonance. Parity is determined from the relation $P = (-1)^J$.

More recently the peripheral model has been applied to quasi two body reactions in which more than one pion is produced. In such processes, heavier exchange particles like the ρ, K and ω are often introduced, called generally as the One Meson Exchange process (O.M.E.). Because of the spins of these particles, the assumptions entering into the analysis introduces complications in that the numerator of the production cross-section has an increasing function of Δ^2 which in most cases completely masks the effect of the propagator, $\frac{1}{(\Delta^2 + m_e^2)^2}$ which favours small momentum transfers, (Svensson, 1965). The result is that at high momentum transfer the cross-section does not fall to the level of experimental distributions.

Attempts have been made to seek a way out of this defect by introducing empirical form factors which are functions of Δ^2 to produce the necessary damping in the cross-section. For example in a number of one-pion exchange reactions at different energies,

the following form factor given by Amaldi and Sellari (1964) gives good agreement between theory and experiment in Δ^2 distributions:

$$F(\Delta^2) = \frac{0.72}{1 + \frac{\Delta^2+\mu^2}{4.73\mu^2}} + \frac{0.28}{1 + \left(\frac{\Delta^2+\mu^2}{32\mu^2}\right)^2}$$

μ = pion mass, so that $F(-\mu^2) = 1$.

At present there is a lack of reliable theory to calculate such form factors and the parameters are more or less determined by comparison with experiment - a procedure which does not make them energy independent.

(iii) The Absorption Model

The draw-backs of the form factor approach in the simple peripheral model have given rise to the Absorptive Peripheral Model which may be regarded as a refinement of the former, to produce the necessary collimation to small production angles.

The qualitative aspect of the model is that in the high energy collision of the particles a and b there are many inelastic open channels which compete with each other. As a result any particular production process such as the quasi two body states is reduced in frequency by the presence of other absorptive channels. The absorptive effect takes place mainly through the suppression of channels with lower angular momentum states, the suppression being greater for smaller impact parameters, since

$$\hbar^2 \ell(\ell + 1) = (Pb)^2$$

where ℓ is the angular momentum, b is the impact parameter and P is the C.M.S. momentum of the incident particles. This effect is not taken into account in the simple peripheral model which thus fails to account for the observed over-peripheralism in the experimental distributions.

The theoretical approach towards the suppression of low partial waves has been formulated in terms of the modified Feynman diagram shown in figure 4(B).

The absorptive effects are taken into account by the interactions U_i and U_f which represent elastic scattering of the particles before and after the exchange mechanism. The suppression of the low partial waves in the cross-section is introduced by making a Distorted Wave Born Approximation (DWBA) to the above diagram, i.e. by writing

$$< \lambda_e \lambda_d | T(J) | \lambda_a \lambda_b > = e^{i\delta_J^-} < \lambda_c \lambda_d | B(J) | \lambda_a \lambda_b > e^{i\delta_J^+}$$

In this equation T(J) is the transition matrix element, λ_i's are the helicities of the appropriate particles, B(J) is the Born term for the J-th partial wave projection of the T matrix element. The quantity $<\lambda_c \lambda_d | B(J) | \lambda_a \lambda_b>$ is the partial wave amplitude as calculated from the simple OME Model. δ_J^+ and δ_J^- are the phase shifts for the elastic scattering in the initial and final states. For small J the exponentials are small which give the desired suppression of the low partial waves.

For the determination of the phase shifts one assumes the elastic scattering to be purely diffractive which is produced by a

partially absorbing disc of radius R and absorptivity A. The result of this mode of approach gives the following relations: (Svensson, 1965)

$$\frac{d\sigma_{el}}{dt} = \frac{\sigma_{tot}^2}{16\pi} \exp\left(\frac{R^2}{4}t\right)$$

and $$\exp(2i\delta_J^{\pm}) = 1 - 2A_{\pm} \exp(-\gamma_{\pm}(J-\tfrac{1}{2})^2)$$

where $$A = \frac{\sigma_{tot}}{2\pi R^2}, \quad \gamma = \frac{2}{R^2 q^2}$$

Here q is the C.M.S. momentum of either of the particles and σ_{tot} and σ_{el} are the total and elastic cross-sections. The parameters R and A for the elastic scattering in the initial state can be directly determined from experiment. However, the same parameters for the final state elastic scattering which involves unstable particles are not available and as such can only be determined by comparison with experiment. In general, rough agreement has been obtained by taking the following values for the final state scattering process: $2A_- \simeq 1$ and $R_- \simeq 1.3\ R_+$ (Svensson, 1965).

The absorption model which brings about the necessary damping in the $\frac{d\sigma}{dt}$ distribution for large t, also retains the essential features of the simple peripheral model for small t values. In the energy range of a few Gev, the absorption model has given a remarkably good description of many quasi two body reactions. One particular aspect of its success has been in predicting the parameters of decay

Fig.5

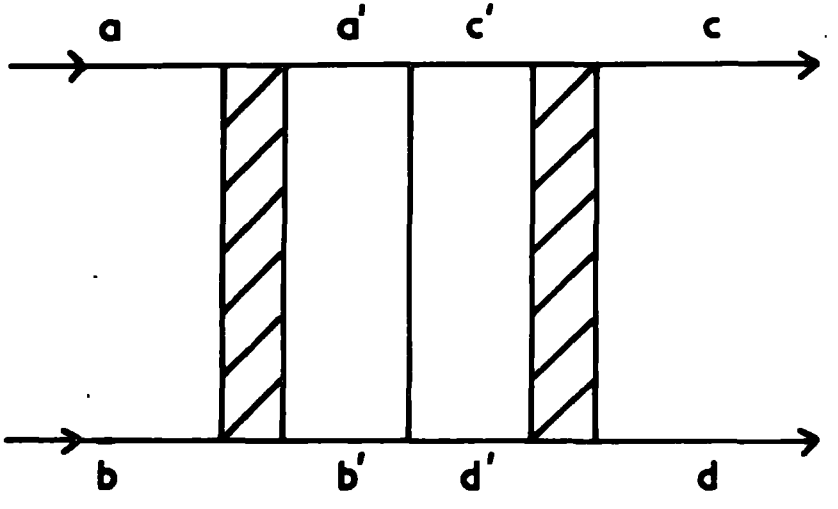

OME diagram for inelastic corrections in the initial and final states.

angular distributions (density matrices) for some of the resonances. For example, in the 8 Gev/c π^+P interactions, the predictions of the model were found to be in reasonable agreement for the channels $\pi^+P \rightarrow P\rho^+$ and $\pi^+P \rightarrow N^{*++}\rho^0$ which can proceed by pion exchange (Aachen-Berlin-CERN Collaboration, 1965).

But the usefulness of the model seems to depend on the type of the particle that is allowed to be exchanged. For vector meson exchange the absorption model displays the same energy dependence as the unmodified peripheral model; that is, the calculated cross-section diverges with energy which is in contradiction to the experimental behaviour.

Suggestions have been made to bring further refinements in the absorption model by including absorptive corrections in the inelastic scattering as shown in figure 5.

The formalism of such a process has been developed (Lichtenberg and Williams 1965) but its experimental applications are as yet unknown.

(iv) The Regge Pole Model

The theoretical development of the Regge Pole Model started with the observation at CERN by Cocconi et al., (1961) that in high energy Proton-Proton elastic scattering the diffraction peak of the $\frac{d\sigma}{dt}$ distributions narrowed logarithmically with increasing centre of mass energy S. It was found that the experimental distributions could be expressed in the form

(i) $\left(\frac{d\sigma}{dt}\right) / \left(\frac{d\sigma}{dt}\right)_o = e^{\gamma t}$ where γ is a function of energy only and not of t. From the Regge Pole theory the differential cross-section was predicted to have the form -

(ii) $\left(\frac{d\sigma}{dt}\right) / \left(\frac{d\sigma}{dt}\right)_o = F(t) \left(\frac{S}{S_o}\right)^{2\alpha(t)-2}$

comparing (i) and (ii) (t = constant).

(iii) $\gamma = b + c \ln S$ where b and c are constants. Equation (iii) implies a logarithmic shrinking of the diffraction peak and the experimental results were consistent with this behaviour within the moderately large errors.

Now the original work of Regge was to regard the angular momentum ℓ as a complex variable and to introduce the idea of poles in the complex angular momentum plane. In the scattering of two spinless particles, the scattering amplitude T(E, Cos θ) which is written in an expansion series

$$T(E, \cos\theta) = \sum_{\ell=0}^{\infty} (2\ell + 1) P_\ell (\cos\theta) A(\ell, E)$$

the partial wave amplitude $A(\ell, E)$ which corresponds to physical values of ℓ = 0, 1, 2 etc., can according to the Regge theory, be interpolated as a function which has poles at variable complex values of ℓ called $\alpha(t)$, i.e. near a pole,

$$A(\ell, E) \simeq \frac{\beta(t)}{\ell - \alpha(t)} \qquad \text{Lim } \ell \to \alpha(t)$$

where $\beta(t)$ is called the residue. Near a pole the amplitude becomes very great unless $\beta(t)$

is very small and makes a very great contribution to the scattering. If now one plots the real part of $\alpha(t)$ against t, the poles (called Regge poles) become marked on this plot. If the assumption is made that the appropriate poles can be joined by a trajectory, then it is called a Regge trajectory. If the real part of $\alpha(t)$ corresponds to some physical values then it can be assumed that a particle with this particular value of $\alpha(t)$ has been exchanged provided other conservation laws are not violated for the process. The mass of the exchange particle is equal to the energy at which $\alpha(t)$ has the particular physical value. All particles, resonances excited states etc. are thus considered as poles in the Regge theory (Chew and Frautschi, 1961). The scattering in general is described in terms of the exchange of one or more trajectories. The greater the value of the real part of $\alpha(t)$ in the physical region (t = -ve), the greater is the influence of that trajectory.

In a two-body reaction of the type

$$a + b \rightarrow c + d$$

the matrix element is given by the asymptotic expression (Maor, 1966):

$$T(s, t, u) \simeq_{s\to\infty} \sum_i \left(\frac{s - u}{S_i}\right)^{\alpha_i(t)} \beta_i(t) \; \frac{1 \pm e^{-i\pi\alpha_i(t)}}{\sin \pi\alpha_i(t)}$$

where the summation is performed over all the relevant trajectories of corresponding quantum numbers and signature except spin; s, t and u are the Mandelstam variables and S_i is a normalisation mass which can be chosen conveniently.

In some recent analysis of the reactions $\pi^- P \rightarrow n\eta^o$ (Phillips and Rarita, 1965) and $\pi^- P \rightarrow n\pi^o$ (Hohler et al., 1966) the Regge pole Model has given remarkably good descriptions of $\frac{d\sigma}{dt}$ distributions. However, the model in its present form cannot predict angular correlations as the Absorption Model does. It seems there is now a need for a unified model which can reproduce the successful features of both the Absorption Model and the Regge pole Model.

1.5 Slope of $\frac{d\sigma}{dt}$ Distributions

Apart from the predictions of the different models of interactions it is found in general that in two-body reactions the $\frac{d\sigma}{dt}$ distributions for small t values can be reasonably fitted by the simple exponential

$$\frac{d\sigma}{dt} = C \; e^{at}$$

where C is a constant. The constant a is called the slope since the logarithm of $\frac{d\sigma}{dt}$ is plotted against a linear scale in t.

In the intermediate energy range from about 2 Gev to about 8 Gev it is observed that in general, the slope increases as the energy increases.

However, at a fixed energy the slopes of the different channels of inelastic two-body reactions vary considerably towards higher and lower values than the value obtained for elastic scattering. This is shown in Table 1 for the $\pi^+ P$ collision at 8 Gev/c (Morrison, 1966).

TABLE 1

Slope of Differential Cross-sections (Morrison, 1966)

Reaction	Slope $(Gev/c)^{-2}$
8 Gev/c	
$\pi^+P \rightarrow N^{*++}(1236)\ \eta$	5
$\pi^+P \rightarrow N^{*++}(1236)\ \omega$	5
$\pi^+P \rightarrow P\rho^+$	9
$\pi^+P \rightarrow N^{*++}(1236)\ \pi^o$	9
$\pi^+P \rightarrow \pi^+P$ (elastic)	10
$\pi^+P \rightarrow N^{*++}(1236)\ \rho^o$	14
$\pi^+P \rightarrow N^{*++}(1236)\ f^o$	14

The values of the slopes in the Table are given without the small statistical errors which do not effect the general features in the Table. The values of the slopes were taken over the t-range from the Kinematic limit to about 0.3 to 0.4 $(Gev/c)^2$ except for the two reactions involving η or ω meson production when the t-range from 0.2 to 0.5 $(Gev/c)^2$ was taken. It will be seen that the values of the slopes for the channels $N^{*++}\rho^o$ and $N^{*++}\omega$ at the lower energy of the present experiment i.e. at 5 Gev/c π^+P is smaller (c.f. Chapter 4) than those given in the Table. There is as yet no theoretical explanation for the values of the slopes as observed in the different channels at the same energy.

CHAPTER 2

2. Experimental Setup

2.1 The Exposure

During February, 1965, the 150 cm. British National Hydrogen Bubble Chamber was exposed to a beam of positive pi mesons of momentum 5 GeV/c at the Proton Synchrotron at C.E.R.N., Geneva. About 150,000 pictures were taken over a period of three weeks. The film was initially divided between five collaborating laboratories - Bonn - Durham - Ecole Polytechnique (Paris) - Nijmegen and Turin for analysis of six-prong events. Later, for four-prong analysis the film of Ecole Polytechnique was shared by Strasbourg and the measurements were carried out simultaneously by the six laboratories.

Descriptions of the beam and the chamber are given in the following sections.

2.2 The Beam

The beam used in this experiment, called the 02 beam, was primarily designed to produce reasonably well separated beams of kaons, protons, antiprotons and pions with momenta up to 15 GeV/c. The beam was constructed in the East Experimental area of C.E.R.N. and combined in a single channel both electrostatic and radio frequency separation. In the present experiment, however, for the production of π^+ beam at 5 GeV/c only the electrostatic separators were used because radio frequency separation was found to be more efficient at higher momenta. A description of the beam and an

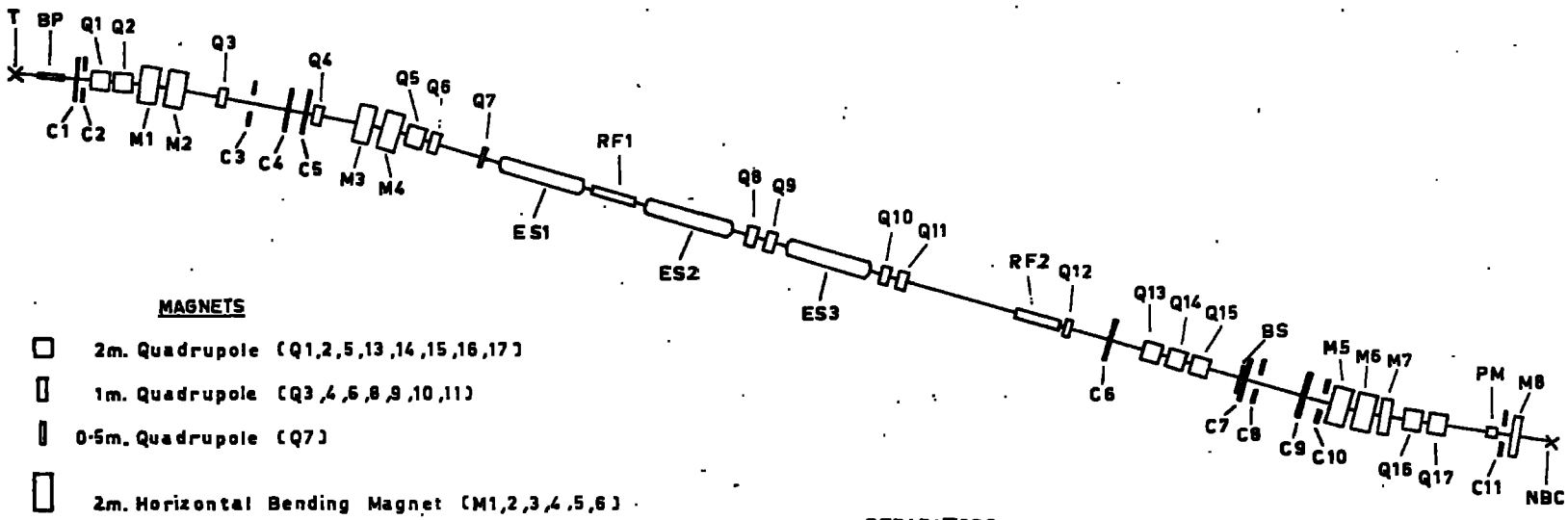

MAGNETS

- 2m. Quadrupole (Q1,2,5,13,14,15,16,17)
- 1m. Quadrupole (Q3,4,6,8,9,10,11)
- 0·5m. Quadrupole (Q7)
- 2m. Horizontal Bending Magnet (M1,2,3,4,5,6)
- 1m. Vertical Bending Magnet (M7,8)
- 1m. Pulsed Vertical Bending Magnet (PM)

SEPARATORS

- Electrostatic Separator (ES1,2,3)
- Radiofrequency Separator (RF1,2)

COLLIMATORS

- Horizontal Collimator (C2,3,8,10,11)
- Vertical Collimator (C1,4,5,6,7,9)
- Beam Stopper (BS)

T = Target

NBC = Bubble Chamber

Fig 6 THE O_2 BEAM LAYOUT

estimate of its performance has been given by Keil and Neale (1963). Below is a short description of the beam as it was in this experiment.

Figure 6 shows the schematic layout of the beam which is about 180 metres long between the target and the bubble chamber. The particles are confined to about 5 cm. of the beam axis and to avoid multiple scattering all the collimators are in vacuum boxes. The circulating proton beam of the proton synchrotron had an energy of 25 GeV and an intensity of 5.10^{11} protons per pulse. The 02 beam received about 10% of the intensity in short bursts lasting about one millisecond. The internal target used to produce the secondary particles was Beryllium with dimensions : height 0.5 mm, width 2 mm, and length 80 mm.

The external beam was extracted at an angle of 5.1° with respect to the internal proton beam. After leaving the target the secondary particles pass through an iron pipe which shields them from the fringing effects of the magnetic field of the neighbouring P.S. magnet unit.

The large number of beam transport elements such as the quadrupoles, bending magnets and the collimators can be regarded as combination of lenses and prisms. The beam may be conveniently regarded as made up of three parts. In the first part the phase space acceptance which is the product of target area and the solid angle acceptance is determined. Here also the momentum bite is selected. In the second

part mass analysis is carried out. In the final section the phase space acceptance and the momentum bite are again re-defined and the beam is shaped for entry into the bubble chamber.

Angular acceptance from thetarget is determined in the vertical and horizontal planes by the two collimators C1 and C2 respectively. The quadrupole lens triplet Q1, Q2 and Q3 focusses the beam at the centres of Collimators C3 and C4 in the horizontal and vertical planes. The bending magnets M1, M2 produce dispersion in the horizontal image at C3 and the momentum bite is defined at this stage. The horizontal and vertical images are kept separated in order to decrease the background of muons and scattered particles. After passing through the lens Q4 the beam is again made dispersion free by the bending magnets M1 and M2.

Mass analysis is carried out from the Collimator C4 onwards up to the Collimator C6. The lens triplets Q5, Q6 and Q7 produces a parallel beam in the vertical plane, and an intermediate horizontal focus inside the electrostatic separators. Each of the separators had a plate length 9 m, plate gap 10 cm. and an electric field of 50 Kv/cm. The series of quadrupoles produces a vertical focus at C6 which is the final stage in the mass analysis.

The lens triplet Q13, Q14, Q15 refocusses the beam onto the collimators C7 and C8 and the angular acceptance is redefined at the collimator C9. The horizontal bending magnets M5, M6 and the lens doublet Q16, Q17 produces a dispersed horizontal image at the

Collimator C11. The momentum bite is redefined at this point. To obtain a vertical spread in the chamber, the lenses Q16 and Q17 produce a vertical focus which is swept across the bubble chamber. The beam is steered into the chamber by the vertical bending magnets M7 and M8.

2.3 Beam Momentum and Width

To check the values of the beam momentum and beam width an analysis was made with a sample of 4-prong events by one of the collaborating groups (Schotanus, Nijmegen Group). The events selected were unambiguous four constraint fits obtained without beam editing. From a plotted distribution of the fitted values of the beam momenta, the average value was calculated to be 4.990±.006 GeV/c, after correcting for the magnetic field in the chamber. A distribution of the measured values of the beam momenta gave an average value of 4.959±.007 Gev/c and a standard deviation of 100 Mev/c. The reason for the significant difference between the fitted and measured mean values was not clear. The observed width of 100 MeV/c was due to -

(a) multiple scattering

(b) measurement error.

The multiple scattering gives an uncertainty of about 1% in the sagitta measurement, so that the best value of the measured momentum will be uncertain by at least this amount. However, in the kinematic fitting program, Grind, a weighted average is taken of the measured

and the known mean value of the beam momentum so that the effects of measuring error are considerably reduced.

2.4 Contamination in the beam

Contamination in the beam is considered to be mainly due to muons from pion decays. As the last stage of mass analysis is carried out at the collimator C6, it is assumed that only pions decaying anywhere after C6 will have some probability of getting into the chamber; those decaying between C6 and the last collimator C11 make a negligible contribution, while the main contribution to contamination comes from decays after C11. A total of 3% is estimated to be muon contamination in the beam tracks inside the chamber. A fraction of these muons will be slower than the pions and thus diverge by more than 2 cm. over the length of the chamber. Since in counting beam tracks, these diverging ones can be sorted out, a final estimate gives $(2 \pm 1)\%$ as muon contamination in the beam.

2.5 The British National Hydrogen Bubble Chamber (B.N.H.B.C.)

The first experimental run with the chamber took place at C.E.R.N. in November, 1963. The chamber has been described in several papers, e.g. Welford, 1963 and CERN/TC/NBC 64-1. A short description is given below:-

Figure 7 shows a plan view of the chamber and its surrounding magnet. It has a useful volume, 150 cm. along the beam direction, by 45 cm. wide and 50 cm. high. The effective volume of liquid

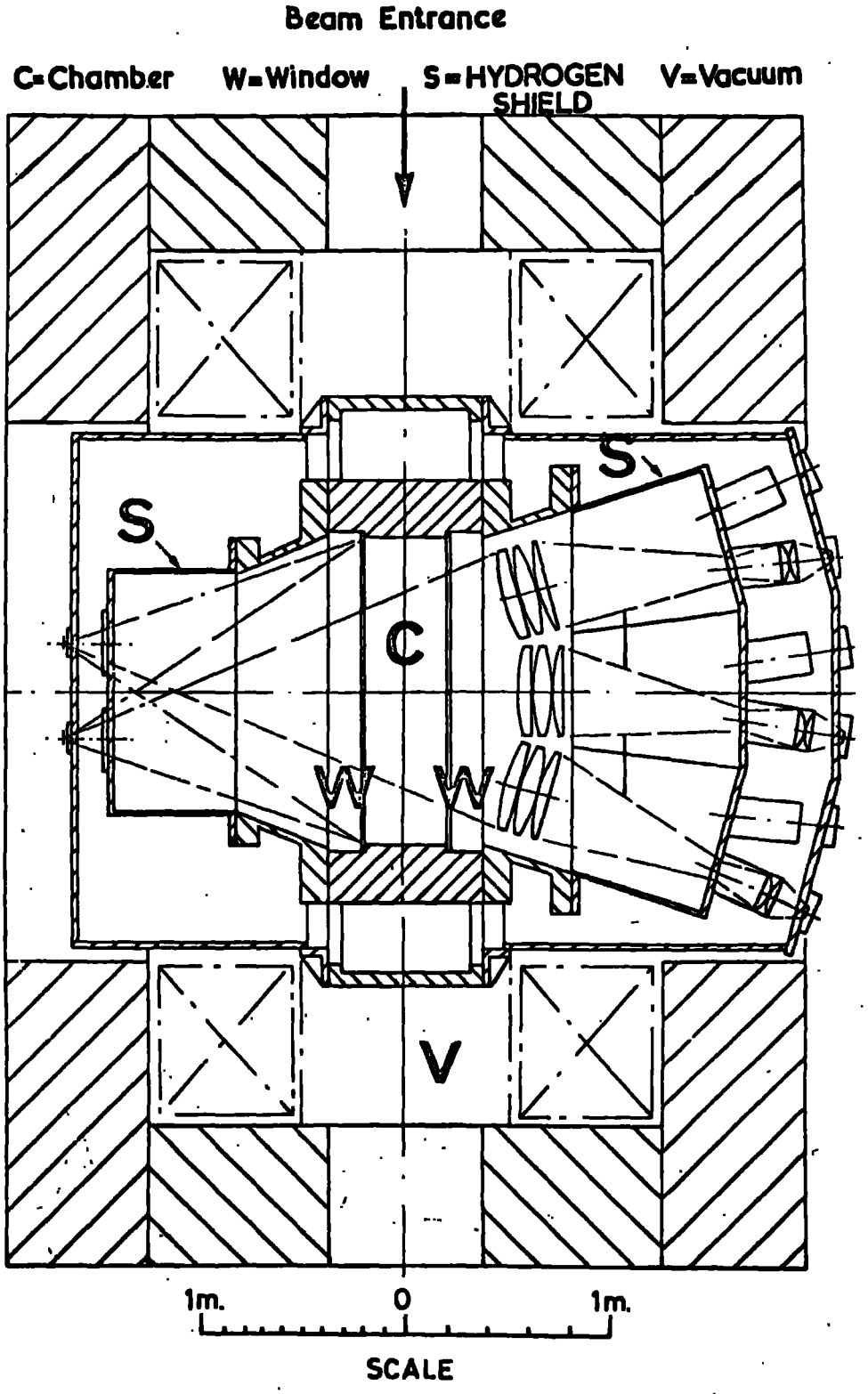

FIG. 7. PLAN VIEW OF B.N.H.B.C. SHOWING OPTICAL SYSTEM AND MAGNET.

hydrogen as seen by the three cameras is about 300 litres. The chamber body is machined from a single aluminium forging and is closed on either side by parallel glass windows 15 cm. thick. The windows are protected by hydrogen shields. The whole unit is hung inside a stainless steel vacuum tank to avoid thermal losses.

The optical system is the 'direct' or 'through illumination' type. Circular flash tubes are used to illuminate the chamber and are made to form ring images around the camera lenses by means of condenser lens systems. Only the light scattered by the bubbles can then enter the camera lenses. The chamber was photographed by an array of three cameras with parallel axes, perpendicular to the front glass. The film used was unperforated 35 mm film in 300 metre lengths. The cameras were mounted at the corners of an isosceles triangle of which the height (= base) is 480 ± .01 mm.

The Operating Cycle

The fully automatic operation of the chamber took place under the following conditions:

Operating temperature	:	$27^{\circ}K$
Upper Operating Pressure	:	$6.3\ Kg/cm^2$
Sensitive Time	:	2 milliseconds
Repetition Cycle	:	30 per minute
Bubble diameter	:	200 microns (approx.)
Bubble density for minimum ionising tracks e.g. 5 GeV/c π^+	:	10-12 bubbles per mm.

About 30 milliseconds before the particles of the beam arrived at the chamber, a signal from the proton synchrotron caused the pilot valves of the chamber to open and these in turn opened the main expansion valves, allowing the hydrogen to enter the expansion tank. The hydrogen took about 8 milliseconds to expand fully and reach the desired superheated state and at that point the beam particles arrived in the chamber. The arrival of the particles was detected by a scintillation counter which sent a secondary signal, causing the flash tubes to be pulsed $1\frac{1}{2}$ ms. afterwards. This allowed the right amount of growth of the bubbles which were then photographed before turbulence developed. Immediately after the flash the expansion valves were closed and the recompression valves were opened. The hydrogen returned to its initial state in about 10 ms. The film in the camera was also wound forward one frame and the whole cycle repeated.

2.6 Reference System in the Chamber

A set of fiduciary crosses ruled on the inner surfaces of the two windows provide the necessary reference system in the chamber. The fiduciary crosses on the light-side window have one arm longer than the other three, the crosses on the camera-side window have four equal arms. The coordinate system in the chamber is defined as a right-handed rectangular system in which the $Z = 0$ plane is the inner surface of the camera-side window, Z-axis pointing towards

the cameras, X-axis along the beam direction. The origin of the coordinate axes may be taken anywhere in this plane.

2.7 Optical Distortions

Optical distortions in the chamber were not negligible. In order to make reliable reconstruction of events possible, it was found necessary to take into account distortions due to lens, film tilt and film stretch. Kellner (1965) made a study of these effects and obtained a set of distortion coefficients for correcting film measurements. The method used by Kellner was to fit the distortions with a general polynomial of the form

$$\begin{pmatrix} x^1 \\ y^1 \end{pmatrix} = \begin{pmatrix} x \\ y \end{pmatrix} \left(1 + \alpha_1 \frac{x}{f} + \alpha_2 \frac{y}{f} + \alpha_3 \frac{xy}{f^2} + \alpha_4 \frac{x^2}{f^2} + \alpha_5 \frac{y^2}{f^2} + \alpha_6 \frac{(x^2+y^2)^2}{f^4} \right)$$

where x^1, y^1 represent co-ordinate values on the "ideal film plane" that would have been expected if the lens acted like a simple pin-hole camera. The variables x,y are the co-ordinates on the "physical film plane" - the actual image on the film when the effect of film stretch has been removed. The polynomial contains terms to account for the distortions caused by the following:-

(i) tilt of the film plane ..... $\alpha_1 \frac{x}{f} + \alpha_2 \frac{y}{f}$

(ii) spherical lens distortion .... $\alpha_4 \frac{x^2}{f^2} + \alpha_5 \frac{y^2}{f^2}$

and $\alpha_6 \frac{(x^2 + y^2)^2}{f^4}$

(iii) other non-identified causes .. $\alpha_3 \frac{(xy)}{f^2}$

The values of the co-efficients were determined by Kellner and these were incorporated in the geometry program Thresh.

2.8 Magnetic field in the chamber

The magnetic field at different points in the chamber space was accurately mapped out by the proton magnetic resonance probe method (CERN/TC/NBC 63-2). For this purpose two values of excitation current at 8,000 and 10,000 amps were used and in each case the percentage deviations of the field values with respect to the central value were determined at the intersections of a 5 cm cubic matrix. The deviations were found to be the same for both values of excitation current, the maximum being 3% at the sides of the chamber.

The magnetic field, H, at a point is given by

$$H = H_c + \frac{D}{100} H_c$$

where H_c is the central value and D is the percentage deviation at that point. The values of D were tabulated and incorporated in the fitting program in matrix form.

The central value of the magnetic field was checked by an analysis of a sample of K_1^o and Λ^o events. Using a central field value 13.54 K. Gauss, the grind computed masses of Λ^o's and K_1^o's were compared with their nominal values. The observed disagreement could be removed by reducing the central field value to 13.46 ± .03 Kilogauss which was subsequently used in the analysis of 6 and 4 prong events.

2.9 Scanning

Durham's share in the collaboration was to analyse about 30,000 pictures of 25 triads of films including one triad of no field tracks. Five of these films were rejected after a preliminary inspection on the scanning tables. The reasons for rejection were - poor quality of the pictures in one or more views due to too many tracks, faintness and fogging. Two films were partially rejected for the same reasons. Each roll had about 1,250 frames and a total of about 20,000 pictures were scanned. The no field film taken in the absence of a magnetic field in the chamber was used to test the straightness of the beam tracks against multiple scattering in the chamber. Results of measurements on no-field beam tracks have been described in section 3.9.

Scanning was done throughout by a physicist and a scanner. Figure 8 shows the fiducial volume chosen for the purpose of scanning. The volume corresponds to view 2 as seen by the camera 2, which is

FIG. 8

DIAGRAM OF FIDUCIAL VOLUME

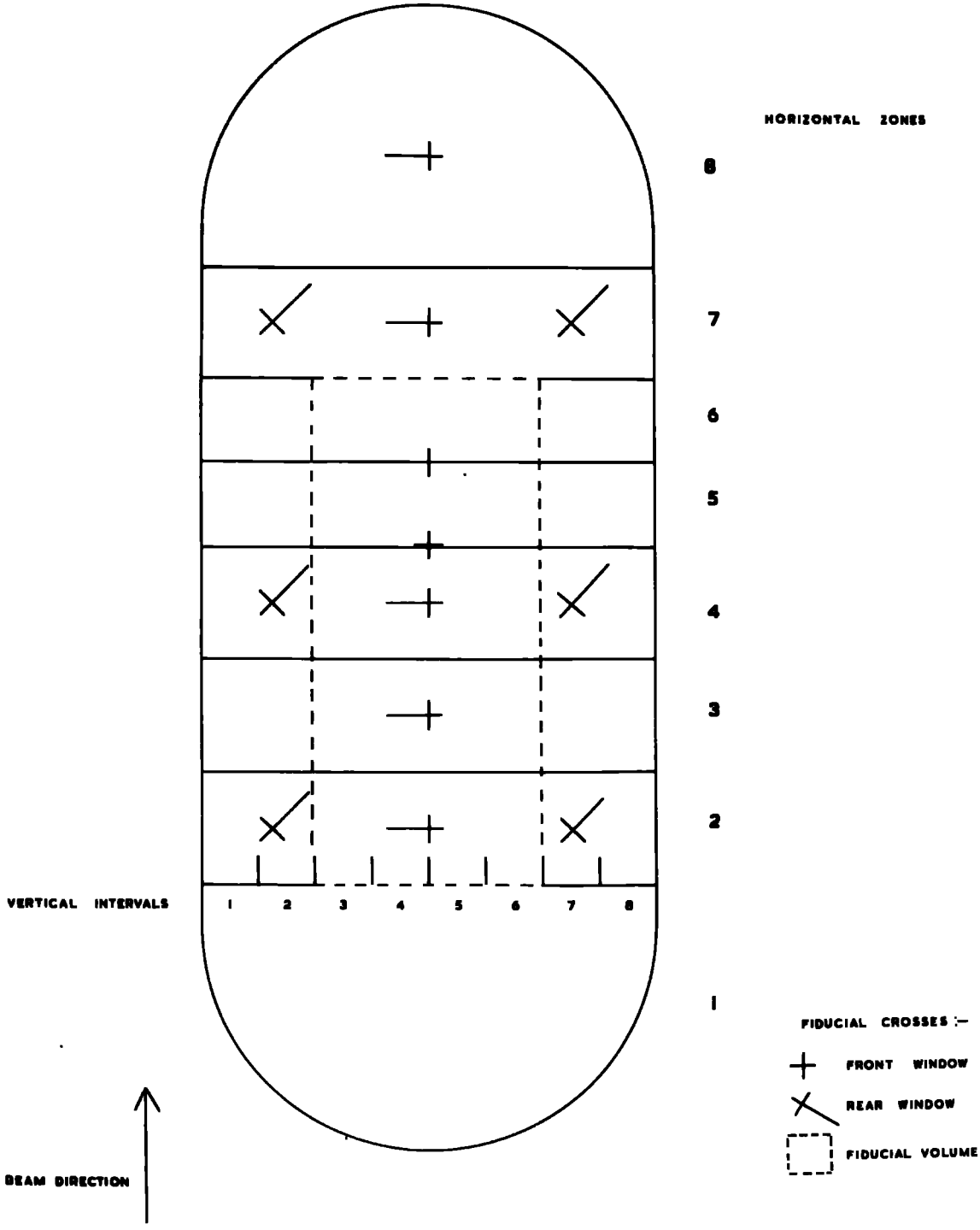

the most symmetric of all the three views. In choosing the fiducial volume, the following considerations were given; minimum loss of events, provision for good observations in all the three views, possibilities for accurate reconstruction of events by making use of the correction coefficients for optical distortion, maximum length of secondary tracks measureable for events near the boundary of the fiducial volume and facilities to observe γ's and V^{o}'s decaying inside the chamber. The fiducial volume thus chosen was approximately 54% of the volume as seen by camera 2. From a preliminary scan it was found that about 5% of the events were outside the fiducial volume.

The projected fiducial volume was divided into six vertical and six horizontal zones. The zone numbers of each event recorded during scanning indicated the location of the interaction; the first number gave the vertical position of the beam track at the beginning of the chamber and the second number gave the position of the interaction along the axis of the chamber.

An event was accepted if it was in the fiducial volume, provided that the beam track entered somewhere through the bottom edge of the fiducial volume. The films were scanned in views 1 and 2 while the third view could always be projected for checking in case of doubt. Scanning was done for all types of interactions, 2, 4, 6, 8 prongs. Information recorded on the scanning sheets were; frame number of the film, the event number in the particular frame, the zone numbers

of the event, the prong size and any secondary interaction. In addition, the following cases of interest were looked for and entries made in corresponding columns of scanning sheets:

Stopping tracks

Associated γ's and V^{o}'s

Charged decays ($V^{\pm}$, π-μ-e)

Associated electron pair.

Besides cases of flipping of tracks of an event from one view to another or an event which was not measureable because it was either too faint or had a secondary track which was too short and straight, were also noted in the remarks. Proton tracks were identified wherever possible by visual examination of ionisation density up to a momentum of about 1300 MeV/c.

2.10 Scanning Efficiency

A complete scan of all the films gave 5795 four prong events. Nine of these films were rescanned. Any discrepancy about the topology of an event in scan and rescan was resolved by a check scan. An estimate of scanning efficiency was made from the following information in Table 2.

Table 2

Scan Results of 4 Prong Events

(9 Films with double scan)

No. found in first scan	No. found in second scan	No. Common to both scans
3553	3542	3432

Average scanning efficiency = 96.9%

Estimated number of 4 prong events in the whole lot of films = 5980

In the above estimation it has been assumed that the events are missed randomly (Burhop, 1962). It is further assumed that the efficiency of a given observer is a constant quantity. These assumptions are well justified in this case because a four prong interaction is much easier to observe than a low multiplicity interaction or special type of interactions such as charged or neutral decays.

2.11 Labelling

The topology of a four prong event is described by the code 03010 which implies no V^+, three positive secondary tracks, no V^-, one negative secondary track and no V^o for the event. On each view the items of measurement are the fiducial marks, points and tracks. The measurement of each item consists of its label followed by one or more coordinate sequences. The labels are conveniently chosen in keeping with the requirements of the computer programs.

For the four prong events it was not found necessary to do any previous labelling on the scan tables. The events were labelled as they were measured by the operators. Care was taken to keep the identity of the tracks from one view to another. Information from scan tables was consulted for stopping or identified tracks.

2.12 Measurement

General

For every 4 prong event an average of 45-50 coordinate pairs (x,y) were measured in each of the three views. The coordinates were those of - four fiducial crosses, the interaction vertex and 8-9 evenly spaced points along the length of each track. In some cases, the curvature along the track of a slow particle could be seen to change significantly due to multiple scattering. For these cases care was taken to measure only that part of the track near the apex where the curvature was essentially constant. This was because the geometry program Thresh, which was used, does not take energy

loss into account, consequently accurate reconstruction of a track which is measured through an angle greater than 150° is not possible. For stopping tracks of very short range only the coordinates of the end-points were measured. The momentum of these tracks was determined in the kinematics program Grind, after a mass assignment had been made, by making use of known range-momentum data which are supplied in the title of the program. In the case of a stopping track with measureable curvature, both the end-point as well as a number of points along the track were measured. This provided two calculations to be made for the momentum, one from the curvature and the other from the range. After a check for compatibility of the two independent values, a weighted average was taken for use in the analysis programs.

2.13 Machines

Three machines were used for measuring the events. Two of the machines used the well-known technique of counting Moire fringes for digitising x and y motion. These two were designed and built within the department. The third machine was a Coventry Gauge and Tool Instrument fitted with Hilger and Watts mechanical digitiser. The machines have been described in two theses from this group (Briggs, 1966; Kitchen, 1967). The least count of each machine was 2.5 microns. A 4 prong event took, on an average, 12-15 minutes to measure in the machines.

CHAPTER 3

Analysis of the Events

3.1 Introduction

In this chapter a description is given of the processes of data analysis, identification and classification of the four prong events. In the process of data analysis the paper tape output from the measuring machines serve as the basic data for the geometrical reconstruction and kinematical fitting of the events. A chain of computer programs, Reap-Thresh-Grind-Slice-Sumx is used in the analysis. Figure 9 shows the scheme of analysis in a block diagram. Except for Reap the rest of the programs are the well-known CERN library programs which were used by each of the collaborating groups. In the analysis performed by the Durham group all computing except for Reap and Sumx was made by the IBM 7044 computer at the University of Glasgow. A short description about the main purpose of each of the programs is given below:-

3.2 Reap

The main purpose of Reap is to process the raw measurements coming from the measuring tables and prepare the input for the next program Thresh. For each event, the program reads, decodes and sorts the data relevant to it. The Reap program used in the present work was written by H. Halliwell for the Elliott 803 computer of the University of Durham. The program has the following provisions:-

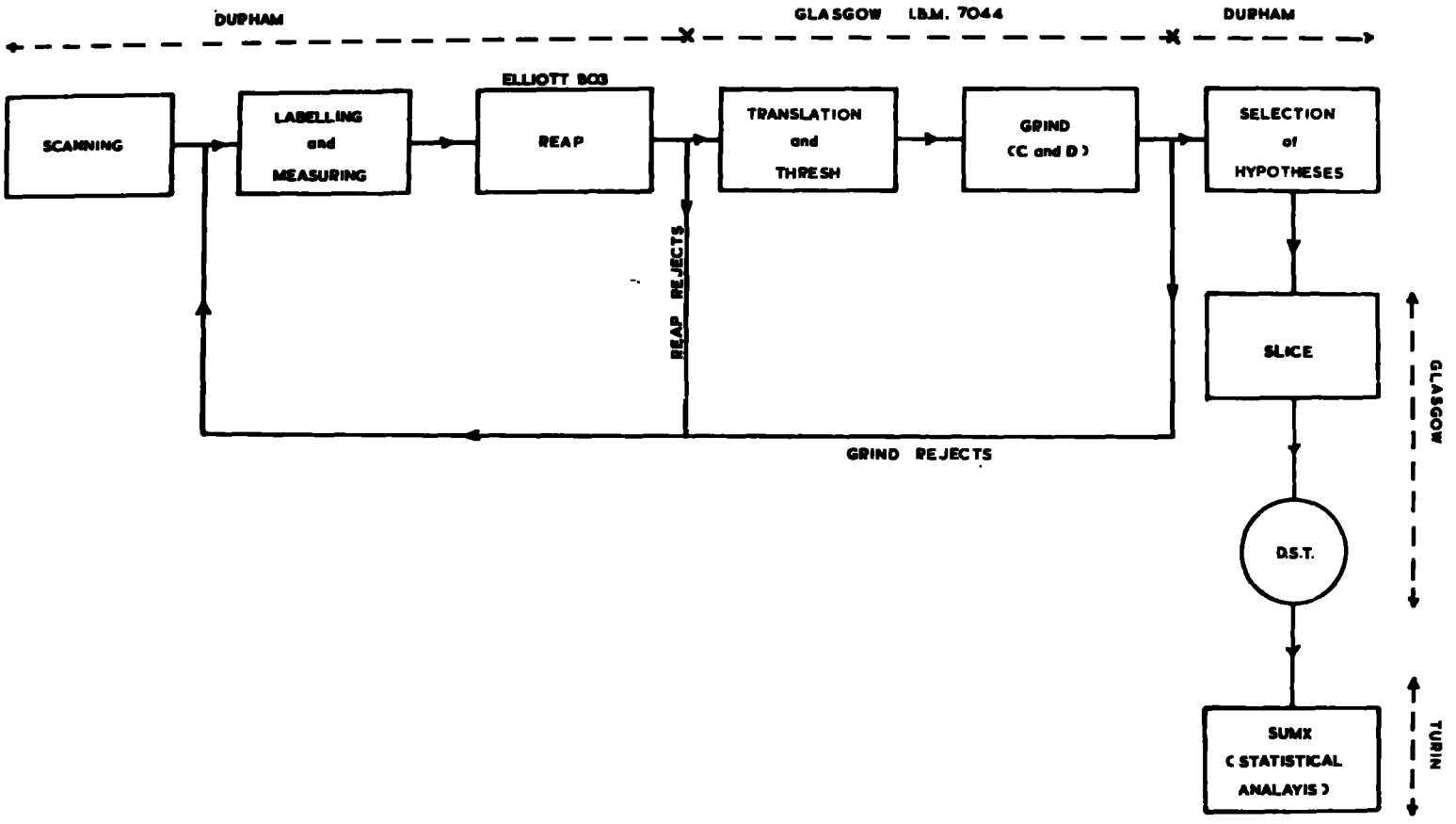

FIG. 9. SYSTEM OF DATA ANALYSIS

(i) The operator needs to punch the full length of the event title only once at the beginning of the first event; the program retains the parts of the title which are common to all other events. In this way, usually the frame number only has to be punched from event to event.

(ii) Any fault in measurement of a point or a track either due to an operator's mistake or failure in the counting system can be rectified simply by remeasuring the point or the track. This is allowed even after the completion of a view as long as the character signifying the end of the event is not punched. Also any mistake in typing the labels can be corrected by typing again; the program recognises only the last two characters as a legal label.

(iii) The program also keeps a check on the number of points measured. Thus a view is rejected if less than three fiducials have been measured. An optional check can also be made about the quality of measurements. This is done by calculating the deviations of the measured points on a track from a fitted parabola. This allows badly measured events to be detected at the earliest stage and so can be remeasured before a particular film leaves the measuring table.

The output from Reap consists of a paper tape in Ferranti code with the ordered Thresh input data and a second tape which gives a summary of the measurements.

3.3 Thresh: Reconstruction of events.

The output from Reap is processed through the geometry program Thresh. A detailed description of Thresh is given by F. Bruyant (T.C. Program Library, C.E.R.N.).

All points measured on the film have corresponding points in the chamber space. The purpose of Thresh is to find the coordinates of those points relative to the chamber reference system and to describe the whole event in space. The program is supplied with some experiment dependent quantities such as the coordinates of standard fiducial system and the cameras, characteristics of the optical media and tolerances for measurements etc. This information is entered in the title blocks of the program. The title blocks used in the present work were the same as those in the 6 prong analysis.

Spatial reconstruction of an event is done in the following way:-

The film measurements are transformed to the chamber reference system through the following stages -

(x_i, y_i)	film measurements in fringes
(X_i', Y_i')	Transformed coordinates in the z=0 reference plane in the optic axis system and in chamber units - corrected for linear distortion due to film stretch and non-orthogonality of the axis of the measuring machines.

(X, Y)	In the z=0 plane, corrected for distortions due to lens and film tilt.
(X, Y, Z)	Coordinates in chamber space.

After reconstruction, for each track Thresh gives curvature, dip angle and azimuth angle and their associated errors. The uncertainty of the track variables is due to errors of the measuring machines and contributions from Coulomb scattering. The uncertainty of coordinates measured by Durham machines is about 5 microns. This constant error was propagated through all the space reconstruction and gave the uncertainties of the derived quantities. The uncertainties due to Coulomb scattering depend on the mass of the particle. As Thresh is mass independent, the multiple scattering effects were included at a later stage.

The output from Thresh is a binary tape which served as the input for the next analysis program, Grind.

3.4 Kinematic Analysis : Grind

The geometry output from Thresh goes next into the Kinematic program Grind. The main purpose of Grind is to test the different hypotheses for possible explanation of an event by a statistical fit to the given data.

As in Thresh, a Grind Title containing information about experimental-dependent quantities was prepared by the collaboration. The Title had a number of blocks containing information about

characteristics of the incident particle beam, magnetic field matrix, the labelling scheme used, the mass hypotheses to be tested at a vertex, convergence criteria in the iterations to be performed by the program.

In its original form, Grind was too big for the IBM 7044 computer used at Glasgow. It was split into two parts, C Grind and D Grind. C Grind mainly computes the momenta for each track with the help of the magnetic field matrix given in the title and outputs a binary tape containing momenta, dip, azimuth and projected length of each track with their associated errors as well as a copy of the program titles. This binary tape is used as input to the hypothesis testing part of the program, D Grind.

The purpose of D Grind is to make mass assignments for each track according to the hypotheses list as given in the Title and to output the results of such assignments.

To describe an event completely, the momentum vector and the mass of each track at each vertex have to be known. The momentum vectors are measured for all seen tracks. If a track is too short its momentum vectors may not be completely known while for neutral particles decaying outside the chamber, these are completely unknown. The masses are not measured but usually there is only a limited number of possible values for each track.

An event must satisfy the conservation of momentum and energy. At an interaction vertex, for n outgoing particles, four constraint

equations can be written as

$$\Sigma p_x = \sum_{i}^{n} p_i \cos\lambda_i \cos\Phi_i - p \cos\lambda \cos\Phi = 0$$

$$\Sigma p_y = \sum_{i}^{n} p_i \cos\lambda_i \sin\Phi_i - p \cos\lambda \sin\Phi = 0$$

$$\Sigma p_x = \sum_{i}^{n} p_i \sin\lambda_i - p \sin\lambda = 0$$

$$\Sigma E = \sum_{i}^{n} \sqrt{p_i^2 + m_i^2} - \left(\sqrt{p^2 + m^2} + M\right) = 0$$

where p, λ, Φ and m are the momentum, dip, azimuth and mass the incident particle (in units C = 1), p_i, λ_i, Φ_i and m_i are those of the outgoing particles and M is the mass of the target particle. As the distributions of the errors on p is not Gaussian, values of 1/p are used instead in the computations.

The raw measurements of the momentum vectors will not fulfill these constraints exactly. Slight adjustments of the measured quantities must be made for this purpose. The best values of the variables are found by an iterative procedure for a least squares fit.

The fitted values must necessarily be small. The extent to which the measured variables are adjusted is given by the well-known expression:

$$\chi^2 = \sum \frac{(\text{fitted variable} - \text{measured variable})^2}{\text{variance of measured variable}}$$

Obviously, the fitted values are those which satisfy the constraint equations and also minimise the expression for χ^2.

For no neutral particle in the final state, there is no unknown quantity and all the variables are constrained through all the four equations. One has four degrees of freedom and the fit obtained is called a 'four constraint fit'.

If one neutral particle with an assigned mass is assumed to be present in the final state, then the first three equations are used to solve for the three unknown parameters, (p, λ and Φ) of of this particle, leaving the fourth equation for a constraint fit. One has only one degree of freedom in this case and the fit obtained is called a 'one constraint fit'. Obviously for two or more neutral particles in the final state, the number of unknowns becomes more than the number of constraint equations. No fit can be obtained in such cases.

As the number of hypotheses to be treated per event can be very large (16 in the present case), D Grind makes an early check on the hypotheses which are tenable and abandons those which are untenable on the basis of some non-convergence criteria. This is done to save Computer time as the arithmetic involved per hypothesis is very large.

For each event processed, D Grind gives a complete copy of the event parameters and the geometry input to the program. For each hypotheses which has been successfully fitted, it gives the masses involved in the hypothesis, the fitted and unfitted values of the momenta, dip and azimuthal angle. Also output are the errors on

the fitted and unfitted quantities and the number of iterations performed to obtain the fit. For each fit, the value of χ^2 and the number of degrees of freedom are also printed so that the goodness of a fit may be judged.

Finally, at the end of calculations on an event, a summary bank is printed which gives the details of all fits attempted, whether successful or not and the reason for failure otherwise. The summary bank also gives for each hypothesis attempted, the momentum vectors of a missing track, the missing energy and the missing mass squared with their associated errors.

In addition to the paper print output, the D Grind results are written on a binary tape. For each successful hypothesis, D Grind produces a slice card which keeps a record of the event number and the hypothesis number. These slice cards and the binary tape are subsequently used for further processing in the next program SLICE. However, before going over to Slice, a Grind library tape is progressively built up with more and more events.

3.5 Slice : Pre-statistical Analysis

The result of Kinematic analysis in Grind is generally one or more interpretations of an event and for each interpretation, the mass and the track parameters of each of the outgoing particles are given with their errors and correlations.

After an interpretation of an event has been accepted on the basis of track ionisation and χ^2 cuts, the corresponding Slice card is chosen. At this stage the program SLICE is called upon to perform some physical analysis on a single event basis. The object of the program is to process the output tape from Grind and to produce a data summary tape (DST) for the next statistical program Sumx.

The DST contains the general information about an event (i.e. momenta, energies and angles) together with, for example, any effective mass values called for by the programmer.

Also SLICE will include NOFIT events on the DST if this is required provided the identities of the charged particles are known. These are supplied through the ionisation estimates made at the scanning table in conjunction with the measured momenta. Then missing masses, effective masses etc. can be determined and included for the NO FIT events.

3.6 Sumx : Statistical Analysis

The last stage in the analysis program is to extract statistical information from the large number of events processed through the earlier programs. Sumx is a computer program for analysing statistical data. The purpose of the program is to digest the information about the large number of events contained in the Data Summary Tapes and to compile this information into histograms, two-dimensional scatter

plots, lists and ordered lists or to find mean values and variances. The program has the facility to select subsets of events according to some criteria defined in control cards. Facilities are also provided for adding routines from the user when quantities not immediately available need to be computed.

3.7 Error Estimation in Thresh and Grind

Each track that is reconstructed in space has three independent variables, $1/p$ (curvature), Φ (azimuth) and λ (dip angle). The variables are conveniently chosen as the errors on these are Gaussian. After finding these track parameters for the fitted helix, thresh also calculates the errors associated with each of them. The magnitude of these errors, known as internal errors, is calculated according to the experimental lack of smoothness with which the reconstructed points define a given track.

Before an event is passed into the fitting program, severity of the internal errors is judged by comparing them against another set of errors, the external errors. These are the errors expected on a track of length L when the average measuring error on a projected sagitta is f_o. They are given by

$$\left(\Delta \frac{1}{p}\right)_{EXT} = \frac{8 f_o}{(L \cos\lambda)^2}$$

$$(\Delta\lambda)_{EXT} = 6\sqrt{\left(\cos^2\lambda + .01\right)}\, f_o/L$$

$$(\Delta\Phi)_{EXT} = \frac{4 f_o}{L \cos\lambda}$$

where f_o is related to σ, the standard error on measurement of a point and is given by $f_o = \sqrt{1.5}\,\sigma$. As the setting accuracy on a point with the IEP machines was about 2 to 3 fringes, σ was taken to be about 5 microns. Taking the magnification from the chamber to film which was of the order of $\frac{1}{15}$, the value of f_o was set at 100 microns in the analysis programs.

If the internal errors are found to be greater than 3 times the external errors, an appropriate error word is flagged against the track. For example, error words 100, 40, 20 would indicate these situations in respect of the internal errors on $1/p$, λ and Φ respectively. Besides the error word 200 would indicate that three times the external error on $1/p$ was greater than $1/p$ itself, which is likely to happen in case of a badly measured track. Other error words, 1000 and 4000 are flagged in cases of non-convergence in Thresh or fault in Thresh respectively.

The external errors (rather than internal) are used in Grind. Furthermore in the fitting procedure because of the overall constraints that are imposed, these errors are somewhat reduced.

3.8 Rejection of events

Looking at these error words one can judge the goodness of measurement for every individual event and decide whether the event is to be considered for the given interpretations or to reject it for re-measurement. In the present work, the events were sorted out for re-measurement on the basis of the following criteria which

were decided in the collaboration:

(a) Error words 20,40 or 100		: not serious unless on more than one track.
(b) " " 120(= 100 + 20)	)	: not serious if momentum
	)	<400 MeV/c
" " 140(= 100 + 40)	)	: or dip $>\|60^{\circ}\|$; otherwise,
" " 160(= 100+40+20)	)	: remeasure.
(c) " " 200		: not serious on beam track or short stopping track; others re-measure.
(d) " " 1000		: same condition as at (b)
" " >1000		: re-measure.

About 40% of the events failed in the first measurement according to the above criteria and were measured again.

3.9 The no-field film

The determination of curvature of a track is subject to errors due to measurement and multiple scattering. The errors due to these two effects are taken into account in the analysis program. In order to investigate any other unknown sources of error, measurements were made on a no-field film. On this film exposures were taken when there was no magnetic field in the chamber except for a small residual field of 4 ± 2 Gauss.

The film had about 200 frames which were scanned for any

interactions in the horizontal zones 5 and 6 (c.f. figure 8) of the fiducial volume. This provided 62 interaction vertices for which the average projected length of the beam tracks was about 40 cm. To obtain more statistics 69 additional beam tracks in different frames were selected. Each of these additional tracks had an associated delta ray which made a sharp intersection with the beam track somewhere in the said scanning zones. This point of intersection could be measured as a labelled point as an interaction vertex. Measurements were then made on both sets of the tracks as zero-prong events in all the three views. The events were reconstructed by the geometry programme Thresh. 93 of the tracks were successfully reconstructed the rest were rejected due to bad measurements.

Figure 10 shows the distribution of the curvature of the no-field beam tracks. The distribution, though compatible with errors due to measurement and multiple scattering, has a mean value significantly different from zero. This is

$$1/p = +(0.7 \pm 0.2) \times 10^{-5}\ cm^{-1}$$

which is in an opposite sense to the curvature, $-80.76 \times 10^{-5} cm^{-1}$, of the 5 GeV/c beam tracks in the magnetic field of 13.46 Kilo Gauss in the chamber. The maximum detectable momentum is therefore about 560 GeV/c. The expected curvature of the no-field 5 GeV/c beam tracks due to the residual magnetic field of the chamber is $-(2.4 \pm 1.2) \times 10^{-7} cm^{-1}$ which is only 0.02% of the curvature of the field tracks and is negligible.

FIG. 10

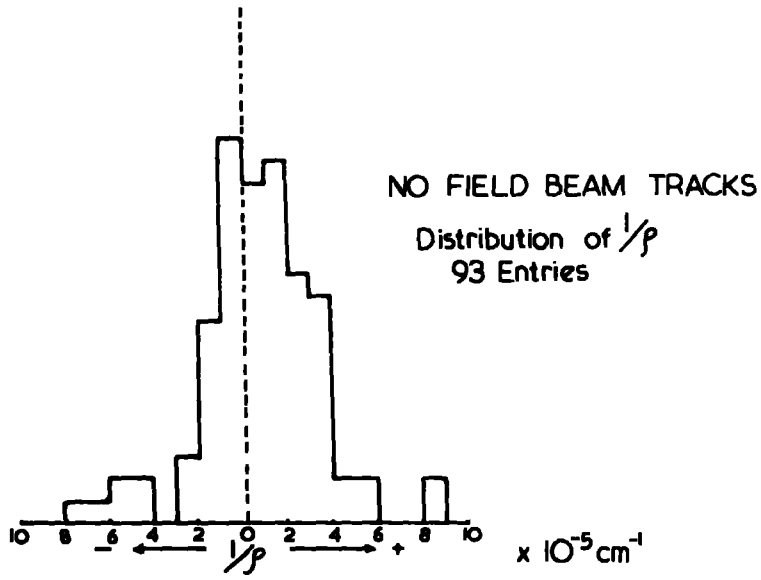
NO FIELD BEAM TRACKS
Distribution of 1/p
93 Entries
10 8 6 4 2 0 2 4 6 8 10
1/p
x 10⁻⁵cm⁻¹

FIG. 11

NO-FIELD BEAM TRACKS

DISTRIBUTIONS OF $\frac{1}{p}$ IN DIFFERENT ZONES IN THE Y DIRECTION.

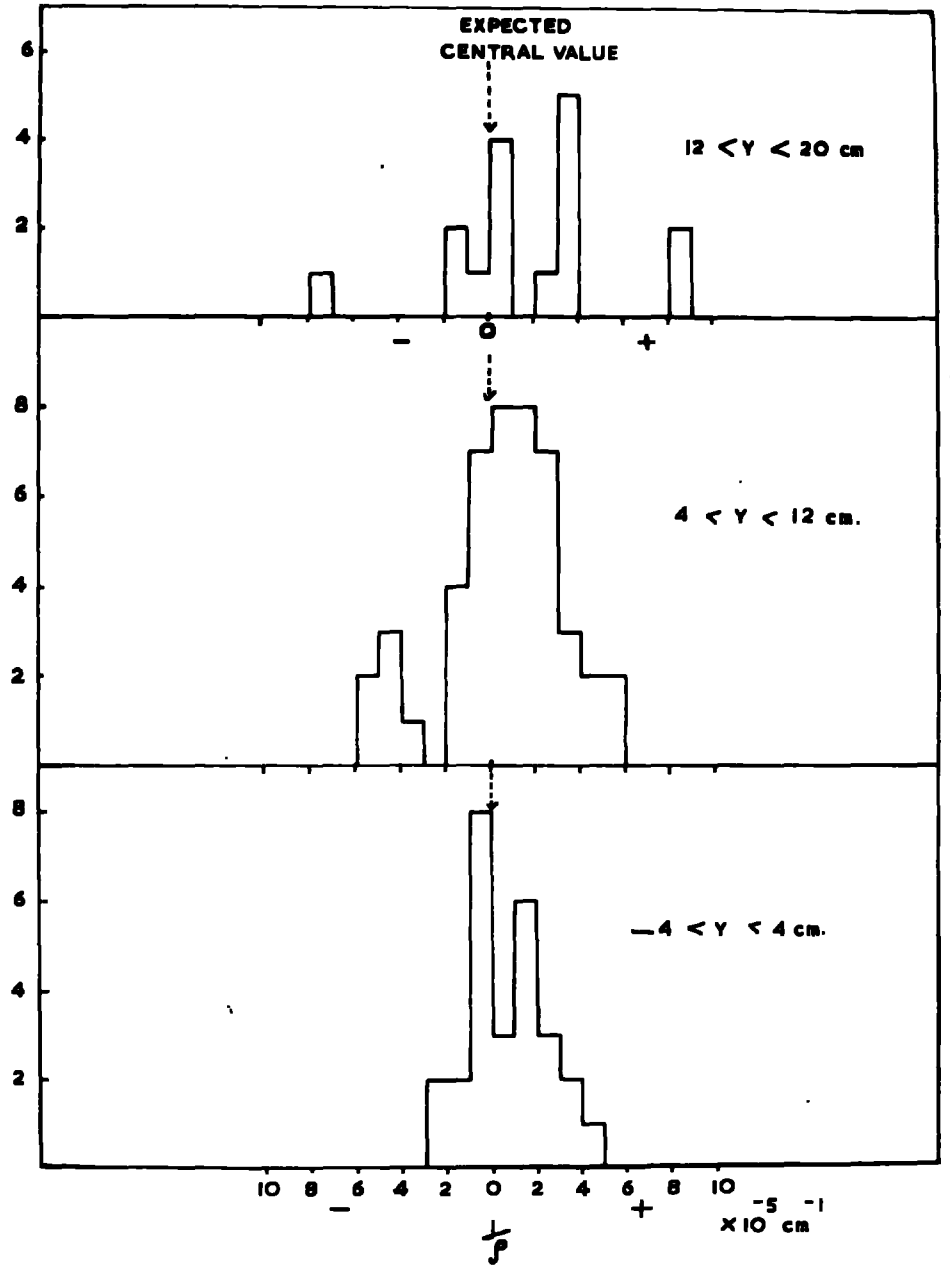

The observed curvature of the no-field tracks is a systematic error and may perhaps be attributed to the distortion of the liquid hydrogen during the expansion process in the chamber. In order to investigate any particular region of the chamber which could possibly be associated with the distortion, the chamber space was divided into three regions each of width about 8 cm along the Y direction and the tracks were grouped accordingly. The distribution of curvature (figure 11) for each group does not show any significant change from the overall mean value. It was thus concluded that there was no particular region of turbulence.

The distortion tended to reduce the curvature of the in-field beam tracks by about 0.8% which produced an over-estimation in the measured momenta of these tracks by the same amount. Grind however, used a weighted average of the beam momenta in its fitting procedure so that the effect of the distortion on the incident momentum was insignificant. In the case of the secondary tracks of a typical four-prong event, where the average momentum of a track is 1 GeV/c, the small effect of the distortion is covered up in the χ^2 fitting process, though this effect might have been reflected in the χ^2 distributions of the fitted hypotheses.

3.10 The χ^2 fit of hypotheses

Each time Grind made a successful fit the goodness of fit was indicated by chi square (χ^2). The magnitude of χ^2 depended on how big the differences between the fitted and the measured values were

(c.f. section 3.4). The value of χ^2 corresponding to a given number of degrees of freedom is converted into a probability by using the theoretical χ^2 distribution which is given by

$$f(\chi^2)\, d\chi^2 = \frac{(\chi^2)^{\frac{n}{2}-1}}{2^{n/2}\Gamma(n/2)}\, e^{-\chi^2/2}\, d\chi^2$$

where n is the number of degrees of freedom and Γ is the Gamma function.

The χ^2 values of 6 and 24 which were the upper limits chosen as criteria for selection of 1C and 4C fits correspond to probabilities of .0143 and .00005 and respectively. The χ^2 distribution for a set of events of a given constraint type should follow the corresponding theoretical distribution and deviations from this distribution would indicate wrong assignment of the errors of the input parameters.

In Figures 12 and 13 are shown the experimental χ^2 distributions for 4C and 1C fits. Both the distributions are biased towards higher values. The 4C χ^2 distribution has a mean value 1.51 instead of the expected value of 1, the deviation between the two values here, is smaller than in the case of the 4C distribution. These higher mean values in both the cases indicated that the errors of the input parameters were systematically small. Distributions showing the same high mean values of χ^2 were obtained by other members of the collaboration in the present analysis, and is probably due to an underestimate of the error f_o, on the projected sagitta which has been set at 100μ. A more realistic estimate is 125 μ. However, the use of the lower value does not introduce any significant biases.

FIG. 12

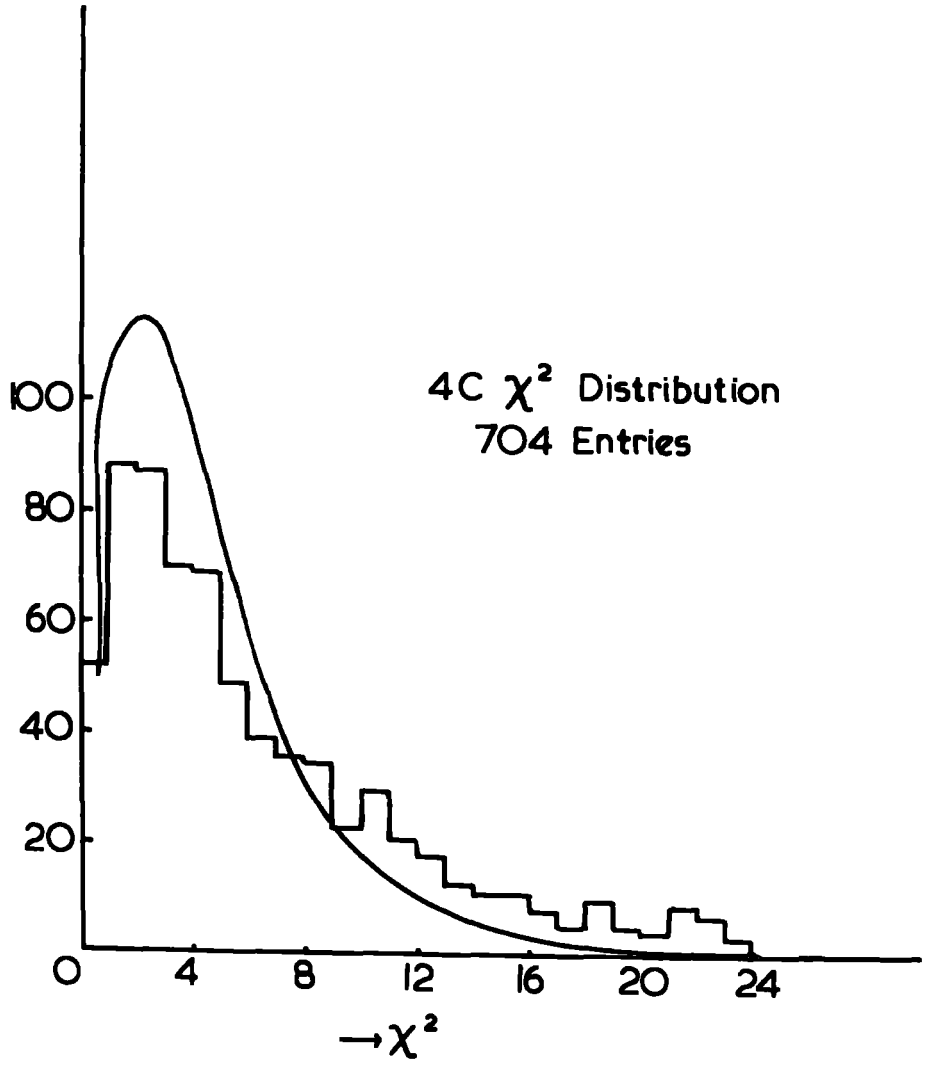
4C χ^2 Distribution
704 Entries
100
80
60
40
20
0
4
8
12
16
20
24
$\rightarrow \chi^2$

FIG. 13

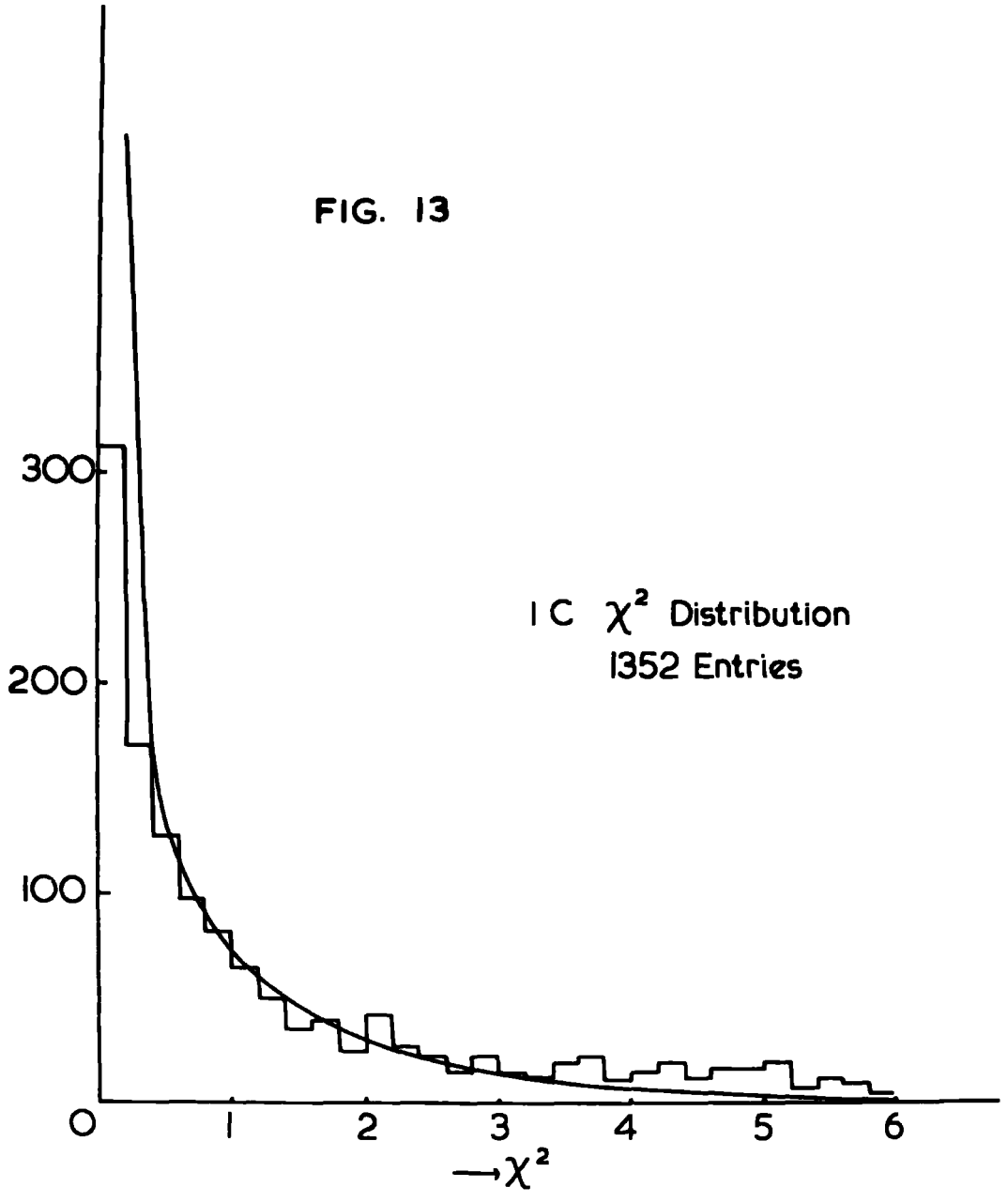

3.11 Event Identification : 4 Prong Events

The possible reaction channels for four prong events are:

$$\pi^+p \rightarrow p+\pi^++\pi^++\pi^- \quad (1)$$

$$\rightarrow p+\pi^++\pi^++\pi^-+\pi^o \quad (2)$$

$$\rightarrow \pi^++\pi^++\pi^++\pi^-+N \quad (3)$$

$$\rightarrow p+\pi^++\pi^++\pi^-+\eta^o \quad (4)$$

$$\rightarrow p+\pi^++K^++K^- \quad (5)$$

$$\rightarrow p+\pi^++\pi^++\pi^-+n\pi^o, n\geq 2 \quad (6)$$

$$\rightarrow \pi^++\pi^++\pi^++\pi^-+N+n\pi^o, n\geq 1 \quad (7)$$

Another channel of the type $\pi^++p \rightarrow p+\pi^++\pi^++\pi^-+\omega^o$ was later rejected from consideration as the missing mass spectra did not show any significant peak at the mass of the ω^o.

Events of type (6) and (7) with more than one neutral particle are classed as no fit events.

Events of type (1) and (5) are of the four constraint type and those of types (2), (3) and (4) are of the one constraint type. For these events, there were 16 possible hypotheses corresponding to proton and kaon mass assignments for the different tracks, as shown in table 3.

For each event, the printed output from Grind contained the following information:

(a) The output from C Grind which gave the coordinates of stopping points and the primary vertex as also the momentum, dip and azimuth of each track with their associated errors.

TABLE 3

Scheme of Hypotheses for the 4-prong events

Topology	Number of Constraints	Order of mass assignment	Hypothesis Number
03010	4C	$\pi^+\pi^+p\pi^-$	1
		$\pi^+p\pi^+\pi^-$	2
		$p\pi^+\pi^+\pi^-$	3
		$\pi^+K^+pK^-$	5
		$K^+\pi^+pK^-$	6
		$\pi^+pK^+K^-$	7
		$K^+p\pi^+K^-$	8
		$p\pi^+K^+K^-$	9
		$pK^+\pi^+K^-$	10
	1C	$\pi^+\pi^+p\pi^-\pi^o$	101
		$\pi^+p\pi^+\pi^-\pi^o$	102
		$p\pi^+\pi^+\pi^-\pi^o$	103
		$\pi^+\pi^+\pi^+\pi^-N$	104
		$\pi^+\pi^+p\pi^-\eta^o$	111
		$\pi^+p\pi^+\pi^-\eta^o$	112
		$p\pi^+\pi^+\pi^-\eta^o$	113
		$\pi^+\pi^+p\pi^-\omega^o$	114
		$\pi^+p\pi^+\pi^-\omega^o$	115
		$p\pi^+\pi^+\pi^-\omega^o$	116

(b) For each hypothesis tried, the fitted and unfitted values of momentum, dip and azimuth of each track with their errors, the χ^2 of the fit and the corresponding probability, the square of the missing mass and its error and also a summary bank of all the fits attempted whether successful or not.

For each event, Grind usually produced results for more than one fit, the number depended on the magnitude of the errors of measurement. Before making a final choice of the interpretations, the output from grind was compared with the film projected on the scanning table. There were two considerations to make in an event identification. One was the bubble density of the tracks and the other was the kinematical information as mentioned in (b) above.

Bubble density

Bubble density, D is defined as the number of bubbles per unit length of track normalised to minimum ionising tracks. The 5 GeV/c π^+ beam tracks ionise at minimum. Bubble density is a function of the velocity of a particle βC. For low velocities the normalised bubble density can be written as $D = \frac{1}{\beta^2}$ (Peyrou, 1960). For any mass assignment, the bubble density of a track is given by

$$D = 1 + \frac{m^2}{p^2}$$

where p = momentum and m is the assigned mass

λ is the angle of dip of the track.

For each track Grind computes the projected bubble density which is $\frac{D}{\cos\lambda}$ and offers a means of testing the correctness of a fit by

checking the computed density in the actual picture.

From a sample of fitted events, bubble densities of proton, kaon and positive pion tracks dipping at small angles ($< 30^{\circ}$), have been plotted against the fitted values of momenta (Figure 14). The graphs show that at about 1300 Mev/c of momentum, the proton ionisation is about 1.4 against the pion ionisation of 1. It was thus found possible to distinguish between the proton and pion tracks up to 1300 Mev/c. Between 1300 and 1500 Mev/c, the proton ionisation decreases to about 1.3 and depending on the picture quality it was sometimes possible to identify a proton track up to 1500 Mev/c. Above 1500 Mev/c, the proton ionisation approaches the pion ionisation and becomes indistinguishable. A pion track ionises at minimum from about 400 Mev/c while for a kaon the corresponding momentum is 700 Mev/c. The effect of dip is to make an apparent increase in ionisation and this fact was taken into consideration in deciding about tracks with appreciable dip.

About 1% of the 4 prong events were found to be $K^{+}K^{-}$ events, that is of type (5). Most of these $K^{+}K^{-}$ events were identified by the fact that the negative track had to be denser than would be the case with a negative pi meson, provided that the momentum was less than 700 Mev/c. For very slow tracks (momentum < 100 Mev/c) distinction between different particles by ionisation is not possible. These cases were decided by kinematics and the observed range of the track. The following procedure was adopted in making an event identification.

FIG. 14.

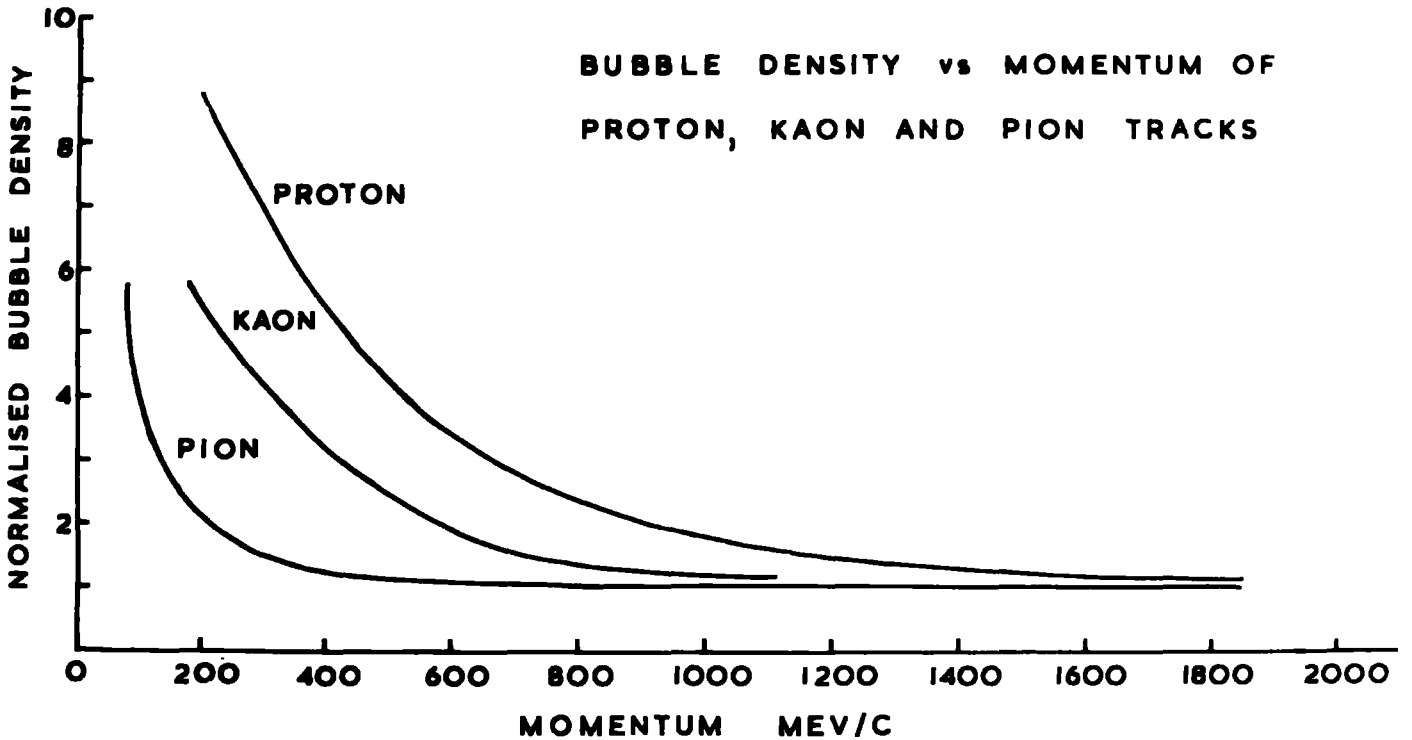
BUBBLE DENSITY vs MOMENTUM OF
PROTON, KAON AND PION TRACKS
NORMALISED BUBBLE DENSITY
10
8
6
4
2
PROTON
KAON
PION
0
200
400
600
800
1000
1200
1400
1600
1800
2000
MOMENTUM MEV/C

Looking at the picture of an event, each of the three positive tracks was weighted as either 2, 1 or 0 to make up a 'proton code' for the event; 2 for a definite proton, 1 for a possible proton and 0 for definitely not a proton. This weighting was done by visually examining the densities of the tracks against the momenta and dip angles as given in the geometry record (C Grind output passed on to D Grind). The weight 2 could be given for a sufficiently dark track if its momentum did not exceed 1300 Mev/c and provided that its dip was not too high. With the weight 2 given for any one track, the other two tracks are weighted as 0,0. In events where no definite proton could be identified by ionisation, the tracks were weighted as 1 or 0 according as the momentum was greater or less than 1300 Mev/c. Some tracks had large dip angles and this fact was taken into consideration in deciding about a proton code. Once a proton code for an event was determined only fits consistent with the code were considered and accepted if the fits also fell within the limits of Chi square. Events in which none of the attempted hypotheses agreed with the proton code were rejected as no fit events.

The percentage of events in the 4C and 1C channels selected on the basis of different codes is shown in the Table 4.

TABLE 4

Percentage of Events (according to Proton Code)

Code	4C	1C (without neutron)	1C (neutron)	no-fit
Definite proton	20.2	27.3	-	10.2
Possible proton	5.6	9.8	2.2	11.2
No proton	-	-	3.2	10.3

It can be seen that in the 4C channel there were about 4 times as many events in the 'definite proton' code as there were in the 'possible proton' code while in the 1C channel this factor was about 3. In the neutron channel about 60 per cent events were in the 'no proton' codes. No-fits were approximately in the same proportion in all the three codes. The above statistics have been taken from a sample of about 2000 events and it shows the use of a proton code in an event interpretation. The proton code can also be used with the no-fit events (c.f. Section 3.5).

The second criterion considered in selecting a hypothesis for an event was the value of chi square of the fit corresponding to the hypothesis. For the 4C fits the criterion was $\chi^2 \leq 25$ and for the 1C fits the criterion was $\chi^2 \leq 6$. These criteria were the same as used in the analysis of the 6 prong events in this experiment and also in the analysis of the 4 GeV/c π^+p interactions by the ABBHM

collaboration, 1966. No criterion for 'missing mass' was introduced at this stage of checking the Grind output on the scan table until later when the missing mass spectra were examined and appropriate cuts were applied to make a final classification of the events in the various 4C and 1C channels (c.f. Section 3.12).

In case of ambiguity between a 4C fit and a 1C fit, the 4C fit was preferentially chosen as suggested by Fake calculations (Lynch, 1962). The fraction of events in the 4C sample, chosen in this way in preference to 1C (π^0) fits, was about 15%.

3.12 Missing Mass Spectra

For each hypothesis Grind computed the square of the missing mass MM^2 which is given by (in units C= 1)

$$MM^2 = (\Delta E)^2 - (\Delta p)^2$$

where E and p are the missing energy and the missing momentum. For a 1C fit MM^2 is expected to correspond, within errors, to the square of the mass of the neutral particle (π^0, n, η^0) entering into a hypothesis while for the 4C fits, the distribution of MM^2 should have a sharp peak centred around zero.

4C Fits

The 4C fits constituted about 23% of the total events including about 1% of the K^+K^- events, i.e. of type (5). Figure 15(a) shows the distribution of the square of the missing mass corresponding to these events. The distribution shows a small shift from zero which

Fig. 15

Distribution of MM^2 (Durham Data)

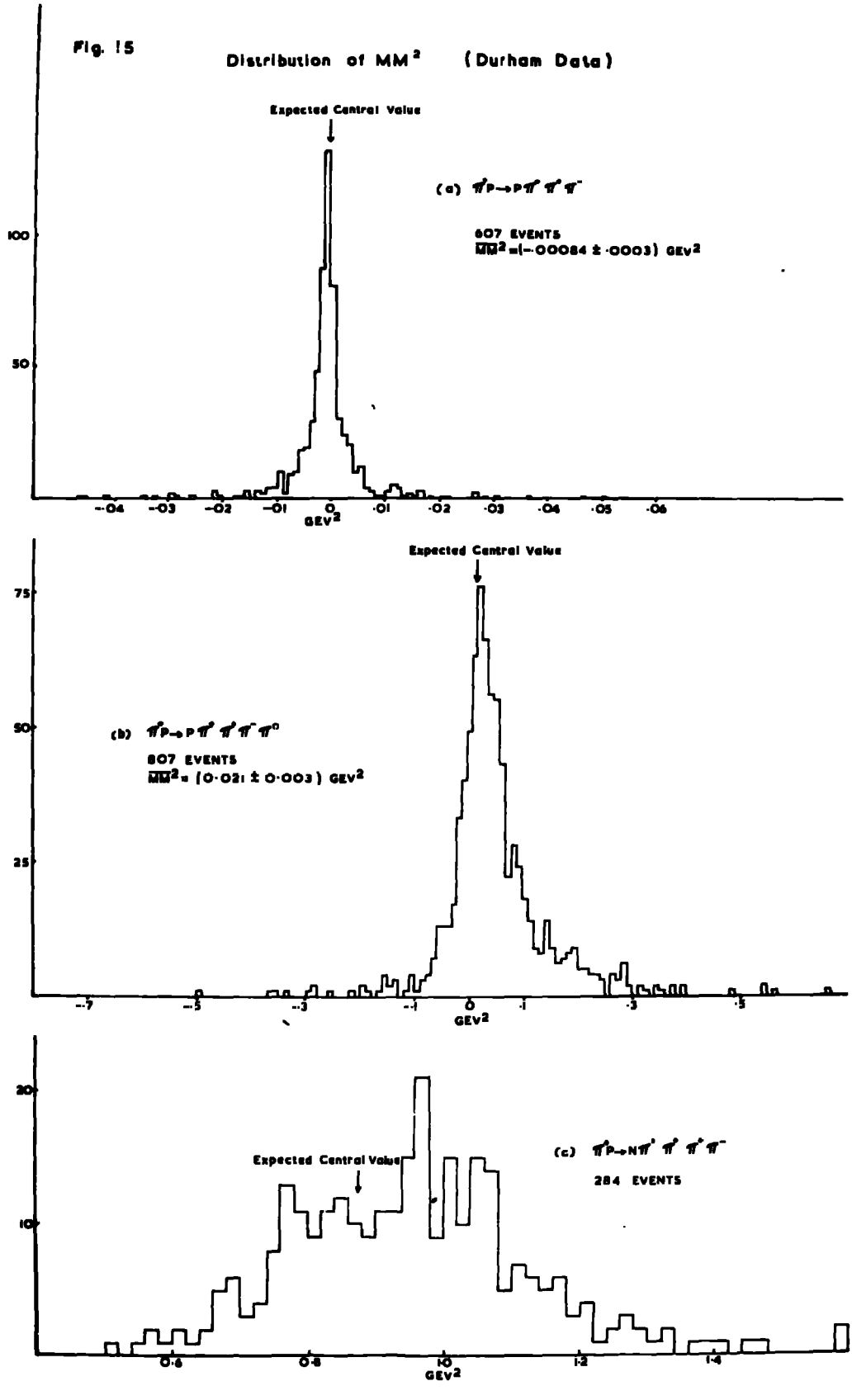

was not considered to have any significant effect on the dynamical parameters of the events. At SLICE level, the criterion on MM^2 for a 4C fit was

$$MM^2 - 2\,\Delta MM^2 \leq 0.0 \leq MM^2 + 2\,\Delta MM^2 \quad Gev^2$$

As the error ΔMM^2 was large for the events near the edges of the distribution, the above condition retained all the 4C fits in the Durham sample in the final classification. Only 6 events gave double fits with respect to the hypotheses 1, 2 and 3 while one event was ambiguous between the hypotheses 2 and 8. These few ambiguities were resolved by taking the hypothesis with the smaller χ^2 value.

As the error on missing mass is sometimes very large ($\sim$ 0.3 GeV) it becomes difficult to determine whether an extra π^o is possible in a 4C fit. Since a fraction of 15% of the 4C fits was chosen in preference to 1C π^o fits on the predictions of Fake calculations, an attempt was made to test the purity of the 4C sample from a study of the transverse momentum unbalance in an event. This was based on the following considerations.

High energy tracks (momentum > 1 GeV/c) are emitted at small angles. A high energy missing track is certain to be observed in the fitting procedure. The average momentum of the π^o's produced was $\sim$ 1 GeV/c. The π^o's which are produced at momenta lower than the average value are emitted at larger angles, so that the error on the longitudinal momentum (X-momentum) will be comparatively

FIG. 16. DISTRIBUTION OF TRANSVERSE MOMENTUM (LAB. SYSTEM) OF THE MISSING TRACK

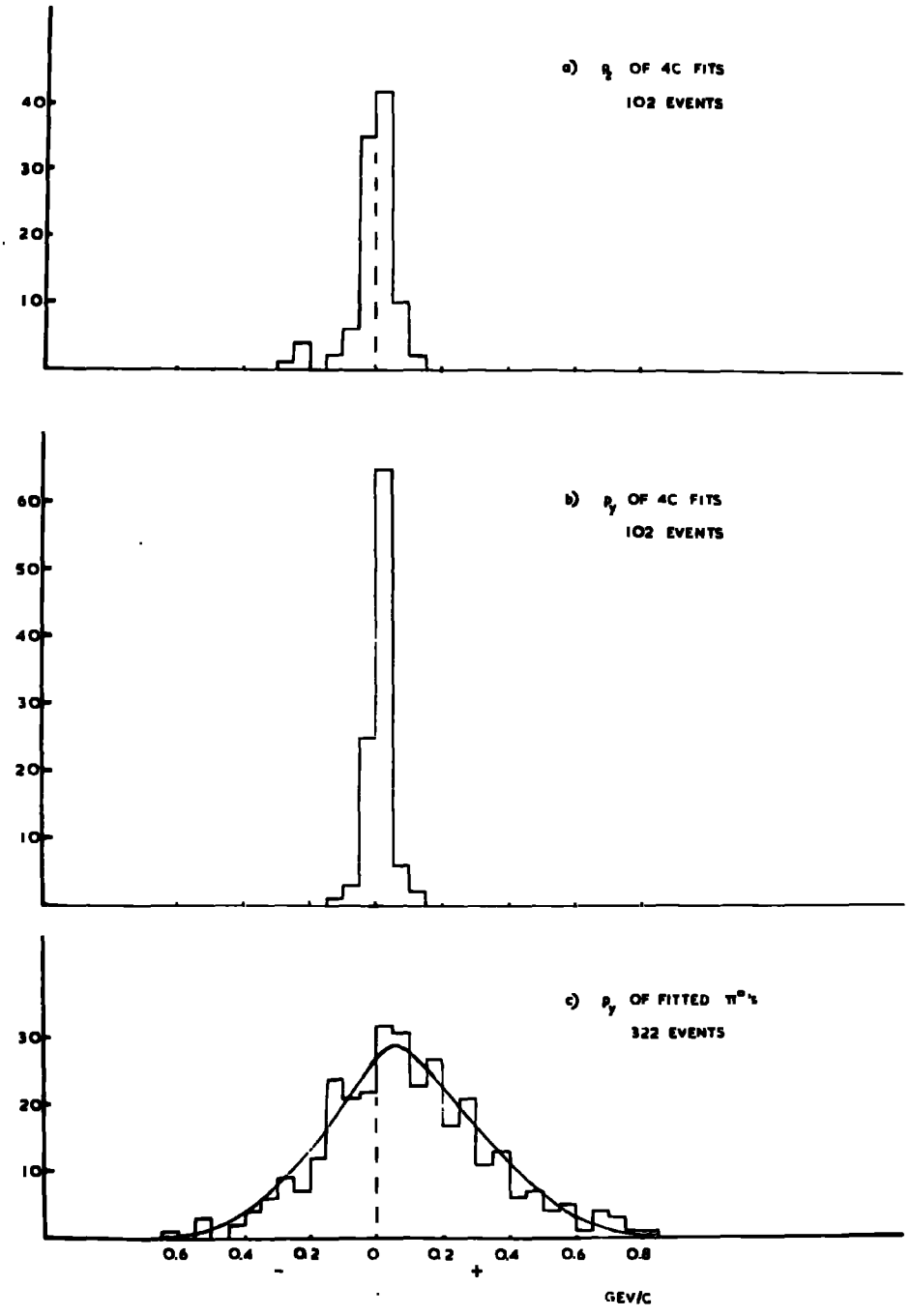

larger than the error on the transverse momentum. The transverse momentum has two components, the Y-component which is parallel to the windows and the Z-component which is parallel to the camera axis. Due to stereo reconstruction one would expect the Y-component to be more reliable than the Z-component.

Figure 16(a) shows a distribution of the momentum unbalance in the Z direction and Figure 16(b) shows the distribution of the momentum unbalance in the Y direction for a sample of the 4C fits. The momentum unbalance |Py| is mostly limited to 50 Mev/c and is better than the |Pz| unbalance.

The momentum unbalance |Py| of the 4C fits may be compared with Figure 16(c) which shows a distribution of the Y-momentum of the fitted π^o's in a sample of unambiguous events. The distribution is fairly smooth and is fitted by a normal distribution curve with a χ^2 probability ~51%. The average Py of the π^o's is (90 ± 12) Mev/c. As can be seen, a fraction of only 15% of the π^o's produced have |Py| $\leq$ 50 Mev/c. Besides the absence of any significant deviation from the smooth distribution in the region |Py| $\leq$ 50 Mev/c suggests that there is very little contamination of π^o events in the 4C sample.

1C(π^o) fits

The fraction of events initially selected in this channel i.e. without applying any criterion for MM^2 was about 29% including a fraction of 4% which were ambiguous with either a neutron or an η^o fit. The events which were ambiguous between π^o and η^o fits were

mostly unambiguous in the assignment of the proton track. Figure 15(b) shows the distribution of MM^2 corresponding to the π^o fits including the ambiguous events. The distribution shows a peak at about 0.02 GeV which corresponds to the square of the π^o mass. The distribution is, however, broad and considering the ambiguities present, not all these events are genuine π^o events, particularly those with large MM^2. As the errors associated with MM^2 were large, the criterion chosen to get a purer sample of π^o events was

$$-0.12 \leq MM^2 \leq 0.12 \text{ Gev}^2$$

Under this criterion about 85% of the events in the above plot were classified as π^o events. The use of the above criterion was justified by the fact that of the events rejected by the criterion only 1% gave rise to an ω signal while of those retained by it the fraction which contributed to the ω signal was about 20%. It was further estimated that not more than 5% events were lost in this way and those finally classified as π^o events did not have a contamination of more than 5% from other channels.

1C (neutron) fits

Figure 15(c) shows the distribution of the square of the missing mass for events with a neutron fit. The events were selected on the basis of ionisation and the kinematical fit criterion, $\chi^2 \leq 6$. About 60% of the events in this distribution belonged to the 'no proton' ionisation code (c.f. Table 4). About a third of the events which

were ambiguous, mostly with η^o fits and a few with π^o fits, were selected on the highest χ^2 probability. The distribution of MM^2 is broad and does not show any sharp peak in the region of the neutron mass because of the errors of measurement. To reduce contamination, the following criterion for MM^2 was used

$$0.66 < MM^2 < 1.20 \quad GeV^2$$

Under this criterion, 85% of the events, which fitted the neutron hypothesis, were classified as neutron events. The fraction of events thus classified constituted about 9% of the total 4 prong events. If a more severe cut at $\chi^2 < 4$ is applied, the distribution of MM^2 peaks at the neutron mass and under the above criterion for MM^2 about 8% of the 4 prong events are classified in the neutron channel. The cross-section for this channel has been calculated on both these estimates.

1C (η^o) fits

A fraction of 13% of the 4 prong events gave fits to the η^o hypotheses on the basis of ionisation and $\chi^2 \leq 6$. About 5% of these events were ambiguous with neutron or π^o hypotheses. About a third of the ambiguous events were classified in the neutron and π^o channels, on the basis of highest χ^2 probability. On the overall MM^2 spectrum the η^o fits produced a weak peak. Because of the large measurement errors it was difficult to separate the η^o from the $\eta^o + n(\pi^o)$ $(n \geq 1)$ events and considering that the η^o has an experimental width, the fits obtained were contaminated by spurious fits to a large and

uncertain extent. Any estimate of the cross-section for this channel was considered to be unreliable at this stage.

NO-FIT EVENTS

The unambiguous no-fit events consistent with more than one missing neutral particle were initially classified to be about 29% of the total sample of the 4 prong events. By including the events rejected from the π^0 and neutron fits under the criteria chosen for these channels, the fraction of the no-fit events rises to about 35%. The cross-section for the no-fit channel has been calculated on this last estimate which does not include the uncertain fraction of events which give rise to the spurious η^0 fits.

3.13 Cross-Sections and Statistics

DURHAM DATA

A total of 3307 four prong events were processed and recorded on the Data Summary Tape (DST) as Durham's contribution to the combined data of the collaboration. This sample constituted about 54% of the total 4 prong events found in scan. An estimate has been made of the total and partial cross-sections by using the Durham data which is then compared with the combined data. The cross-section per event has been computed from a knowledge of the total number of frames scanned, the geometry of the fiducial volume and the distribution of the number of beam tracks per frame. By counting tracks in every tenth frame of all the films, the mean number of beam tracks per frame was found to be 11.8. Corrections were made for an estimated

muon contamination of (2 ± 1)% and an absorption of 3% of the beam tracks. The cross-section per event on the DST was calculated to be (3.32 ± 0.15) μb. The sources of error were:

(i) the Density of Hydrogen - This was due to the uncertainty in the temperature of liquid hydrogen which was taken as (27 ± 0.5)°K for which the density was(0.0611 ± 0.0006) gm. per c.c., so that the uncertainty was about 1%.

(ii) The mean number of tracks per frame: A statistical error of 5% was taken into account.

(iii) Number of events: A statistical error of 1% was taken into account on the total number of events after correcting for scanning loss.

Table 5 shows the number of events and the total and partial cross-sections for the different channels. The cross-section for the no-fit channel has been calculated by excluding the spurious η^o events due to uncertainty in the estimation of those events.

Combined Data

Before combining the data of the six collaborating laboratories checks were made to test the consistency in the data presented by each group. The total and partial cross-sections computed individually did not show any significant deviation from each other. The fractions of events in the different 1C and 4C channels for each subset of data were found to be consistent with each other. An investigation of the $\pi^+\pi^-\pi^o$ mass spectrum in each subset of data showed consistency

TABLE 5

Total and Partial Cross-sections of 4-prong events
(Durham Data)

	Number of events analysed	Cross-section (mb)
Total 4 prongs	3307	10.97 ± 0.5
$\pi^+p \rightarrow p\pi^+\pi^+\pi^-$	768	2.55 ± 0.15
$\pi^+p \rightarrow p\pi^+\pi^+\pi^-\pi^0$	824	2.74 ± 0.13
$\pi^+p \rightarrow n\pi^+\pi^+\pi^+\pi^-$	297	0.99 ± 0.04 $\chi^2 \leq 6$ 0.87 ± 0.04 $\chi^2 < 4$
$\pi^+p \rightarrow p\pi^+K^+K^-$	40	0.13 ± 0.006
NO FIT (more than one missing neutral particle)	1155	3.83 ± 0.17

TABLE 6.

4 Prong Cross-sections (Combined Data)

	Number of events analysed	Cross-section (mb)
Total 4 prongs	23489	10.5 ± 0.5
$\pi^+p \rightarrow p\pi^+\pi^+\pi^-$	6004	2.69 ± 0.17
$\pi^+p \rightarrow p\pi^+\pi^+\pi^-\pi^o$	6287	2.81± 0.18
$\pi^+p \rightarrow n\pi^+\pi^+\pi^+\pi^-$	1911	0.84 ± 0.11

FIG 17 4 PRONG CROSS-SECTIONS

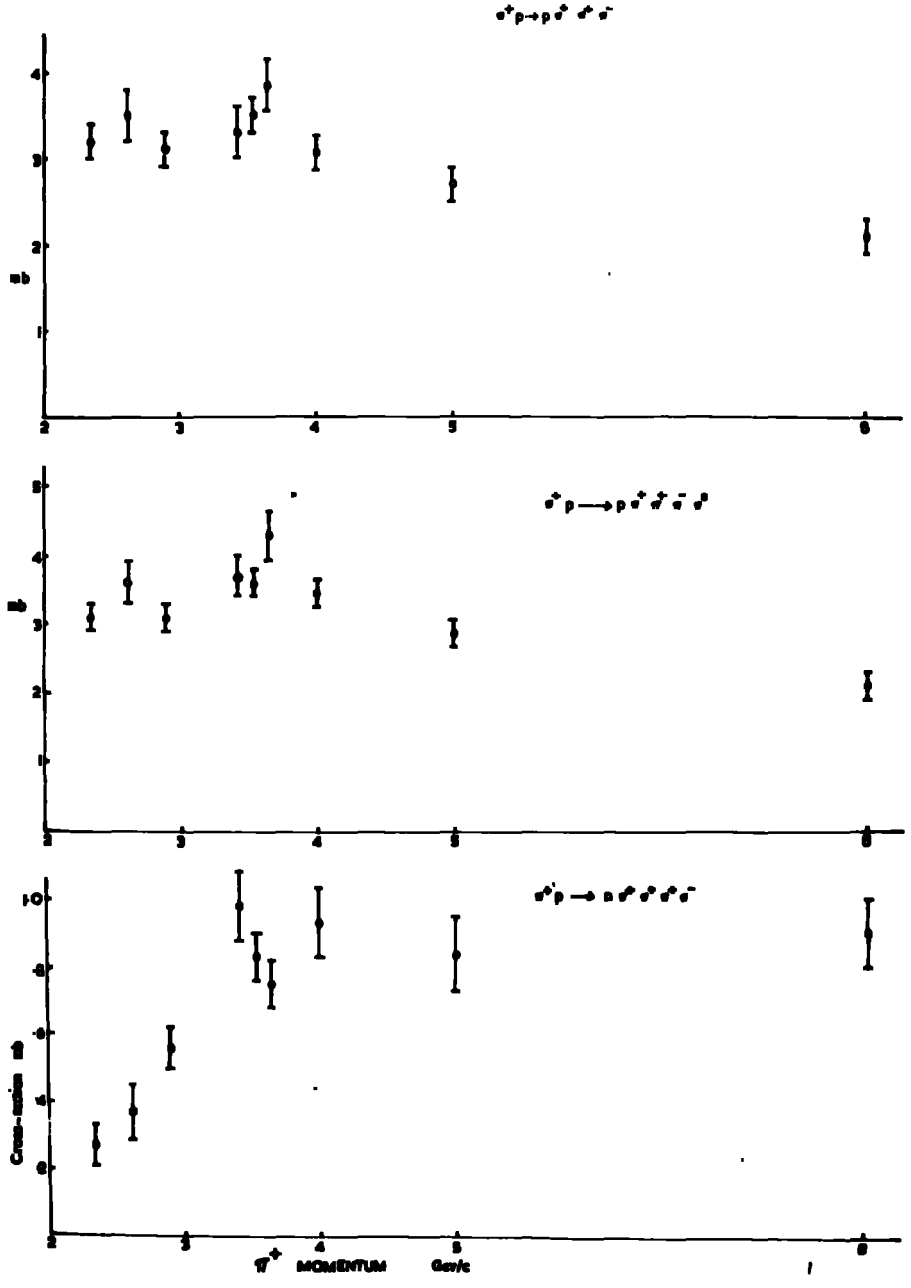

in the position, width and the contribution of the ω resonance.

Table 6 shows the total and partial cross-section which have been calculated by using a combined sample of 23489 events. The partial cross section for the channel $\pi^+p \to p\pi^+K^+K^-$ has been discussed in Chapter 5 and the value of the cross-section has been listed in Table 10 along with the cross-sections for the V^o events. The cross-section per plot event was calculated to be $(0.44 \pm 0.02)\mu b$. The sources of error considered were the same as in the case of the Durham data. Figure 17 shows a plot of the partial cross-sections in relation to some other available data at different energies (Maris et al., 1963, A-B-C Collaboration, 1964 and A-B-B-B-H-L-M Collaboration, 1965).

3.14 Phase Space and FOWL

A final state interaction between two or more particles such as a resonance has to be recognised against a background of randomly associated particles. To estimate the fraction of interactions resulting in resonance production, 'phase space' calculations are made of the distribution of effective masses, four-momentum transfer, production angles etc. expected for various mixturesof resonance and background. By comparison with the experimental distributions, the proportion of resonance can be estimated.

Phase space is the total volume available in the momentum-space for an interaction to take place and is determined by energy-

momentum conservation. The Lorentz invarient phase space for n particles in the final state is given by

$$R(Q, q_1 \ldots q_n) = \int \prod_{i=1}^{n} [d^4 q_i \; \delta(q_i^2 - m_i^2)] \delta^4\left(\sum_{i=1}^{n} q_i - Q\right)$$

where Q is the energy-momentum four-vector of the system and q_i, m_i are the energy-momentum four-vector and mass of the i-th particle. The differential distribution of R with respect to effective masses, momenta and other dynamical quantities gives the phase space prediction for these quantities.

FOWL

Instead of using the analytic method, the phase space distributions in the analysis of the V^o events (Chapter 5) were obtained by using the program FOWL. FOWL uses the Monte Carlo method to generate the required number of random events of a given type, as specified by the user. Each event is given a statistical weight according to the phase space distribution. The distribution of the dynamical quantities such as the effective masses, square of the four-momentum transfer from the target to any other particle or group of particles etc. as specified in the subroutine USER are printed as normalised histograms. The total weight (WEIGHT-SUM) of the generated events is also printed. The program allows any production mechanism such as the peripheral process to be included in the calculation and produces any control distribution of the dynamical quantities as may be required. Resonances can be introduced by a Breit-Wigner function

which increases the weight of those events which lie within the width of the resonance. The increase in WEIGHT-SUM can be varied to produce the required percentage of resonance production in a given sample.

The program is suitable for estimating the background under a resonance peak if the distributions outside the resonance band do not show deviations from the predictions of phase space. In multiparticle final states often more than one resonance is produced and the effective mass distributions outside the resonance band show deviations from phase space because of reflections from other resonances, kinematic effects and production mechanisms whose effects are largely uncertain and so cannot be simulated by the program. For these reasons the program was not found useful in estimating the background under the various resonances which are observed in the four-prong channels described in chapter 4. In fact eye estimations based on the distributions in the nearby bands of a resonance have been made in most cases. An approach can be made by expressing the background as a polynomial in effective mass, where the constants of the equation are determined empirically. This method works well where the resonance of interest is seated in the middle of the background. However, for example, the N^{*++} is situated at the lower mass end of the effective mass distribution, where the lower edge of the phase space is nearly vertical. This edge is difficult to reproduce accurately by a polynomial and it is

necessary to rely on estimates by eye.

In the analysis of the V^{o} events (c.f. Chapter 5) however, the Fowl program was found suitable in estimating the background under the observed resonance peaks as the distributions outside the peak regions did now show any significant deviations from the smooth phase space. This was because of the fewer number of resonances which are observed in any particular channel and the fact that the number of combinations per event in an effective mass distribution is only one in most of the strange particle channels.

The smoothness of the distributions produced by FOWL depends on the total number of events generated. In the present analysis 60,000 events were generated in each case and a fairly smooth distribution of the effective mass was obtained.

CHAPTER 4

Observation of Resonances in the Four-prong Channels

4.0 Introduction

In this chapter the two populous channels of the four prong events

(a) $\pi^+p \rightarrow p\pi^+\pi^+\pi^-$

and (b) $\pi^+p \rightarrow p\pi^+\pi^+\pi^-\pi^0$

are investigated and the resonances observed in the various effective mass plots are described. In both channels there is abundant production of resonances.

In channel (a) a strong production of $N^{*++}(1236)$ and ρ^0 is observed. Besides these two resonances appreciable amounts of the f^0 and the A_2^+ mesons are also observed. Evidence is found for an $N^{*+}(\rightarrow p\pi^+\pi^-)$ resonance at about 1720 MeV.

In channel (b) the dominant features are the production of $N^{*++}(1236)$ and the ω^0. Besides these two resonances, the ρ meson in its three charged modes (ρ^+, ρ^0, ρ^-), the η^0, A_2^0, A_2^+ and the B^+ mesons are also observed. (The $N^{*++}(1236)$ will be denoted as N^{*++}).

The production of the A_2 meson in channels (a) and (b) is discussed with the production in the $K\bar{K}$ channels (Chapter 5) and the neutron channel ($\pi^+p \rightarrow n\pi^+\pi^+\pi^+\pi^-$).

The important features of the two channels (a) and (b) are:

(i) the production of the resonances N^{*++}, ρ^o, ω^o and η^o preferentially at low values of $|t|$, the squared four momentum transfer and

(ii) the production of the double resonance states; the reactions $\pi^+p \rightarrow N^{*++}\rho^o$ and $\pi^+p \rightarrow N^{*++}f^o$ contribute to about 22% and 4% of channel (a), the reactions $\pi^+p \rightarrow N^{*++}\omega^o$ and $\pi^+p \rightarrow N^{*++}\eta^o$ contribute to about 6% and 0.5% of channel (b).

4.10 Resonance Production in channel (a).

4.11 N^{*++} and ρ^o

The two dimensional mass plot $M(p\pi^+)$ versus $M(\pi^+\pi^-)$ with two points for event is shown in figure 18. A considerable accumulation of events is observed in the N^{*++} and ρ bands. Figure 19 shows the projection on the $M(p\pi^+)$ axis. A strong production of the N^{*++} is observed. It is seen that the ratio of N^{*++} production to the background under the N^{*++} peak is about 2.5 to 1. The N^{*++} distribution is not symmetrical but is skewed to the higher mass side and the peak is shifted downwards by about 10 Mev from the generally accepted central mass value (1236 Mev). The solid line in the figure has been drawn as an eye estimation of the background under the N^{*++} enhancement. This has been done by considering the smooth distribution in the nearby bands on either side of the peak regions. The excess of events above this background is estimated to be (53±4)% and the cross-section for the production of N^{*++} is calculated to be

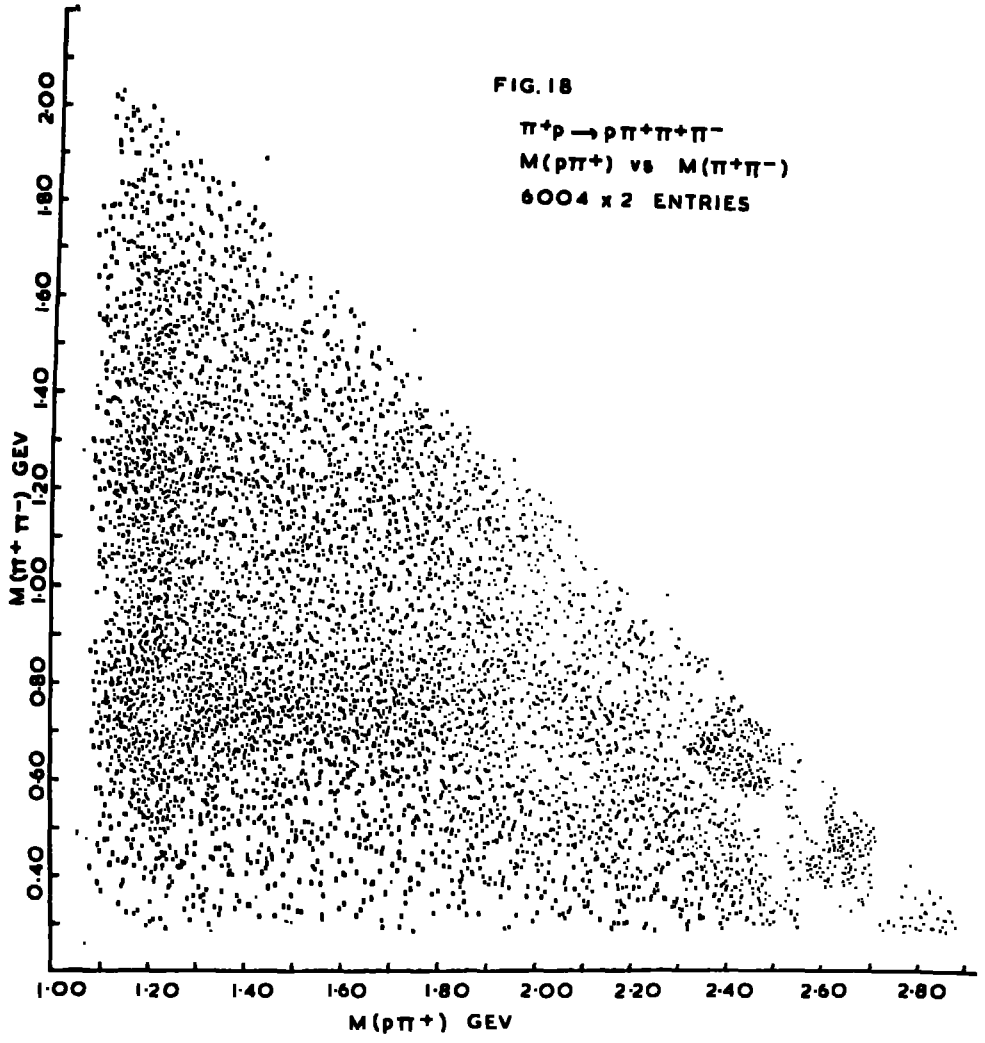
FIG. 18
$\pi^+p \rightarrow p\pi^+\pi^+\pi^-$
$M(p\pi^+)$ vs $M(\pi^+\pi^-)$
6004 x 2 ENTRIES
$M(\pi^+\pi^-)$ GEV
0·40
0·60
0·80
1·00
1·20
1·40
1·60
1·80
2·00
1·00
1·20
1·40
1·60
1·80
2·00
2·20
2·40
2·60
2·80
$M(p\pi^+)$ GEV

FIG. 19

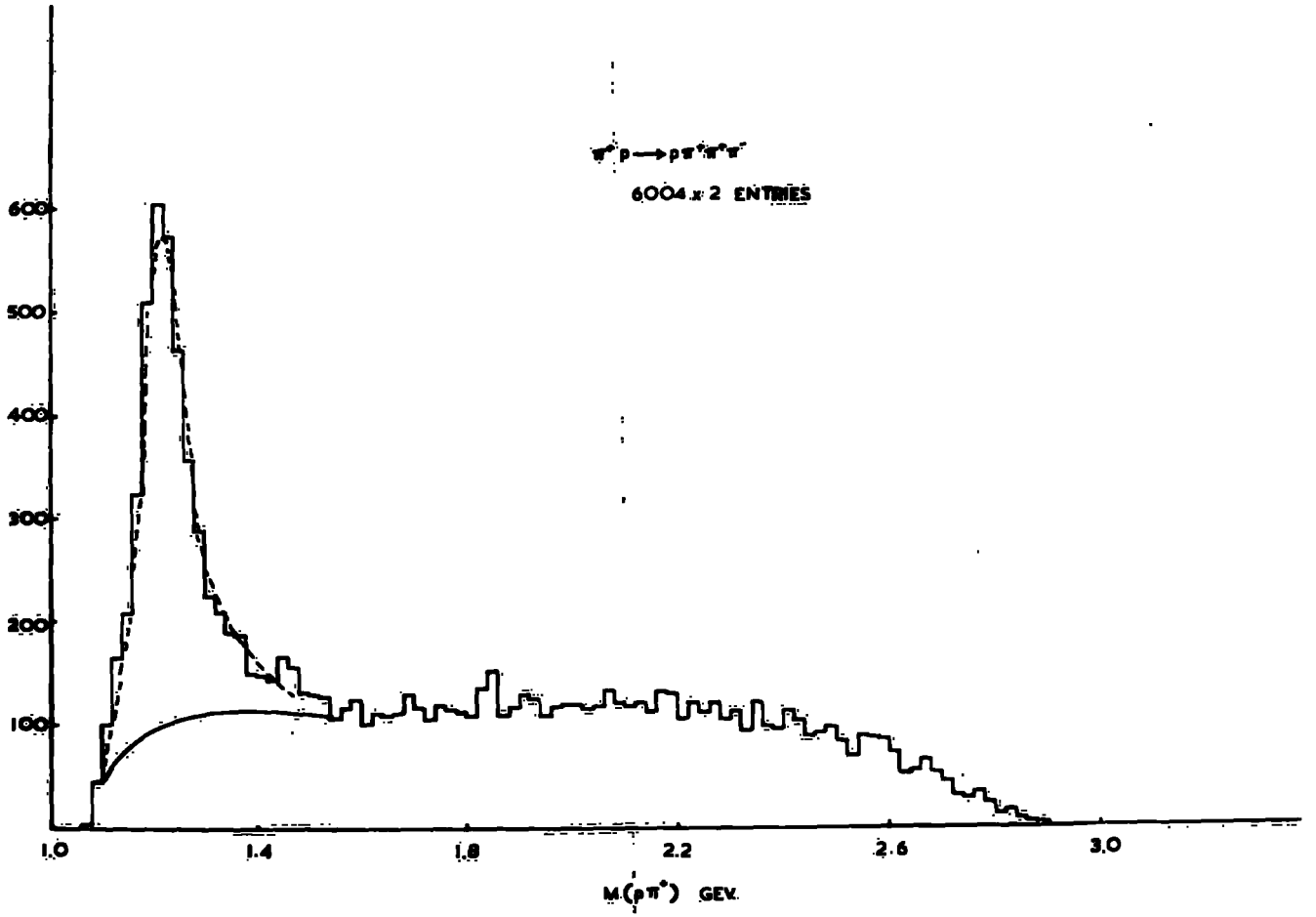
$\pi^- p \longrightarrow p\pi^+\pi^-\pi^-$
6004 x 2 ENTRIES
600
500
400
300
200
100
1.0
1.4
1.8
2.2
2.6
3.0
M($p\pi^-$) GEV.

FIG. 20

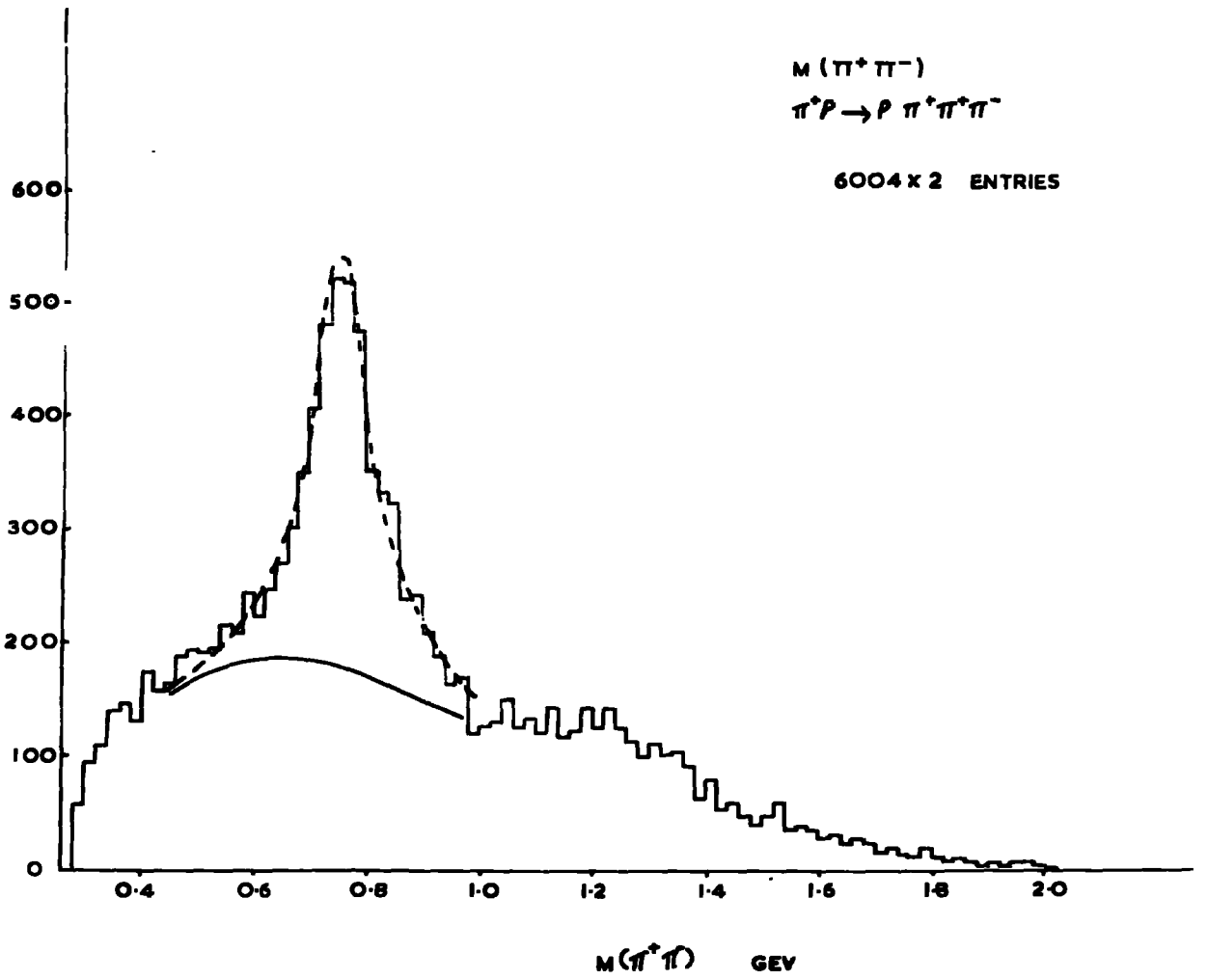
M (π⁺ π⁻)
π⁺P → P π⁺π⁺π⁻
6004 x 2 ENTRIES
600
500
400
300
200
100
0
0·4
0·6
0·8
1·0
1·2
1·4
1·6
1·8
2·0
M(π⁺π⁻) GEV

(1.43±0.12) mb.

It has been proposed by Jackson (1964) that the distribution of the mass of a broad two particle resonance such as the N^{*++} and ρ be represented by a modified Breit Wigner in which the width of the resonance is taken as energy dependent. This modified Breit Wigner has the form

$$\left(\frac{m}{q}\right) \cdot \frac{\Gamma(m)}{(m^2-m_o^2)^2+ m_o^2\ \Gamma(m)^2}$$

For the N^{*++}, the width $\Gamma(m)$ is given by

$$\Gamma(m) = \Gamma(m_o) \left(\frac{q}{q_o}\right)^s \cdot \frac{a\ m_\pi^2 + q_o^2}{a\ m_\pi^2 + q^2}$$

where m is the $P\pi^+$ effective mass, q is the 3-momentum in the $P\pi^+$ rest system and q_o the 3-momentum in the $P\pi^+$ rest system for $M(P\pi^+) = m_o$, the central mass value of the resonance.

For comparison, the $P\pi^+$effective mass distributed according to the above Breit Wigner was produced by FOWL. The parameters used were m_o = 1236 Mev, $\Gamma(m_o)$ = 120 Mev and a = 1.5, the average of the two Jackson values. The dotted curve is the modified Breit Wigner distribution normalised to the number of events above the background. The experimental distribution is in good agreement with the shape given by the Breit Wigner.

The $\pi^+\pi^-$ effective mass distribution is shown in figure 20. A strong production of the ρ^o is observed. As in the case of the

N^{*++} distribution, the background under the ρ^o peak has been estimated by eye (solid curve). The dotted line is the distribution of the ρ^o mass as given by the modified Breit Wigner discussed above. The width was taken as

$$\Gamma(m) = \Gamma(m_o)\left(\frac{q}{q_o}\right)^3 \frac{2\,q_o^2}{q_o^2+q^2}$$

where q is the 3-momentum in the $\pi^+\pi^-$ rest system, q_o the same at the central mass value m_o. The parameters used were m_o = 760 Mev and $\Gamma(m_o)$ = 124 Mev.

The experimental distribution is in good agreement with the shape given by the Breit Wigner. The excess of events above the background is estimated to be (52±4)% leading to a cross-section of the ρ^o production of (1.42±0.13) mb.

Both the N^{*++} and ρ^o are produced predominantly at low values of the squared four-momentum transfer $|t|$. Figure 21(a) shows the fraction of N^{*++} and ρ^o which are produced over the different ranges of $|t|$ values at intervals of 0.3 $(GeV/c)^2$. More than half of the N^{*++} and the ρ^o are produced at $|t| < 0.3$ $(GeV/c)^2$.

4.12 Production of the f^o

A broad enhancement in the f^o region is also observed in the $\pi^+\pi^-$ mass spectrum shown in figure 20. A better signal of the f^o is obtained when it is produced in association with the N^{*++}. This is shown in figure 22 in which the $\pi^+\pi^-$ mass spectrum has been drawn for those events in which the remaining π^+ forms a $P\pi^+$ combination

FIG. 21 Percentage of Resonances vs |t| intervals

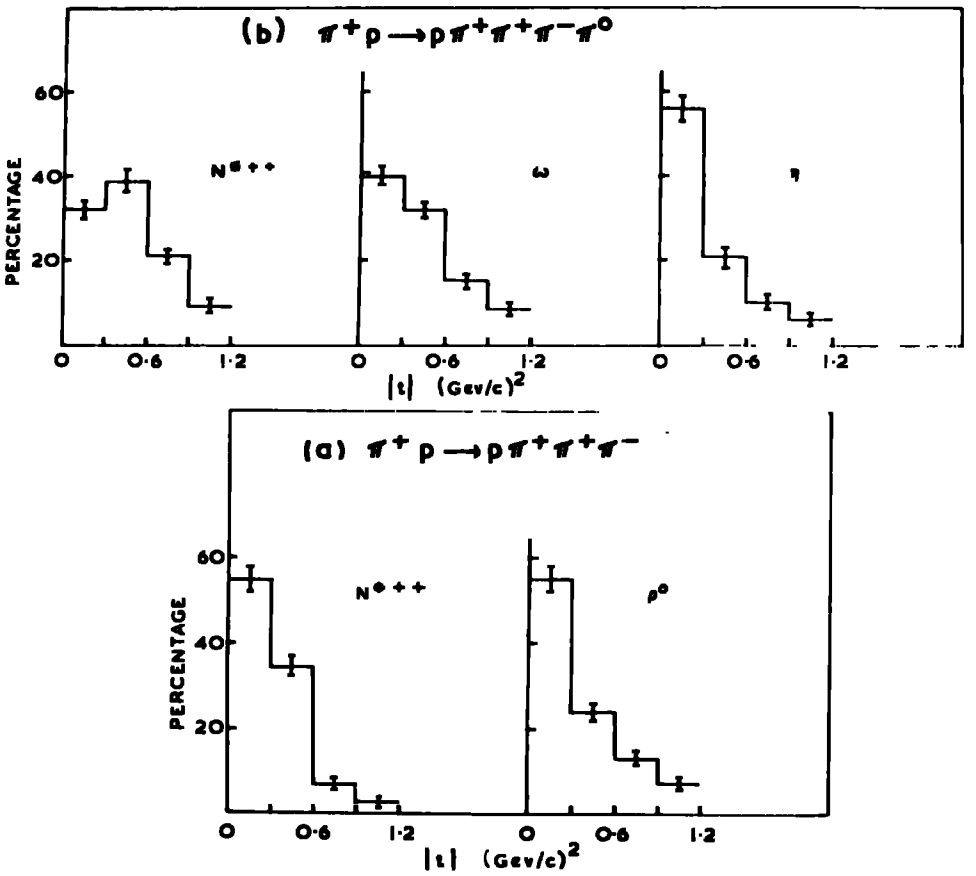

FIG. 22

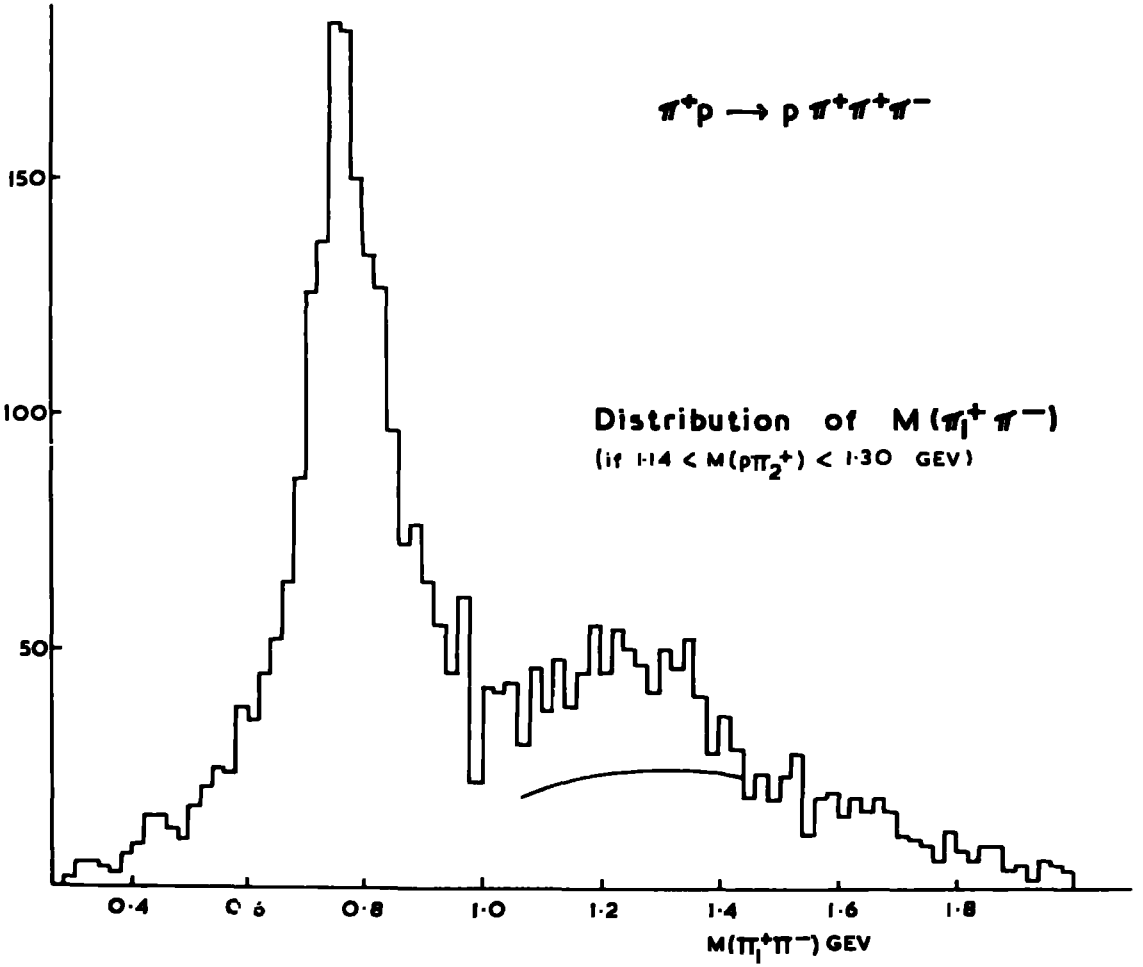
$\pi^+ p \longrightarrow p\,\pi^+\pi^+\pi^-$
Distribution of $M(\pi_1^+\pi^-)$
(if $1{\cdot}14 < M(p\pi_2^+) < 1{\cdot}30$ GEV)
150
100
50
0·4
0·6
0·8
1·0
1·2
1·4
1·6
1·8
$M(\pi_1^+\pi^-)$ GEV

in the N^{*++} band which is defined as $1.14 < M(P\pi^+) < 1.30$ GeV. The f^o is more pronounced in this figure. However an excess of events is observed between the f^o and ρ^o enhancements due to which the background estimation is subject to large errors. By subtracting a background which is estimated by eye (solid line) in the mass band (1250±100)MeV, the cross-section $\sigma(f^o \rightarrow \pi^+\pi^-)$ is calculated to be (0.11±0.03) mb. This value of the f^o cross-section is also the estimate of cross-section for the double resonance state $\pi^+P \rightarrow N^{*++} f^o$. Correcting for the unseen decay mode ($f^o \rightarrow \pi^o\pi^o$), the total cross-section becomes (0.17±0.05) mb.

Another feature of the production of the f^o is shown in figure 23(a). This figure shows the $\pi^+\pi^-$ mass spectrum (under the N^{*++} restriction) in which the direction of the π^+ in the $\pi^+\pi^-$ rest system is forward with respect to the incident pion. The signal to background ratio is much improved in this figure. The f^o distribution is symmetrical and the background estimation is more reliable (solid line). The dotted curve is the ordinary Breit Wigner distribution normalised to the excess of events above this background. The ordinary Breit Wigner has the form

$$\frac{\Gamma^2}{\frac{(m^2-m_o^2)^2}{m_o^2} + \Gamma^2}$$

The parameters used are m_o = 1250 MeV and Γ = 120 MeV. By taking twice the number of events above the background in this figure

FIG. 23. $\pi^+ p \rightarrow N^{*++} \pi^+ \pi^-$

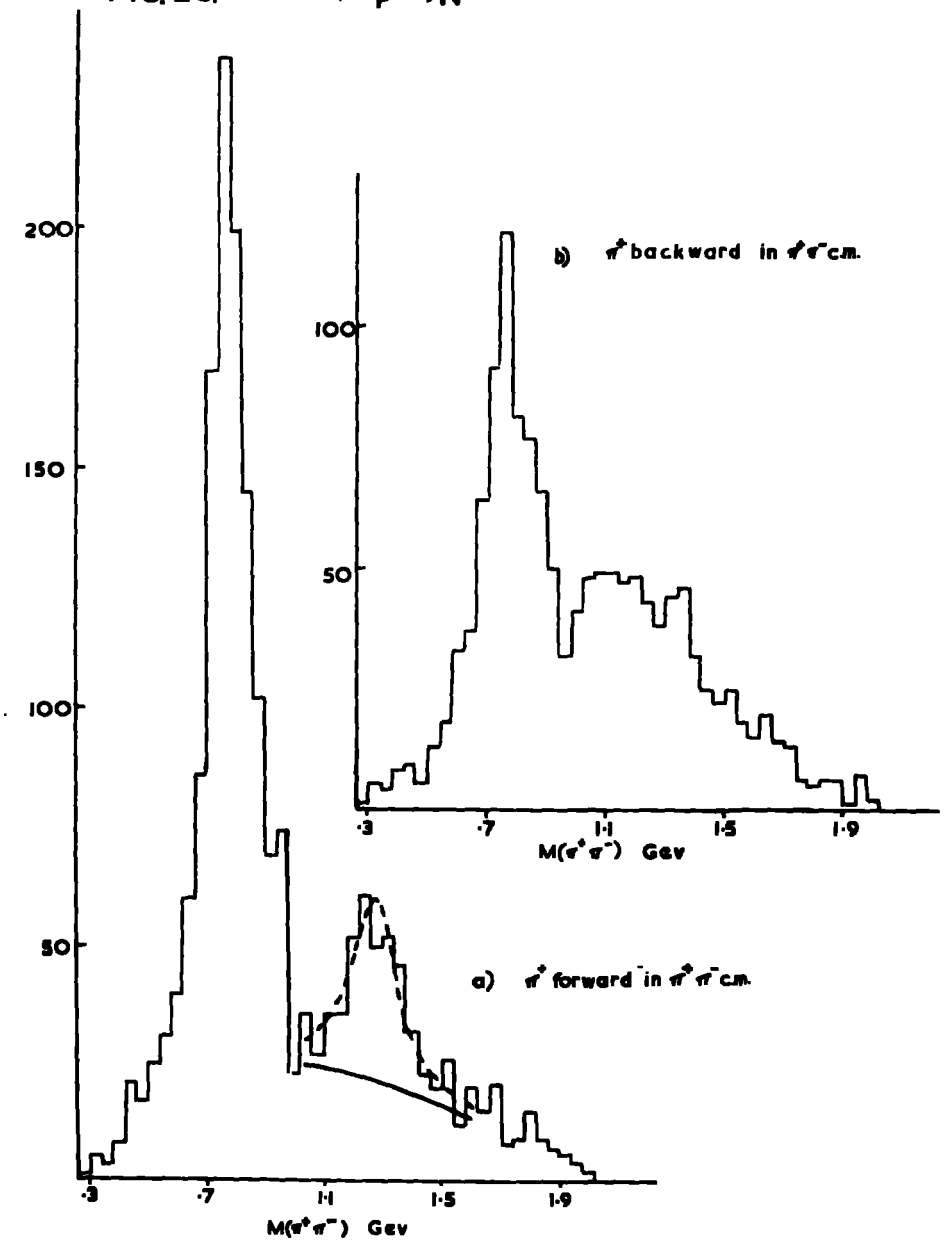

the cross-section $\sigma(f^{o} \rightarrow \pi^{+}\pi^{-})$ may be estimated as (0.24±0.06)mb. This estimate is based on an assumed symmetrical distribution of the f^{o} in the over-all spectrum. This assumption is not supported in figure 23(b) which shows the complementary $\pi^{+}\pi^{-}$ mass spectrum in which the π^{+} goes backward in the $\pi^{+}\pi^{-}$ rest system. This assumption may be one reason for the discrepancy between the two estimates of the f^{o} cross-section.

4.13 N^{*++} ρ^{o} Correlation

The scattered mass plot $M(P\pi^{+})$ versus $M(\pi^{+}\pi^{-})$ in figure 18 shows a concentration of events in the N^{*++} ρ^{o} overlap region. This indicates a strong correlation between the two resonances. Figure 24(a) shows the distribution of the $M(P\pi_{1}^{+})$ in the ρ^{o} band i.e. under the restriction $660 < M(\pi_{2}^{+}\pi^{-}) < 860$ Mev and figure 24(b) shows the distribution of the $M(\pi_{2}^{+}\pi_{1})$ in the N^{*++} band i.e. under the restriction $1140 < M(P\pi_{1}^{+}) < 1300$ Mev.

From these plots it is estimated that (21±2)% of the channel (a) contributes to the reaction

$$\pi^{+}P \rightarrow N^{*++} \rho^{o}$$

and the corresponding cross-section is calculated as (0.55±0.04)mb. This value of the cross-section may be compared with the results of other experiments which are shown in Table 7.

The Chew-Low plot $M(\pi^{+}\pi^{-})$ versus $|t|$ in figure 25 shows a clustering of events at low $|t|$ values in the region of the ρ^{o} mass.

FIG. 24

$$\pi^+ p \longrightarrow p\pi_1^+\pi_2^+\pi^-$$

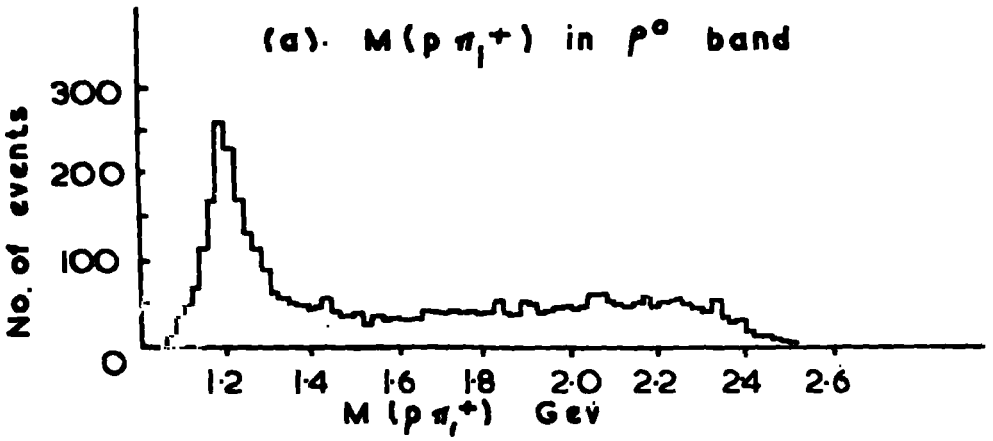

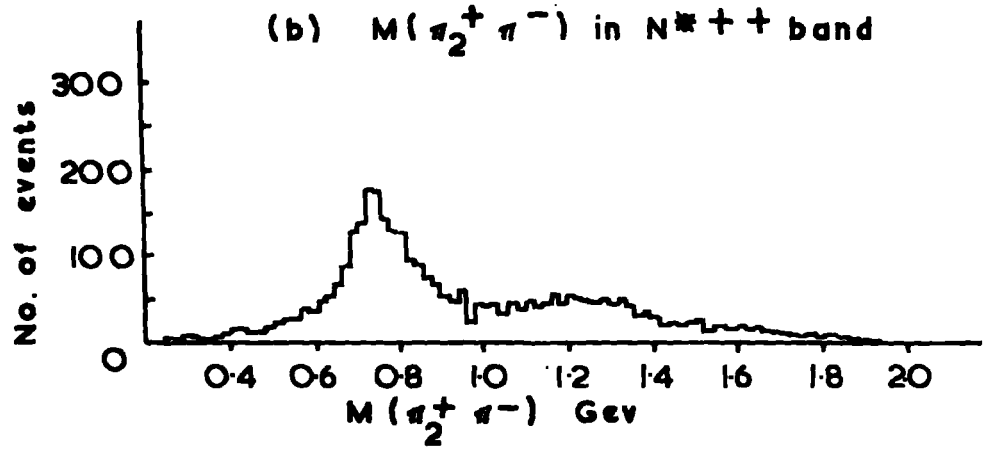

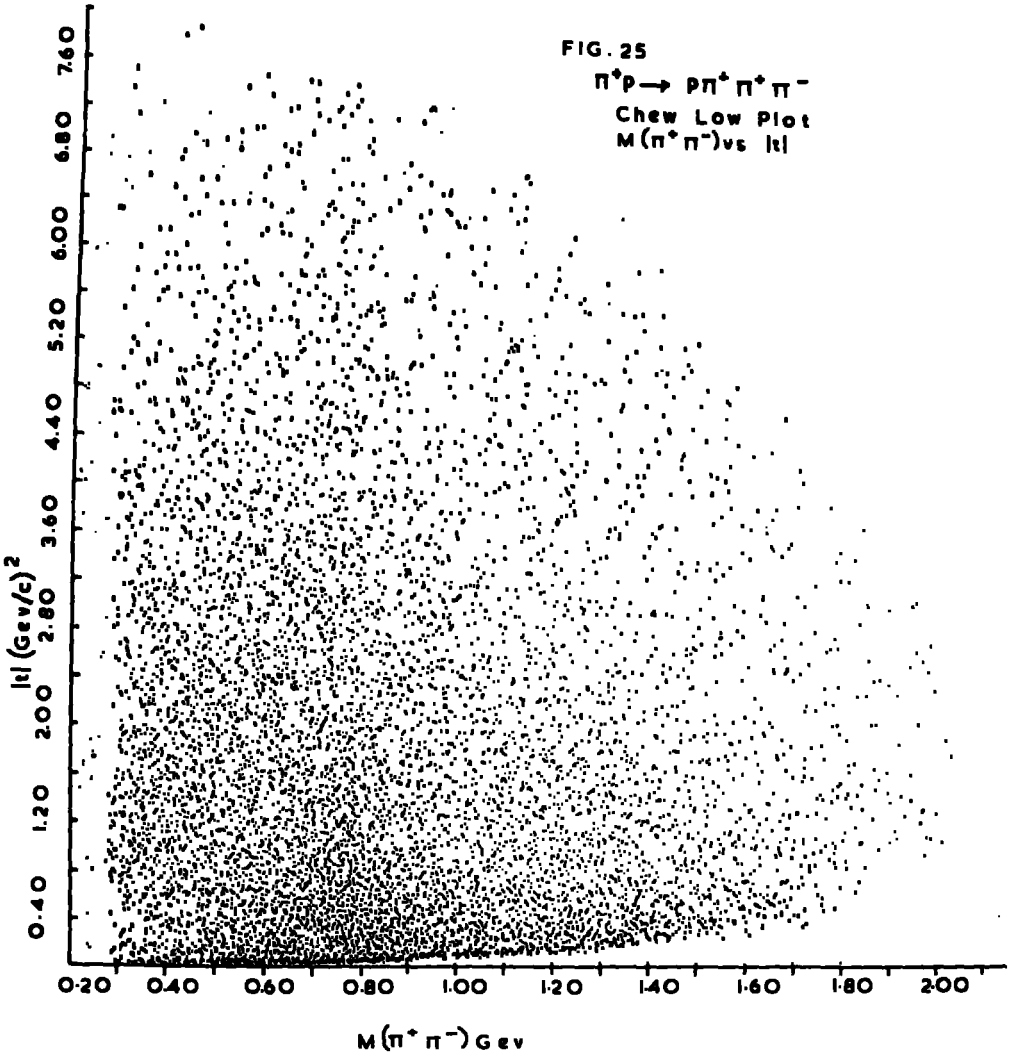
FIG. 25
$\pi^+ p \rightarrow p\pi^+\pi^+\pi^-$
Chew Low Plot
$M(\pi^+\pi^-)$ vs $|t|$
$|t|$ (Gev/c)^2
0·40
1·20
2·00
2·80
3·60
4·40
5·20
6·00
6·80
7·60
0·20
0·40
0·60
0·80
1·00
1·20
1·40
1·60
1·80
2·00
$M(\pi^+\pi^-)$ Gev

FIG. 26.

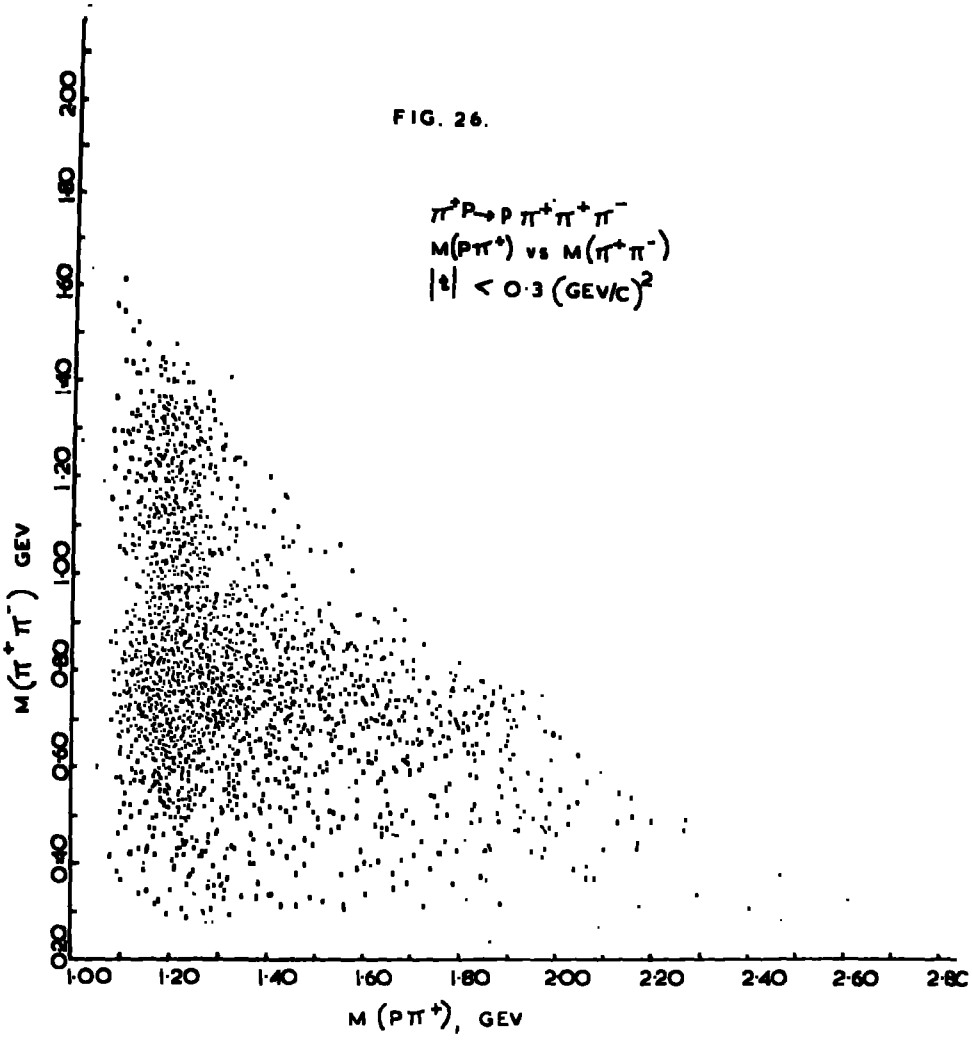
$\pi^- P \to p\,\pi^+\pi^+\pi^-$
$M(P\pi^+)$ vs $M(\pi^+\pi^-)$
$|t| < 0.3$ (GEV/C)^2
M($\pi^+\pi^-$) GEV
0·20
0·40
0·60
0·80
1·00
1·20
1·40
1·60
1·80
2·00
1·00
1·20
1·40
1·60
1·80
2·00
2·20
2·40
2·60
2·80
M ($P\pi^+$), GEV

FIG. 27.

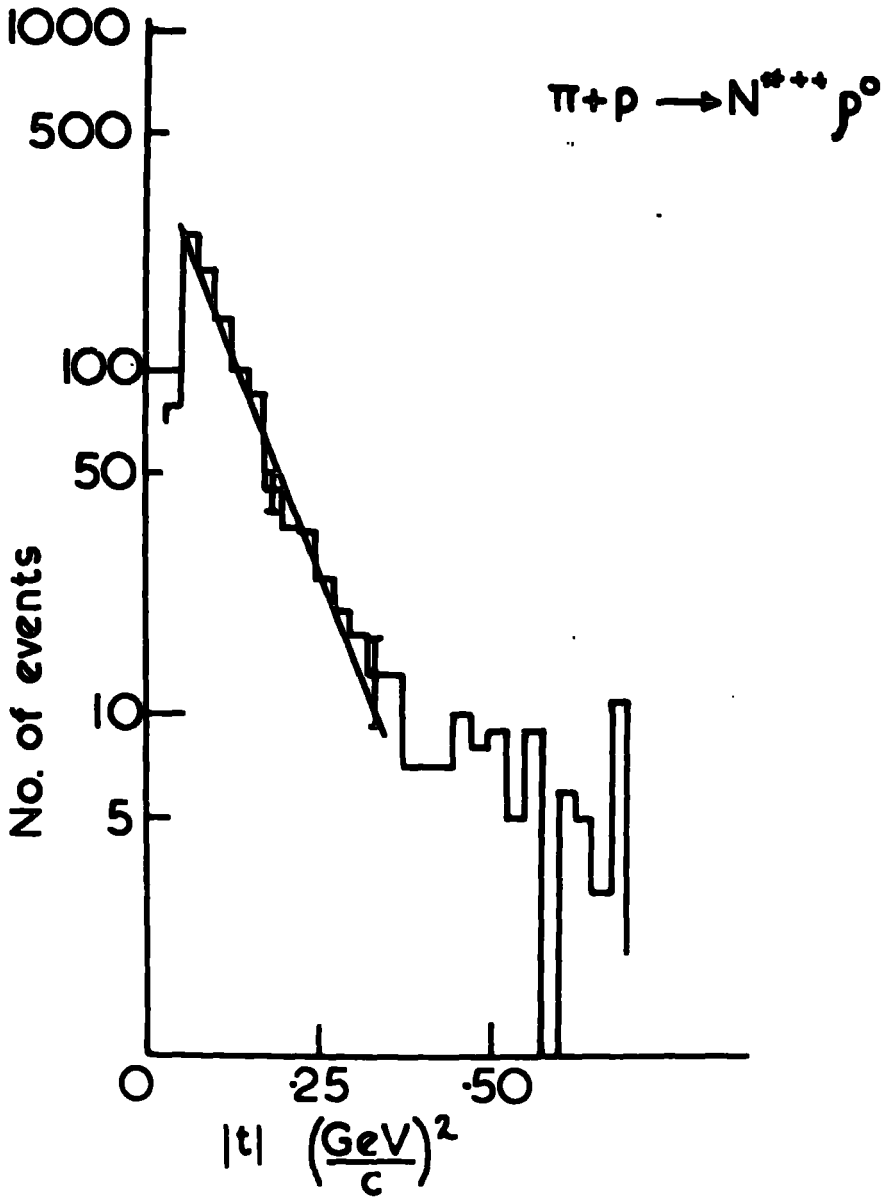
1000
500
100
50
10
5
No. of events
$\pi + p \rightarrow N^{*++} \rho^0$
0
·25
·50
$|t|$ $\left(\frac{GeV}{c}\right)^2$

By restricting $|t| < 0.3$ $(GeV/c)^2$, the scattered mass plot $M(P\pi^+)$ versus $M(\pi^+\pi^-)$ is obtained in figure 26. As can be seen this restriction has a strong purifying effect on the sample of events of the type $\pi^+P \rightarrow N^{*++}\rho^o$. The peripheral nature of this reaction is evident in figure 27 which shows the distribution of the number of events of the type above as a function of $|t|$ i.e. $\Delta^2(\pi^+/\rho^o)$. The distribution shows a sharp peak at low $|t|$ values indicating a strong production of the ρ^o in the forward direction. The distribution over the interval of $|t|$ ranging from 0.05 to $0.35(GeV/c)^2$ can be fitted by an exponential of the form $e^{-a|t|}$. The value of a obtained is (11.8 ± 0.5) $(GeV/c)^{-2}$.

Besides the peripheral nature of the reaction there is also evidence for a small but significant contribution of antiperipheral events to this reaction i.e. events in which the ρ^o is produced at high $|t|$ values or in the backward direction. This is shown in figure 28 which is a section of the Chew-Low plot $M(\pi^+\pi^-)$ versus $|t|$ for events of the type $\pi^+P \rightarrow N^{*++}\pi^+\pi^-$. This plot shows a clear evidence of concentration of events in the ρ^o band at high $|t|$ values. In a Feynman diagram these events may be interpreted as due to the exchange of a massive particle, in this case a non-strange baryon.

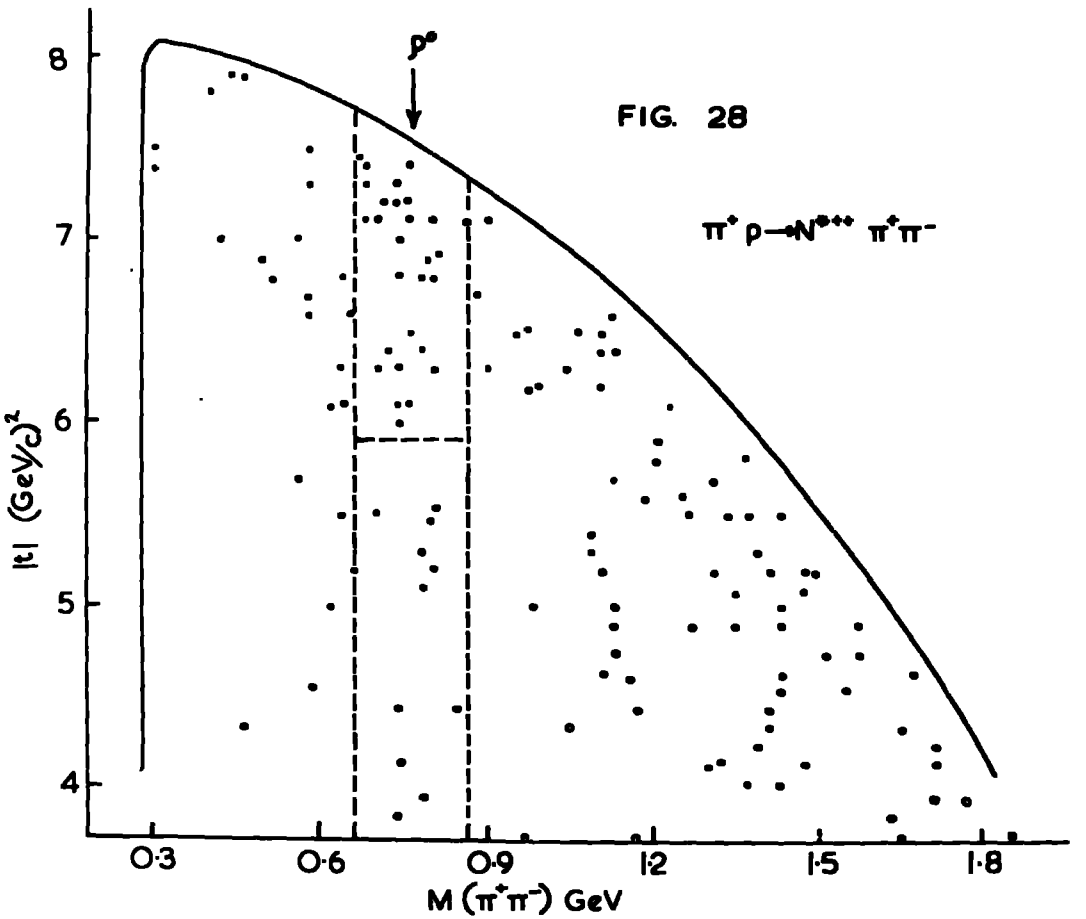
FIG. 28
$\pi^+ p \rightarrow N^{0++} \pi^+\pi^-$
ρ^0
8
7
6
5
4
$|t|$ (GeV/c)^2
0·3
0·6
0·9
1·2
1·5
1·8
M ($\pi^+\pi^-$) GeV

TABLE 7

Two-body Cross-sections (mb) -
(Corrected for unseen decay modes)

Reaction	4 Gev/c *	5 Gev/c	8 Gev/c **
$\pi^+p \rightarrow N^{*++}\rho^o$	0.60 ± 0.05	0.55 ± 0.04	0.43 ± 0.05
$\pi^+p \rightarrow N^{*++}f^o$	0.15 ± 0.05	0.17 ± 0.05	0.18 ± 0.05
$\pi^+p \rightarrow N^{*++}\omega^o$	0.39 ± 0.04	0.19 ± 0.02	0.10 ± 0.01
$\pi^+p \rightarrow N^{*++}\eta^o$	0.10 ± 0.005	0.052± 0.013	0.034± 0.011

* A-B-B-H-L-M Collaboration, Nuovo Cimento, 35, 659 (1965)

** A-B-C Collaboration - Physics Letters, 19, 608 (1965)

4.14 The A_2^+ meson

The $\pi^+\pi^+\pi^-$ mass spectrum is shown in figure 29(a). The shaded area in the histogram corresponds to those events in which at least one $\pi^+\pi^-$ combination is in ρ band defined as $660 < M(\pi^+\pi^-) < 860$ Mev. A significant enhancement with the peak at about 1300 Mev can be seen. In the $\rho\pi$ mass spectrum two peaks are generally seen, one near 1080 Mev and the other near 1300 Mev. They are called the A_1 and A_2 resonances. They have isospin I = 1. In the above figure no evidence is found for the A_1 peak; the small excess of events in the A_1 region is statistically insignificant. The absence of the A_1 peak has also been reported recently in π^+P collision at 7 GeV/c (Slattery, 1967).

The enhancement in the above figure has been identified as the $\rho^o\pi^+$ decay mode of the A_2^+. In order to produce a better A_2^+ signal the $\pi^+\pi^+\pi^-$ mass spectrum has been drawn for those events in which no $P\pi^+$ combination is in the N^{*++} band which is defined as $1120 < M(P\pi^+) < 1320$ Mev. This is shown in figure 29(b). The shaded area of the histogram corresponds to those events for which there is the additional restriction that at least one $\pi^+\pi^-$ combination is in the ρ band. About 126 events are counted as the excess of events above a smooth background in the shaded histogram. A 10% increase to this number is made because of the removal of events in the N^{*++} band (the fraction of events which contribute to the background under the N^{*++} enhancement is about 10%). On this correction the cross-section $\sigma(A_2^+ \rightarrow \rho^o\pi^+)$ is calculated as (63 ± 10) μb. This value of the cross-

FIG. 29

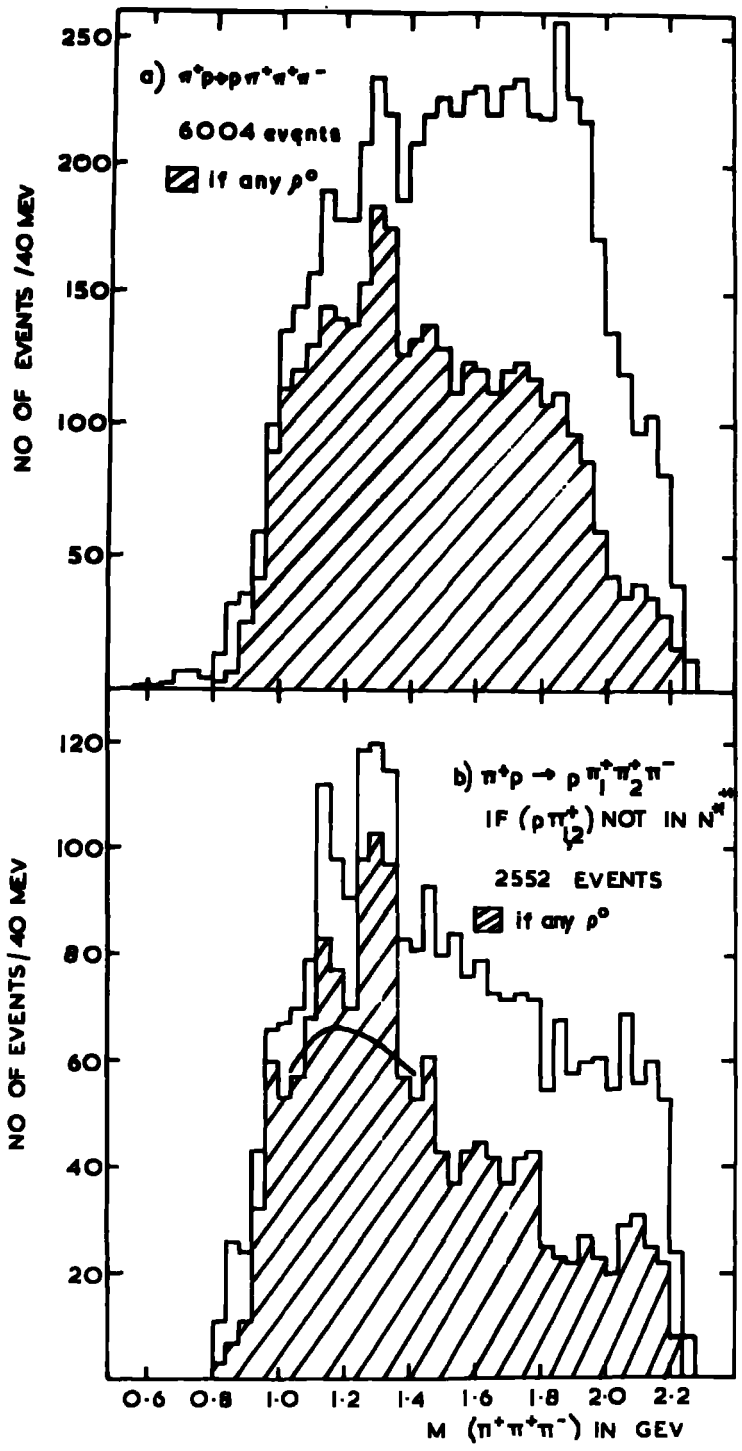
a) $\pi^+p\to p\pi^+\pi^+\pi^-$
6004 events
If any ρ^0
NO OF EVENTS /40 MEV
250
200
150
100
50
b) $\pi^+p\to p\pi_1^+\pi_2^+\pi^-$
IF $(p\pi_{1,2}^+)$ NOT IN N^{*++}
2552 EVENTS
If any ρ^0
NO OF EVENTS/40 MEV
120
100
80
60
40
20
0·6
0·8
1·0
1·2
1·4
1·6
1·8
2·0
2·2
M $(\pi^+\pi^+\pi^-)$ IN GEV

FIG. 30

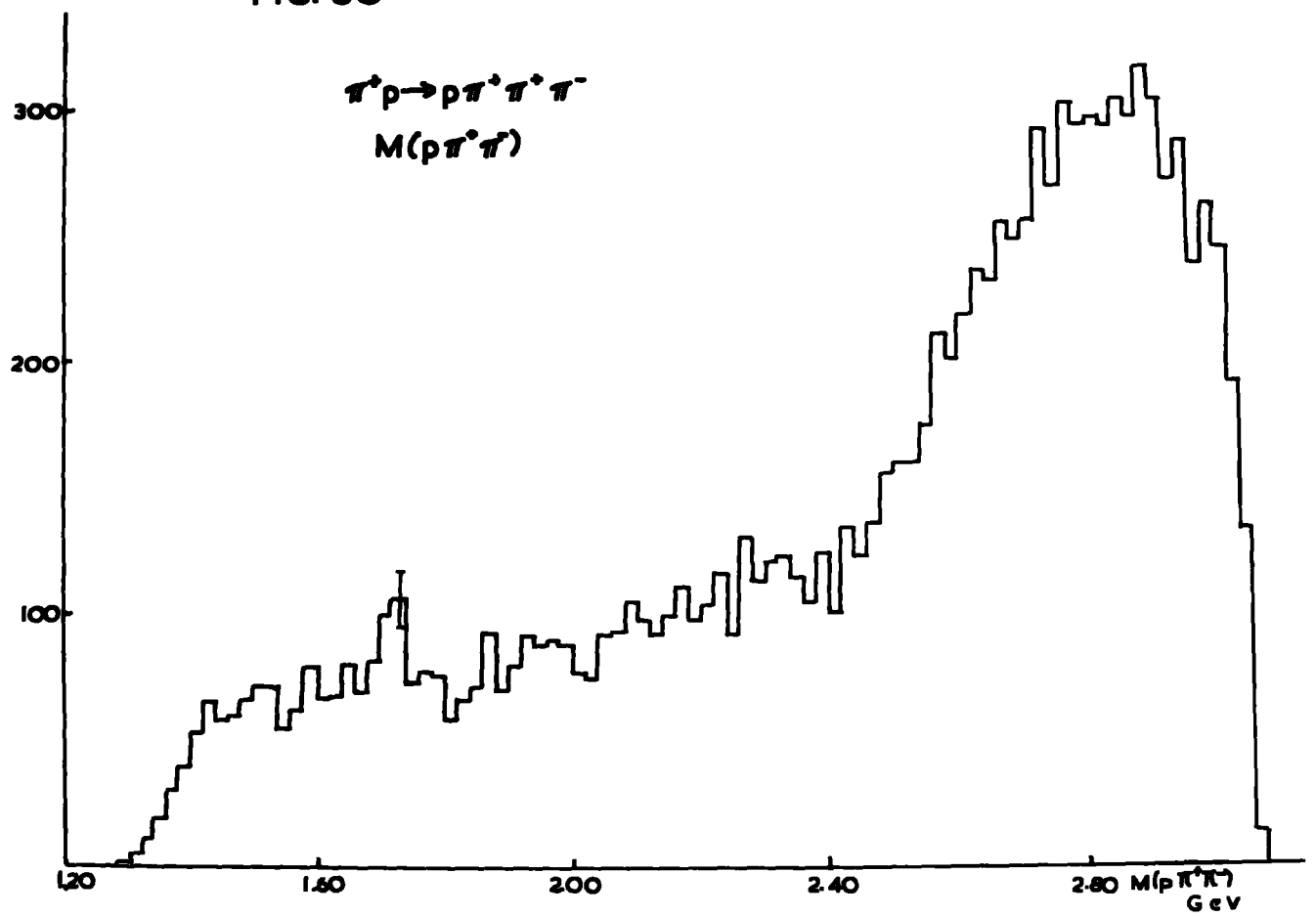
$\pi^+ p \to p\pi^+\pi^+\pi^-$
$M(p\pi^+\pi^-)$
300
200
100
1.20
1.60
2.00
2.40
2.80
$M(p\pi^+\pi^-)$
GeV

section is lower by a factor of about two than the results obtained in some πp experiments (Morrison, 1967).

4.15 A possible N^{*++} resonance at about 1700 Mev

In the $p\pi^+\pi^-$ mass spectrum shown in figure 30 a small enhancement of the order of four standard deviation is observed at the mass value of about 1720 Mev. In this mass region there is other evidence for such a resonance. For example, (Fleury, 1967) a resonance has been observed in this mass region in π^+d interactions at 5 GeV/c. In the above figure the number of events which contribute to the enhancement above a smooth background corresponds to the cross-section of (26 ± 6) μb.

4.20 Resonance Production in the channel (b)

4.21 N^{*++}, ω^o and η^o production

The production of these three resonances is demonstrated in the two dimensional scatter plot $M(p\pi^+)$ versus $M(\pi^+\pi^-\pi^o)$, two points per event in figure 31. Concentration of events is observed in the mass bands of the resonances.

Figure 32 shows the projection on the $M(p\pi^+)$ axis. A strong production of the N^{*++} is observed. As in the case of the channel (a), the phase space background under the N^{*++} peak has been estimated by eye (solid line). The excess of events above this background is estimated to be $(55\pm4)\%$ which corresponds to a cross-section of (1.55 ± 0.08) mb for the production of the N^{*++}. The N^{*++} distribution

FIG. 31

$\pi^+ p \to p\pi^+\pi^+\pi^-\pi^0$

$M(p\pi^+)$ vs. $M(\pi^+\pi^-\pi^0)$

6287 X 2 ENTRIES.

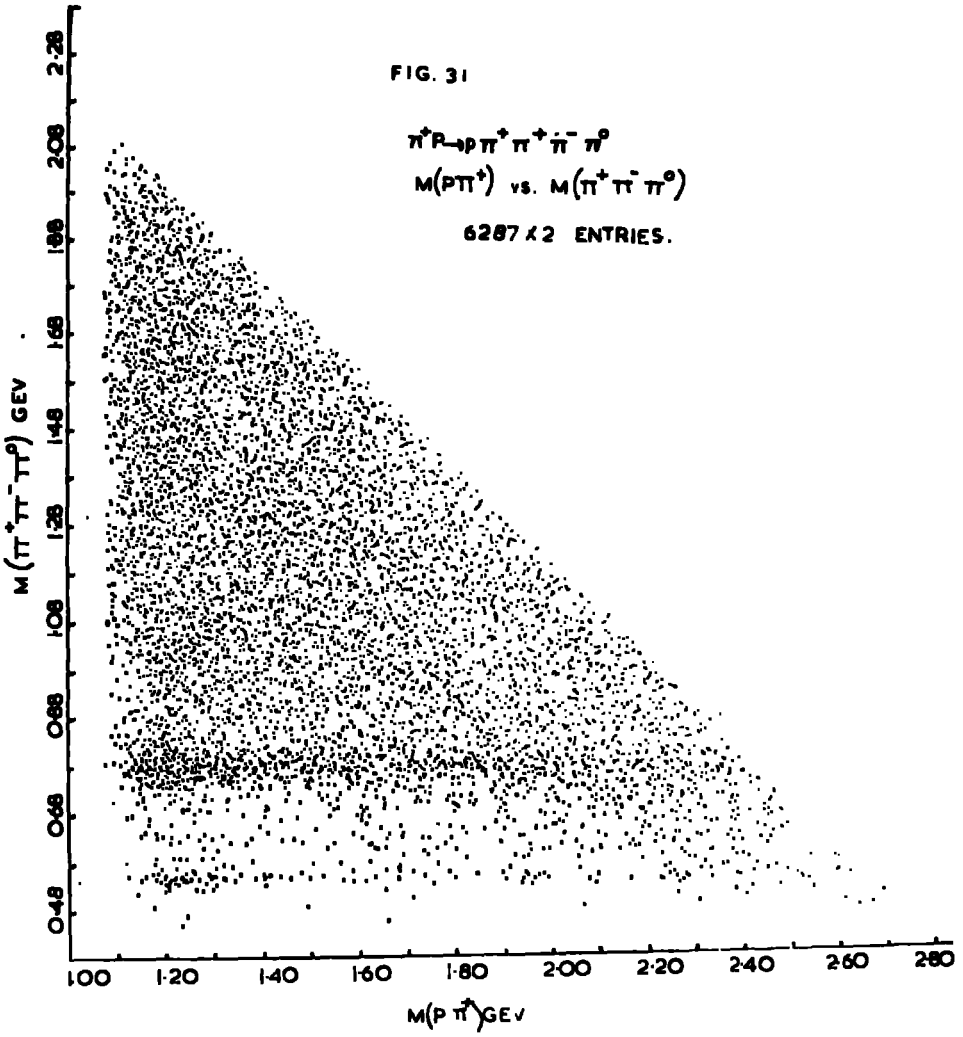

FIG. 32

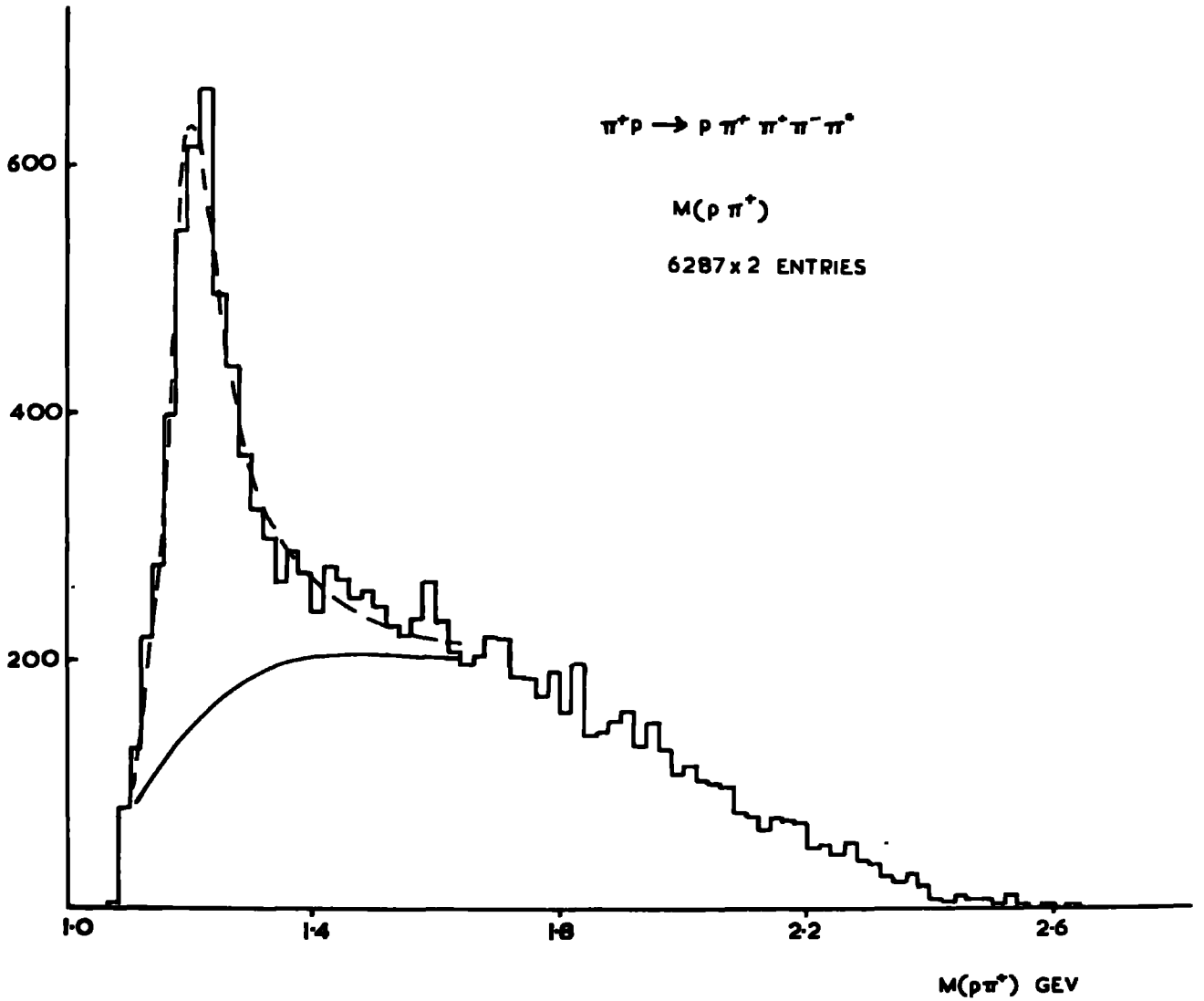
$\pi^+ p \rightarrow p\,\pi^+\,\pi^+\pi^-\pi^0$
M(p π+)
6287 x 2 ENTRIES
600
400
200
1·0
1·4
1·8
2·2
2·6
M(pπ+) GEV

FIG. 33

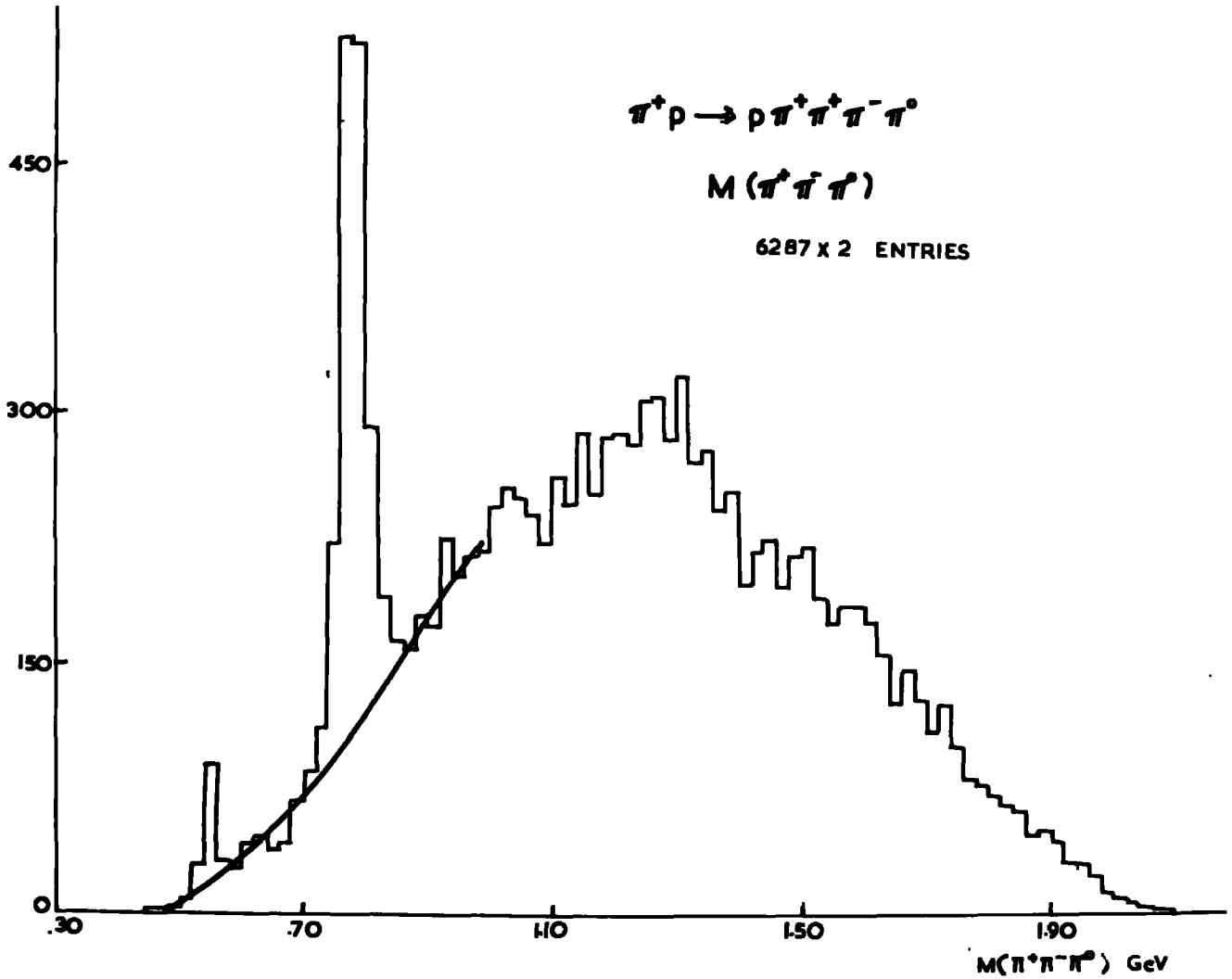
$\pi^+ p \rightarrow p\pi^+\pi^+\pi^-\pi^0$
$M(\pi^+\pi^-\pi^0)$
6287 X 2 ENTRIES
450
300
150
0
.30
.70
1.10
1.50
1.90
$M(\pi^+\pi^-\pi^0)$ GeV

can be represented by the modified Breit Wigner which has been discussed in section 4.11. Using the same parameters as before the dotted curve is obtained by normalising the Breit Wigner distribution to 55% of the events.

In the $\pi^+\pi^-\pi^o$ effective mass distribution shown in figure 33 a strong production of the ω^o and a significant production of the η^o is observed. The cross-sections for the production of the ω^o and η^o which have been estimated by counting the excess of events above a smooth background, are (0.60±0.10) mb and (40±5)μb (not corrected for unseen decay modes).

The N^{*++}, ω^o and the η^o are produced predominantly at low values of the squared four-momentum transfer $|t|$. Figure 21(b) shows the fraction of these resonances which are produced over the $|t|$ intervals of 0.3 $(GeV/c)^2$. The η^o is more peripheral than the other two resonances.

4.22 N^{*++} - ω^o and N^{*++} - η^o Correlation

In the two dimensional scatter plot $M(P\pi^+)$ versus $M(\pi^+\pi^-\pi^o)$ (figure 31) concentration of events is observed in the N^{*++} - ω and N^{*++} - η overlap regions. This gives evidence for the two-body reactions:

$$(i) \quad \pi^+P \rightarrow N^{*++}\omega^o$$

$$(ii) \quad \pi^+P \rightarrow N^{*++}\eta^o.$$

FIG. 34

$\pi^+ p \rightarrow p\pi_1^+ \pi_2^+ \pi^- \pi^0$

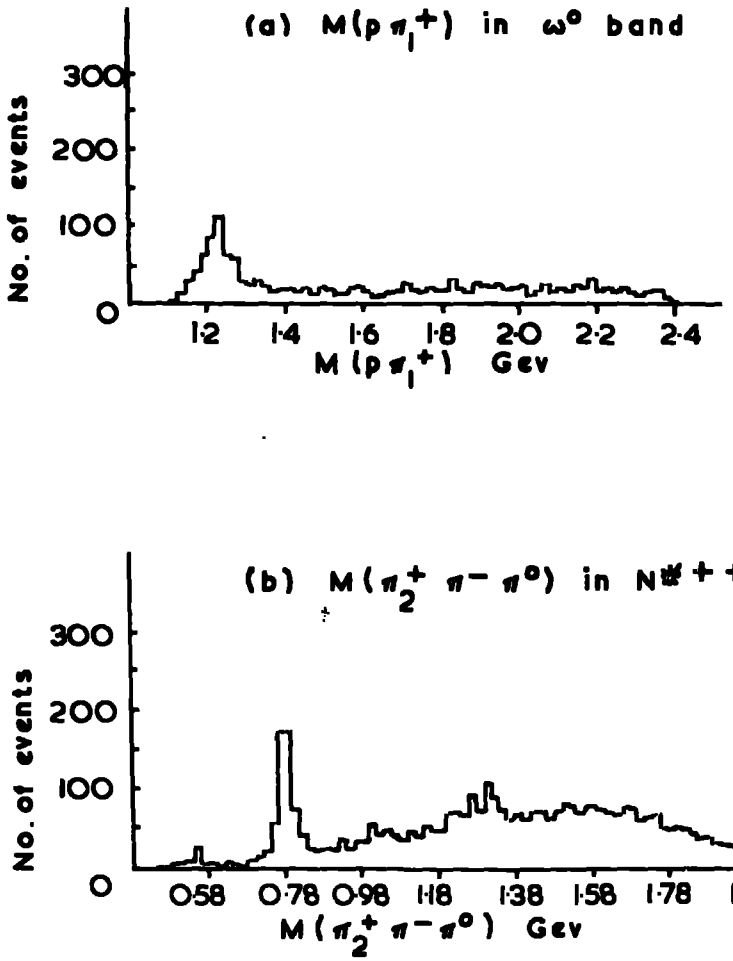

FIG. 35.

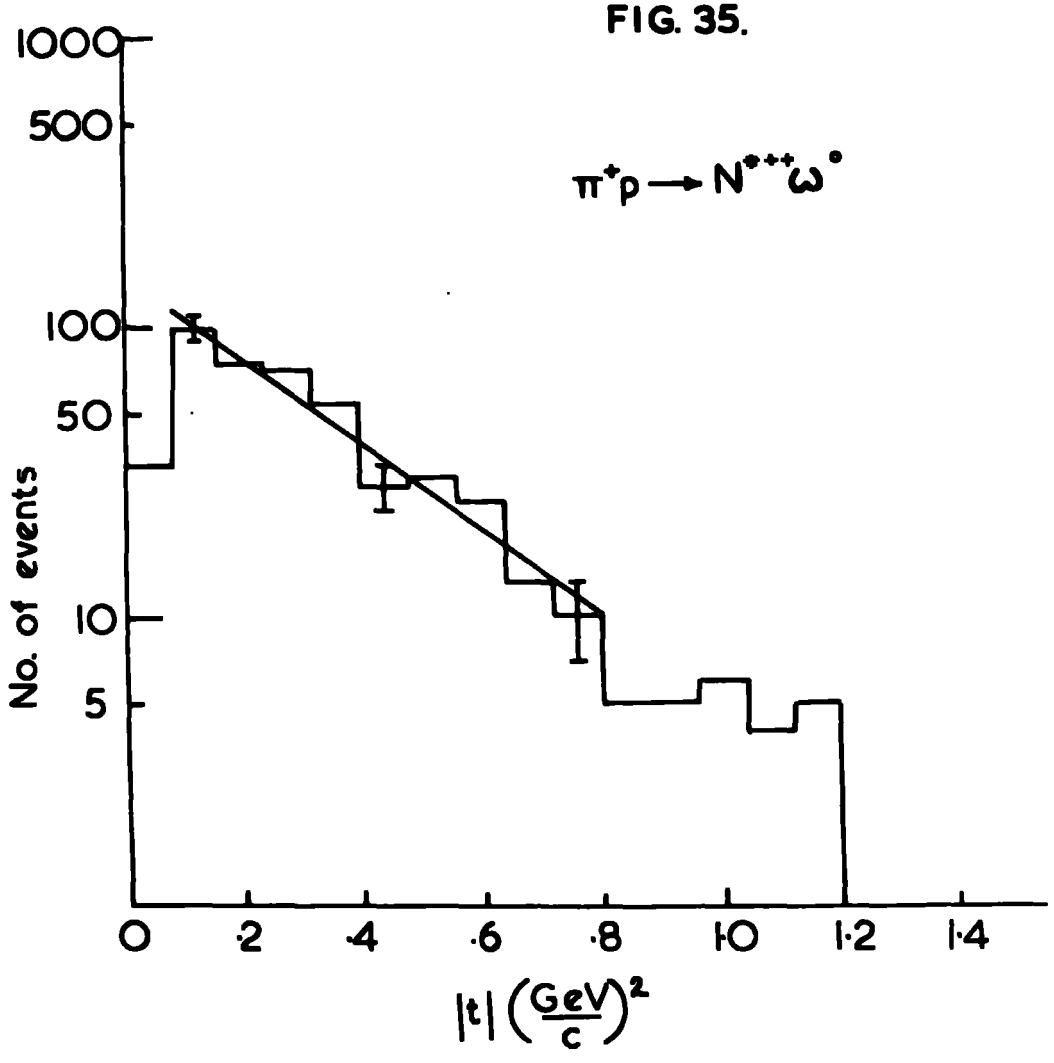
1000
500
100
50
10
5
No. of events
$\pi^+ p \rightarrow N^{*++} \omega^0$
0
·2
·4
·6
·8
1·0
1·2
1·4
$|t| \left(\frac{GeV}{c}\right)^2$

Figure 34(a) shows the distribution of $M(P\pi_1^+)$ in the ω^o band i.e. under the restriction $740 < M(\pi_2^+\pi^-\pi^o) < 823$ Mev and figure 34(b) shows the distribution of $M(\pi_2^+\pi^-\pi^o)$ in the N^{*++} band i.e. under the restriction $1140 < M(P\pi_1^+) < 1300$ Mev. From these distributions it is estimated (after subtracting a smooth background in each case) that (6±1)% of the channel (b) contributes to the reaction (i) and (0.4±0.1)% to the reaction (ii) above. The estimates of cross-sections (after correcting for unobserved decays of the ω^o and η^o) are (0.19±0.02) mb for the reaction (i) and (0.052±0.013) mb for the reaction (ii). These values of the cross-sections may be compared with the results of other experiments which are listed in Table 7.

The t-dependence of the reaction (i) is shown in figure 35 where the number of events is plotted as a function of $|t|$ i.e. $\Delta^2(\pi^+/\omega^o)$. A forward peak is observed but the distribution is much broader than the $N^{*++}\rho^o$ channel. The distribution over the interval of $|t|$ between 0.10 and 0.80 $(Gev/c)^2$ can be fitted by a simple exponential of the form $e^{-a|t|}$. The value of a obtained is $(3.6\pm0.2)\ (Gev/c)^{-2}$.

4.23 The A_2^o and $A_{2'}^+$ mesons

The A_2^o meson. The $\pi^+\pi^-\pi^o$ mass spectrum is shown (figure 36) for events in which the remaining π^+ forms a $P\pi^+$ combination in the N^{*++} band. An enhancement in the position of the A_2 meson is

FIG. 36

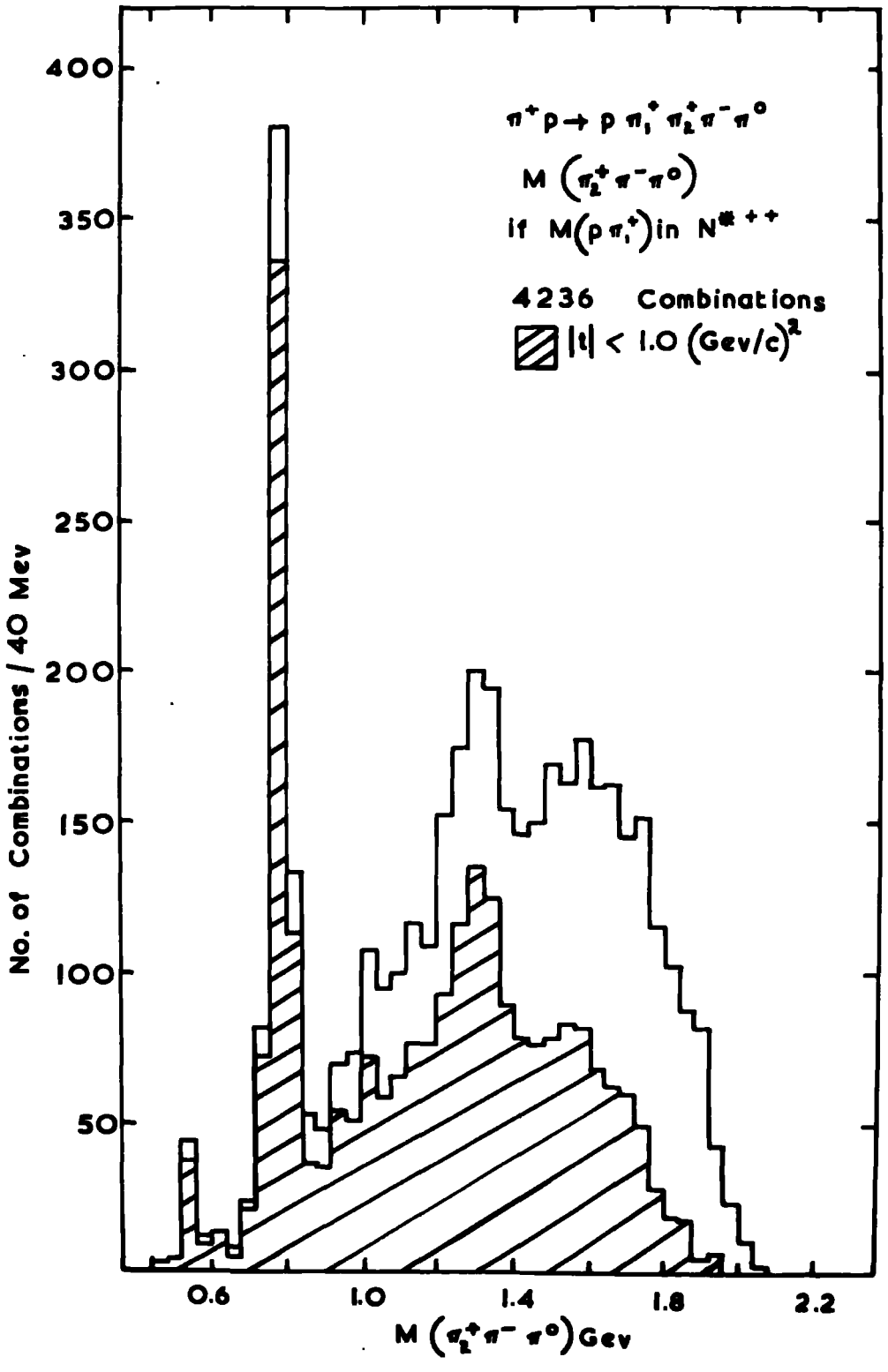
$\pi^+ p \to p\,\pi_1^+\,\pi_2^+\,\pi^-\,\pi^0$
$M\,(\pi_2^+\pi^-\pi^0)$
if $M(p\pi_1^+)$ in N^{*++}
4236 Combinations
$|t| < 1.0\ (\mathrm{Gev/c})^2$
No. of Combinations / 40 Mev
400
350
300
250
200
150
100
50
0.6
1.0
1.4
1.8
2.2
$M\,(\pi_2^+\pi^-\pi^0)$ Gev

FIG. 37

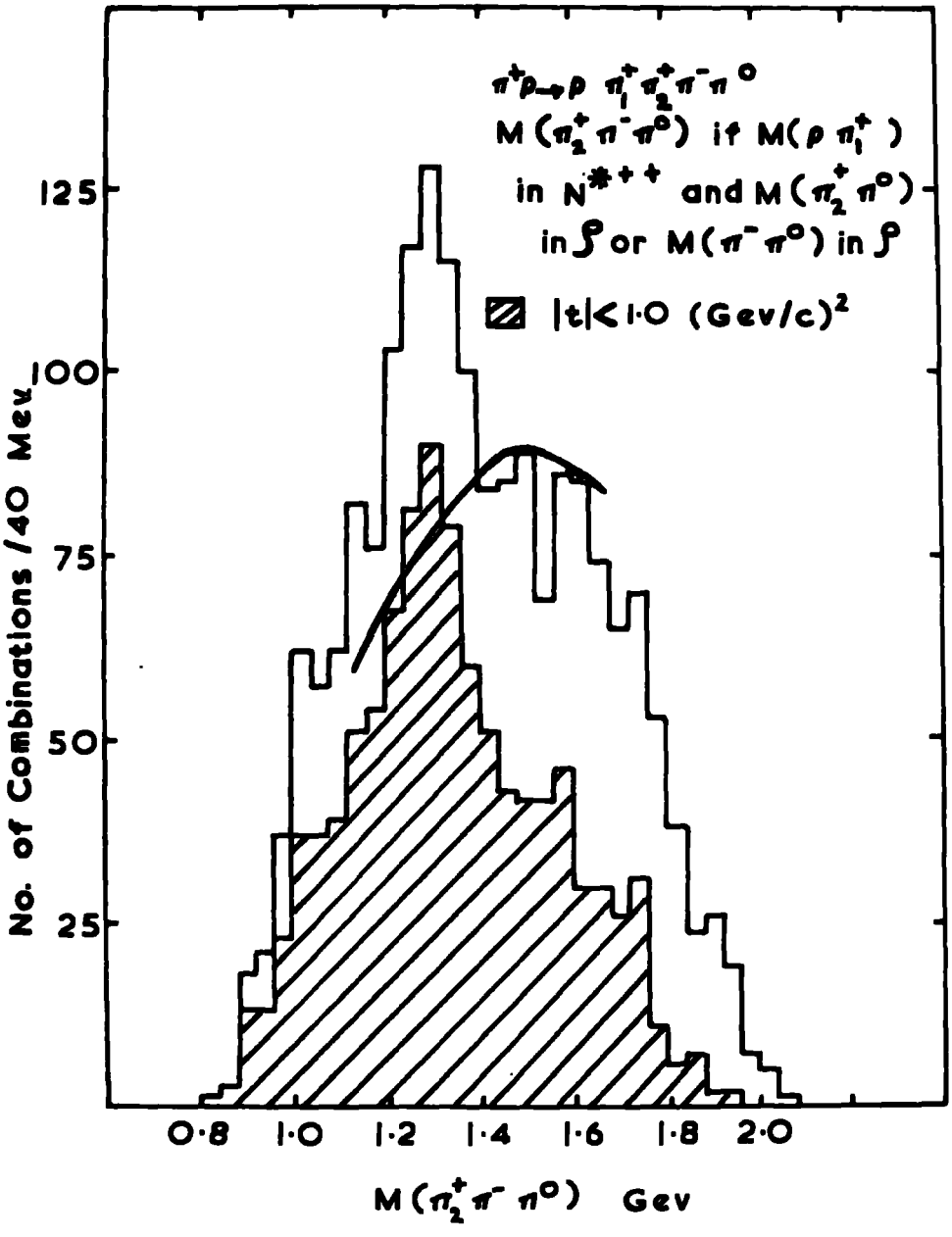
$\pi^+ p \to p\ \pi_1^+ \pi_2^+ \pi^- \pi^0$
$M(\pi_2^+ \pi^- \pi^0)$ if $M(p\ \pi_1^+)$ in N^{*++} and $M(\pi_2^+ \pi^0)$ in ρ or $M(\pi^- \pi^0)$ in ρ
$|t| < 1.0$ (Gev/c)^2
No. of Combinations /40 Mev
125
100
75
50
25
0·8
1·0
1·2
1·4
1·6
1·8
2·0
$M(\pi_2^+ \pi^- \pi^0)$ Gev

observed. This is identified as due to the A_2^o. No significant production of the A_2^o is observed unless in association with the N^{*++}. The shaded area in the histogram is obtained by restricting $|t| < 1.0$ (Gev/c)^2. The signal is correlated with the production of ρ^+ and ρ^-. Therefore, in figure 37 the $\pi^+\pi^-\pi^o$ mass spectrum is shown for those events in which, after the N^{*++} selection, a further condition is made that in the remaining three pions at least one $\pi^+\pi^o$ or $\pi^-\pi^o$ combination is in the ρ band. In this selection, the condition M $(\pi^+\pi^-)$ in the ρ band is not made because under the assumption of isospin I = 1, the $\rho^o\pi^o$ decay mode of the A_2 meson should not occur. The shaded area in figure 37 corresponds to the restriction of $|t| < 1.0$ (Gev/c)^2. The A_2^o distribution is compatible with a central mass value of (1300±15) Mev and a full width at half height of(100±20) Mev. By comparing the A_2^o enhancement in the shaded histogram, the background has been estimated by eye for the enhancement in the unshaded histogram (shown by the solid line in the figure). The excess of events above this background is counted as 236±20 which corresponds to the cross-section $\sigma(A_2^o \rightarrow \rho^{\pm}\pi)$ of (106±10)μb.

The A_2^+ meson

The A_2^+ is not detected in the $\pi^+\pi^+\pi^-$ mass spectrum shown in figure 38. The solid line in the figure is the $\pi^+\pi^+\pi^-$ phase space for the $p\pi^+\pi^+\pi^-\pi^o$ final state. However, the A_2^+ is observed in the

FIG. 38. $\pi^+ p \rightarrow p \pi^+ \pi^+ \pi^- \pi^0$

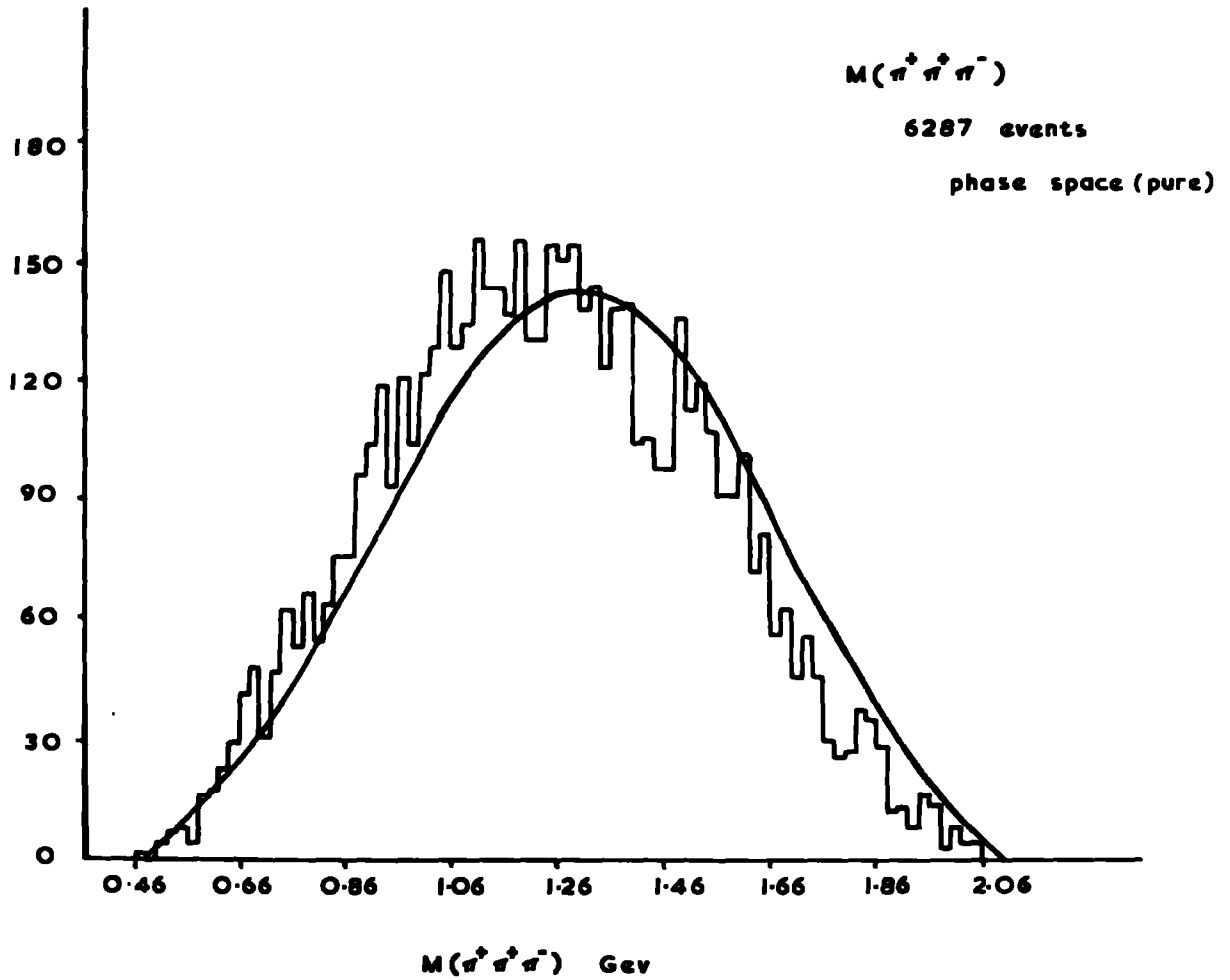

FIG. 39

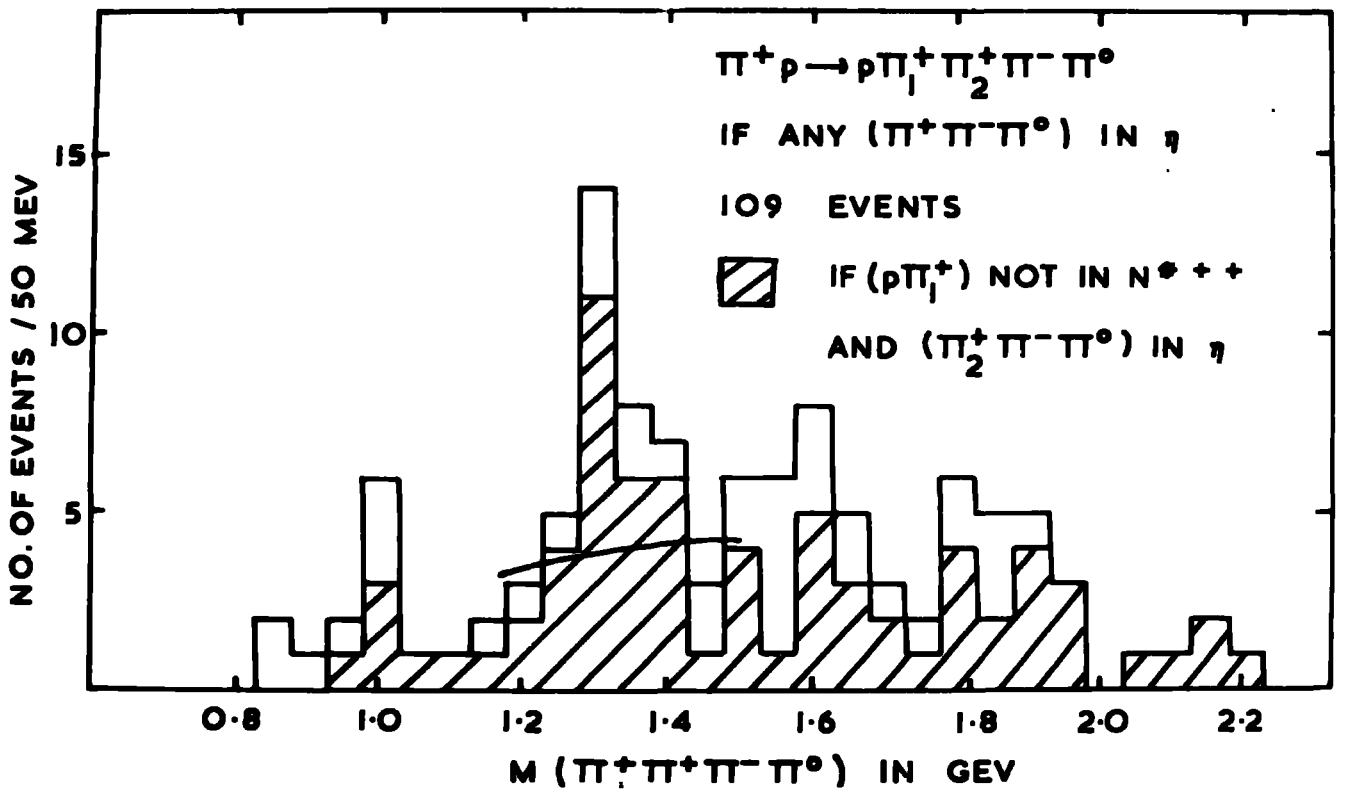
$\pi^+ p \rightarrow p\pi_1^+ \pi_2^+ \pi^- \pi^0$
IF ANY $(\pi^+\pi^-\pi^0)$ IN η
109 EVENTS
IF $(p\pi_1^+)$ NOT IN N^{*++}
AND $(\pi_2^+ \pi^- \pi^0)$ IN η
NO. OF EVENTS / 50 MEV
15
10
5
0·8
1·0
1·2
1·4
1·6
1·8
2·0
2·2
M $(\pi^+\pi^+\pi^-\pi^0)$ IN GEV

FIG. 40

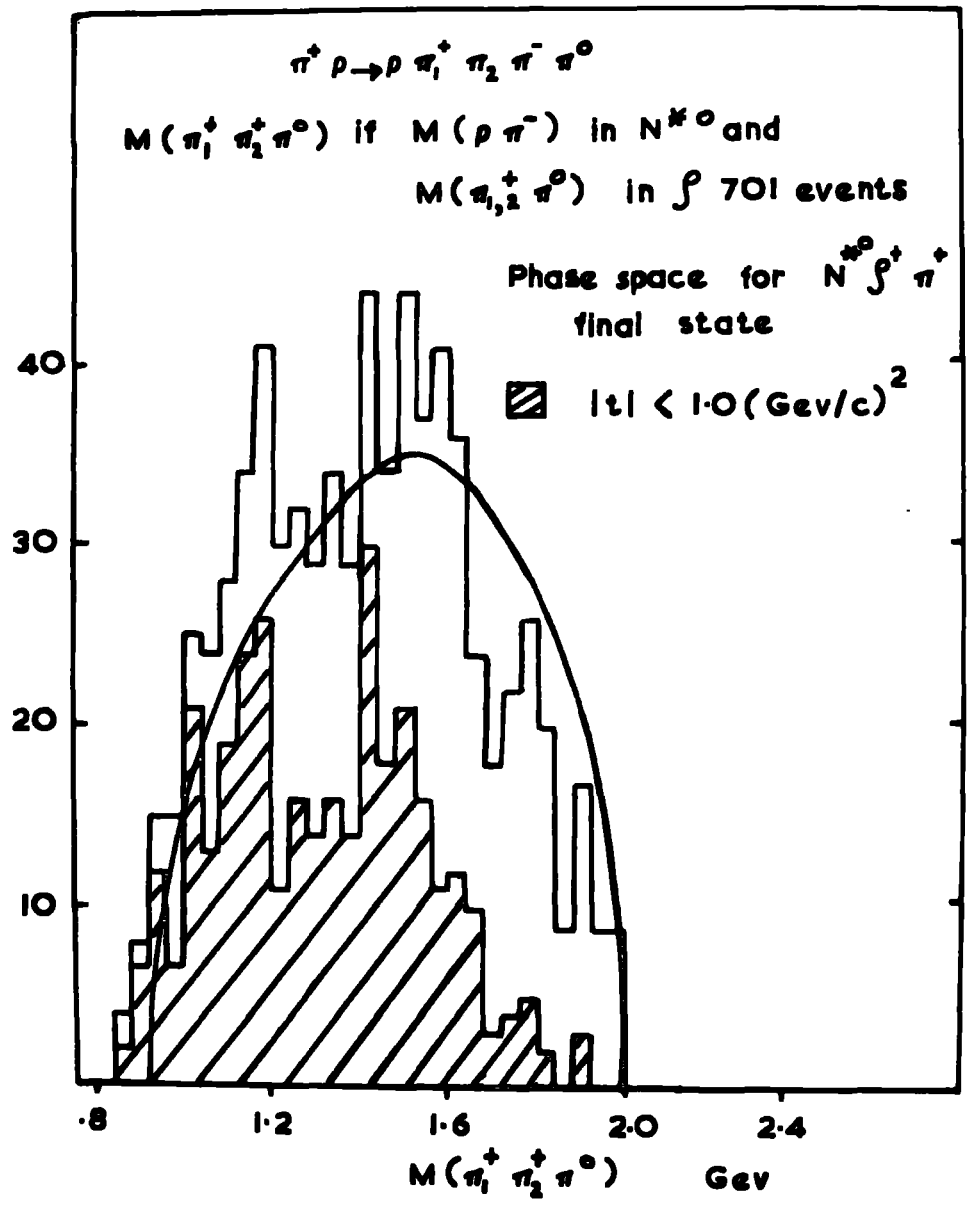
$\pi^+ p \to p \pi_1^+ \pi_2 \pi^- \pi^0$
$M(\pi_1^+ \pi_2^+ \pi^0)$ if $M(p \pi^-)$ in N^{*0} and
$M(\pi_{1,2}^+ \pi^0)$ in ρ 701 events
Phase space for $N^{*0} \rho^+ \pi^+$ final state
$|t| < 1.0 (Gev/c)^2$
40
30
20
10
·8
1·2
1·6
2·0
2·4
$M(\pi_1^+ \pi_2^+ \pi^0)$ Gev

reaction $\pi^+p \rightarrow N^{*++} A_2^+$. This is shown later in section 4.32 in figure 48(A).

The A_2^+ is also observed in the four pion mass spectrum $M(\pi^+\pi^+\pi^-\pi^0)$ under the restriction that at least one $\pi^+\pi^-\pi^0$ combination is in the η^0 band defined as $535 < M(\pi^+\pi^-\pi^0) < 565$ Mev. This is shown in figure 39 in which a significant peak at the mass position of the A_2 can be seen. The shaded area in the figure corresponds to those events in which the π^+ left after the η selection does not form a $p\pi^+$ combination in the N^{*++} band. This is done to exclude the $N^{*++}\eta^0$ events. The position of the peak remains unaffected by this procedure; the central mass value and the full width at half height are compatible with (1300±25) Mev and (100±50) Mev.

The enhancement has been identified as the $\eta\pi^+$ decay mode of the A_2^+. In the shaded histogram an excess of 11±4 events is counted above a smooth background. This corresponds to the cross-section $\sigma(A_2^+ \rightarrow \eta^0\pi^+)$ of (5±2) μb, with the η decaying into $\pi^+\pi^-\pi^0$.

In figure 40 is shown the $\pi^+\pi^+\pi^0$ mass spectrum under the assumption that the $p\pi^-$ combination is in the N^{*0} band and that at least one $\pi^+\pi^0$ combination is in the ρ band. No signal is observed in the A_2 region i.e. there is no production of A_2^{++}. This rules out the assignment of isospin I = 2 for the A_2 meson. Under the assumption of I = 2 for the A_2, the signal is expected to be $\frac{2}{3}$ of the A_2^0 signal which would mean about 160 events above the background.

FIG. 41

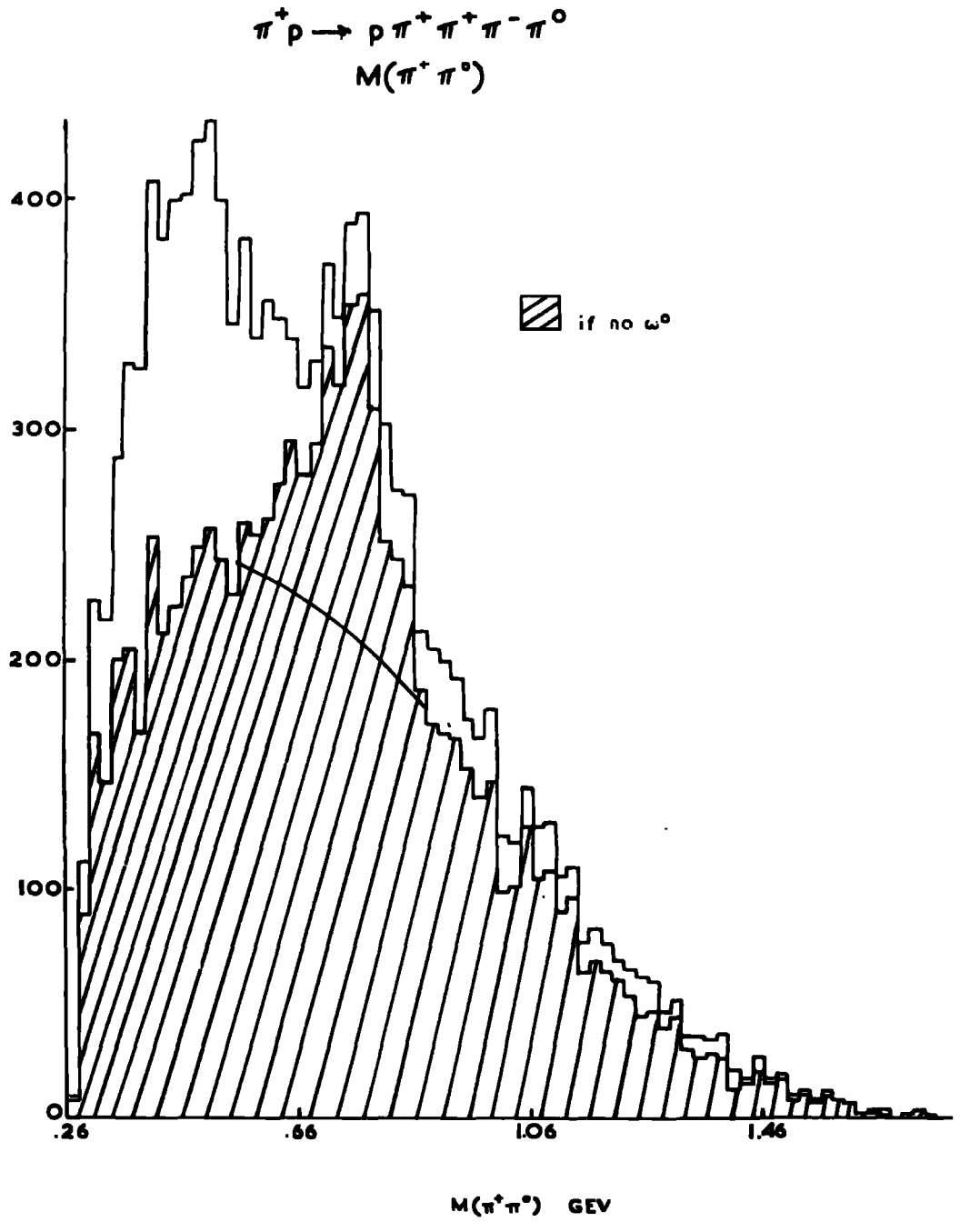
$\pi^+ p \rightarrow p\pi^+\pi^+\pi^-\pi^0$
$M(\pi^+\pi^0)$
400
300
200
100
0
.26
.66
1.06
1.46
if no ω^0
$M(\pi^+\pi^0)$ GEV

FIG. 42.

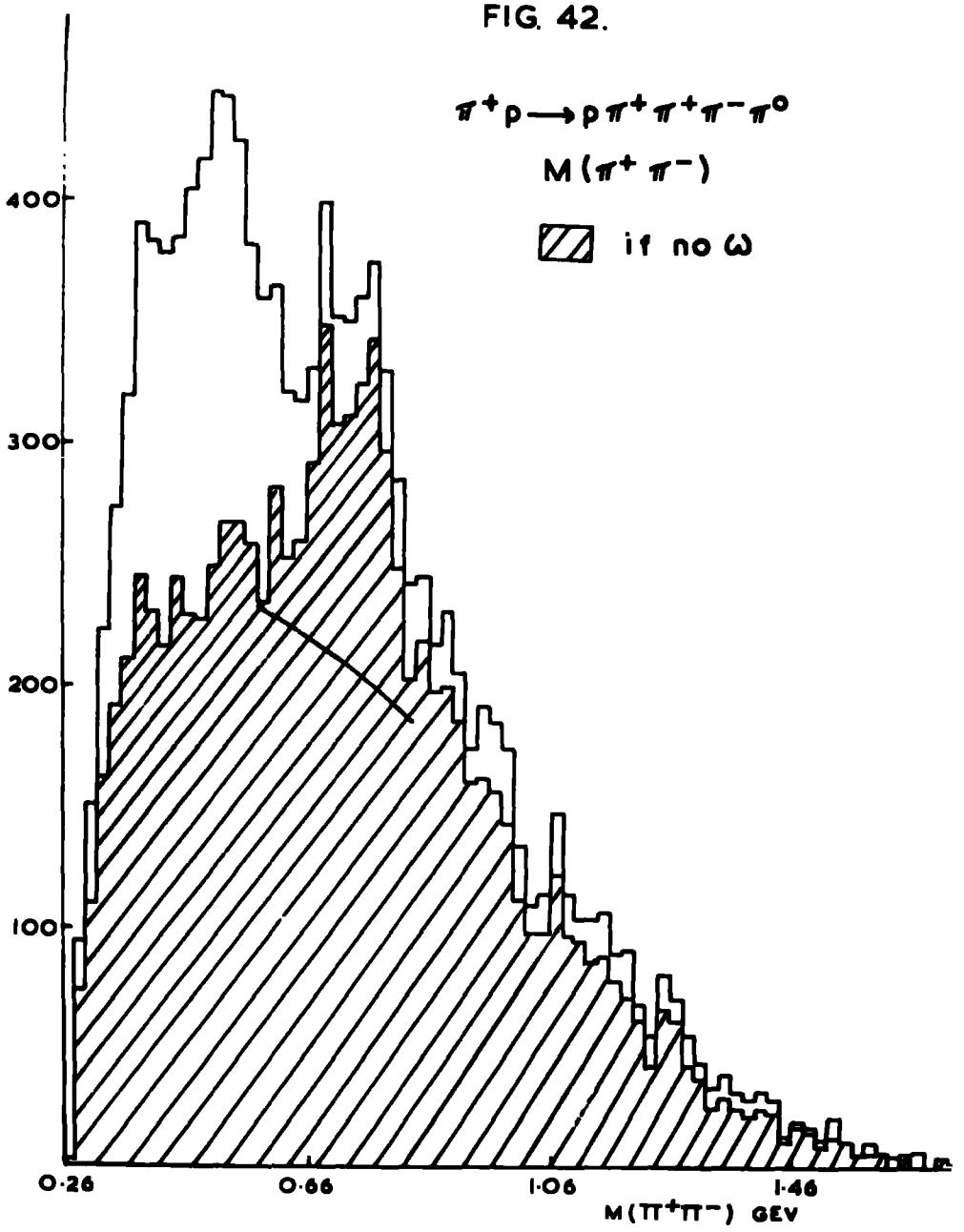
$\pi^+ p \longrightarrow p\pi^+\pi^+\pi^-\pi^0$
$M(\pi^+\pi^-)$
if no ω
400
300
200
100
0·26
0·66
1·06
1·46
$M(\pi^+\pi^-)$ GEV

FIG. 43

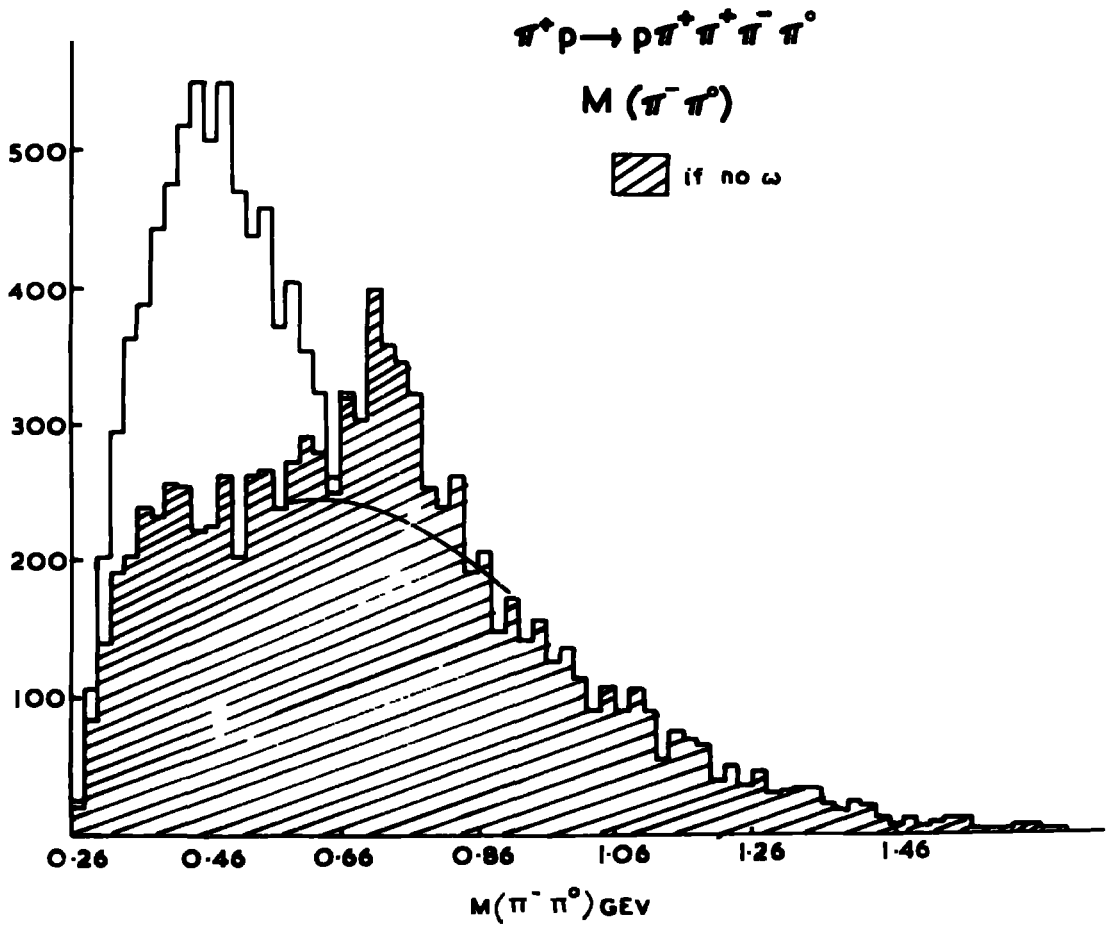
$\pi^+ p \rightarrow p\pi^+\pi^+\pi^-\pi^0$
M ($\pi^-\pi^0$)
if no ω
500
400
300
200
100
0·26
0·46
0·66
0·86
1·06
1·26
1·46
M($\pi^-\pi^0$) GEV

4.24 The ρ meson

The ρ meson is observed in its three charged modes in the $\pi^+\pi^0$, $\pi^+\pi^-$ and $\pi^-\pi^0$ mass spectra which are shown in figures 41, 42 and 43. The shaded area in each histogram corresponds to those events in which there is no $\pi^+\pi^-\pi^0$ combination in the ω band which is defined as 783±40 Mev. The ρ signals are improved in the shaded histograms. By counting the excess of events above a smooth background in each of the shaded histograms, the cross-sections are estimated as (0.50±0.10) mb, (0.58±0.18) mb and (0.40±0.10) mb for the ρ^+, ρ^0 and ρ^- respectively.

4.25 The B^+ meson

All the observed ω mesons are not produced in association with the N^{*++}. Consequently an attempt was made to look for the production of the B meson in the ωπ mass spectrum. Figure 44 shows the four pion mass distribution selected from events in which at least one $\pi^+\pi^-\pi^0$ combination is in the ω band. An indication for the production of the B^+ is observed. The background is reduced, as shown by the shaded histogram, which has been drawn for events in which the π^+ after ω selection does not form a $p\pi^+$ effective mass in the N^{*++} band. The B^+ signal is somewhat improved. The enhancement is centred at about 1240 Mev and has a width of about 140 Mev. By subtracting a smooth background under the B^+ enhancement in the shaded histogram the cross-section $\sigma(B^+ \rightarrow \omega\pi^+)$ is estimated as (105±20) μb.

FIG. 44.

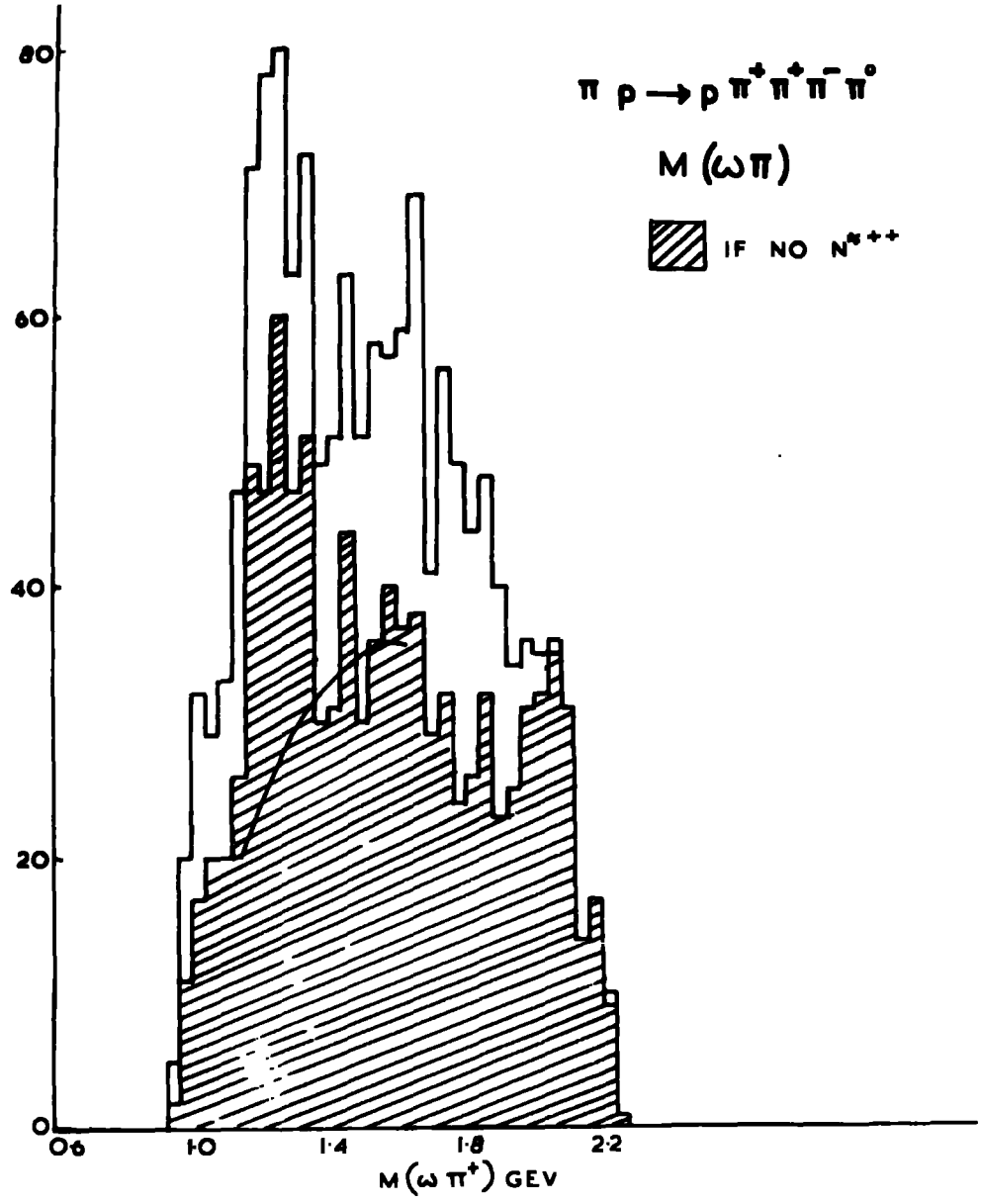

FIG. 45

$\pi^+ p \rightarrow p\pi^+\pi^+\pi^-\pi^0$

$M^2(p\pi^+)$ vs $M^2(\omega\pi^+)$

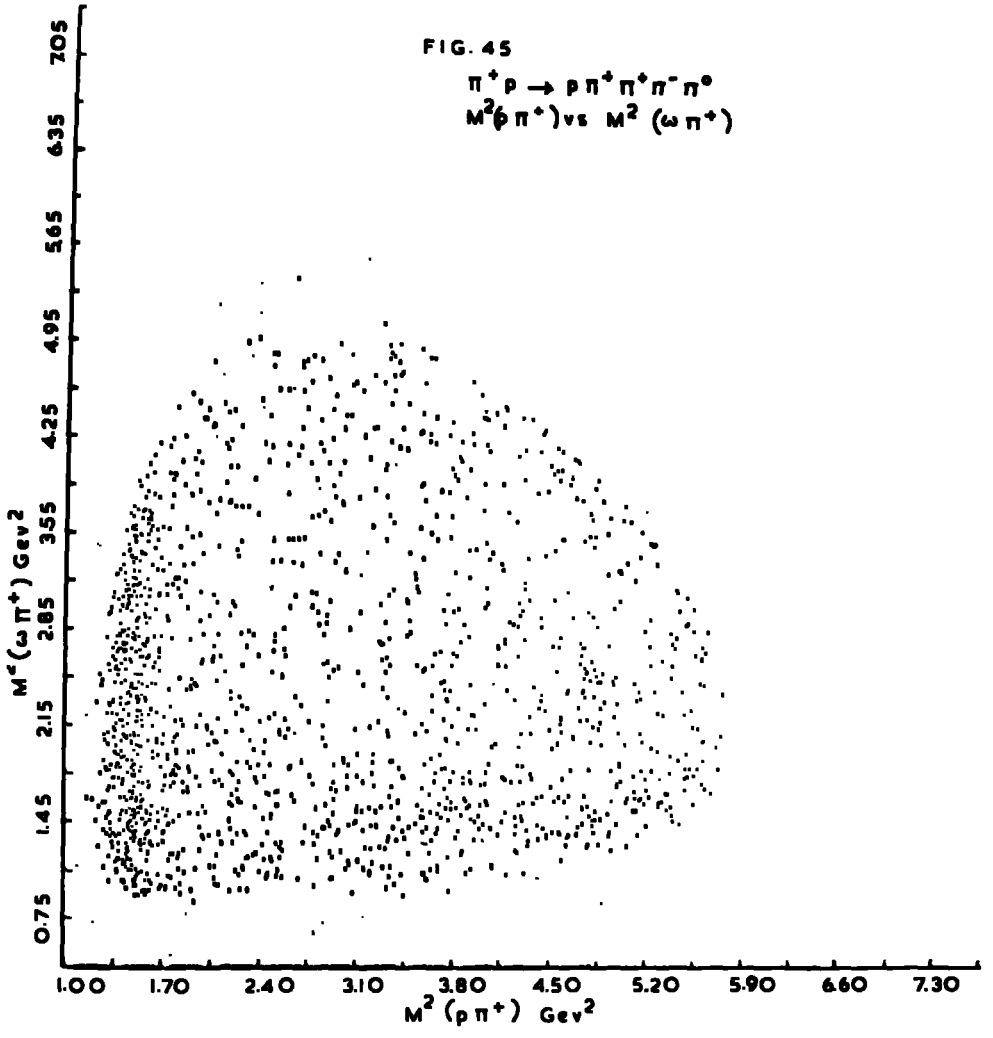

FIG. 46.

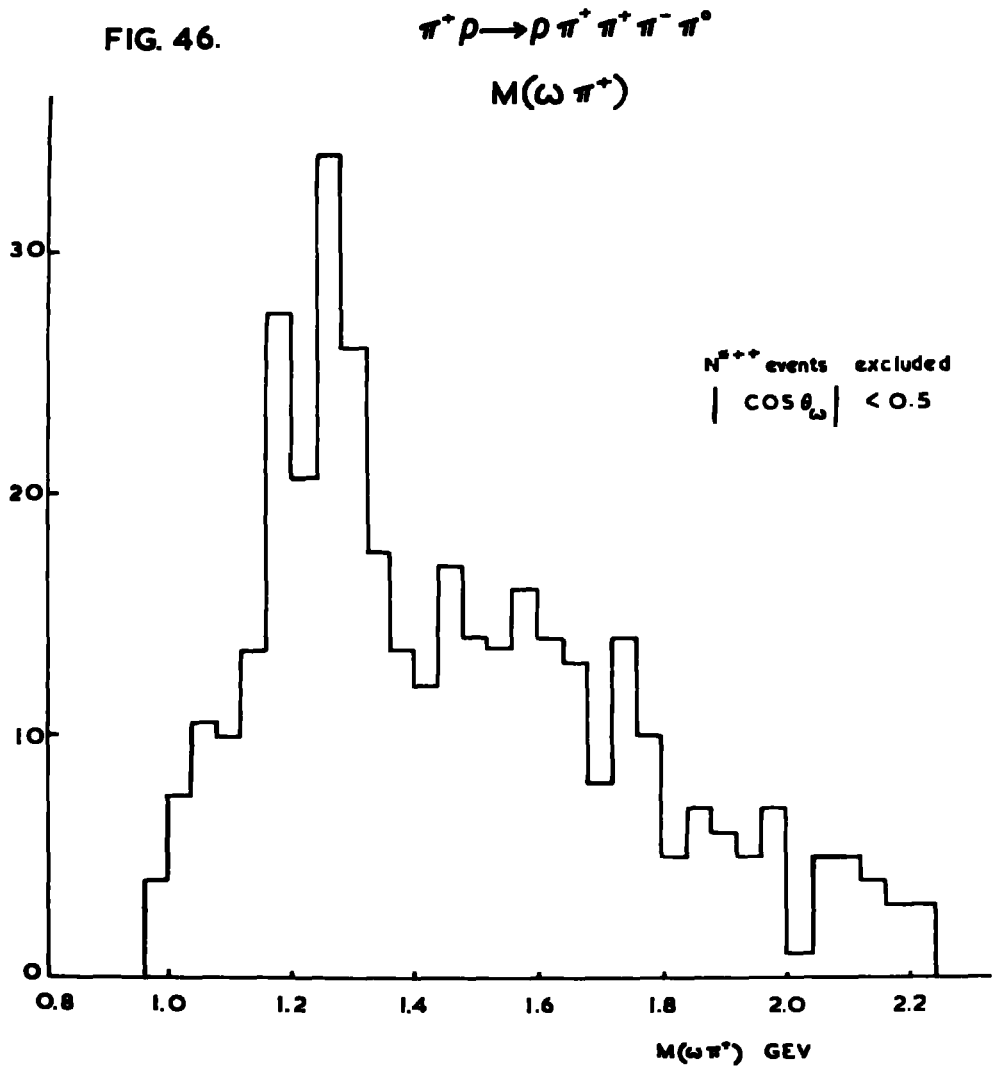
$\pi^+ p \longrightarrow p\,\pi^+\pi^+\pi^-\pi^0$
$M(\omega\,\pi^+)$
30
20
10
0
$N^{\pi^{++}}$ events excluded
$|\cos\theta_\omega| < 0.5$
0.8
1.0
1.2
1.4
1.6
1.8
2.0
2.2
$M(\omega\pi^+)$ GEV

FIG. 47.

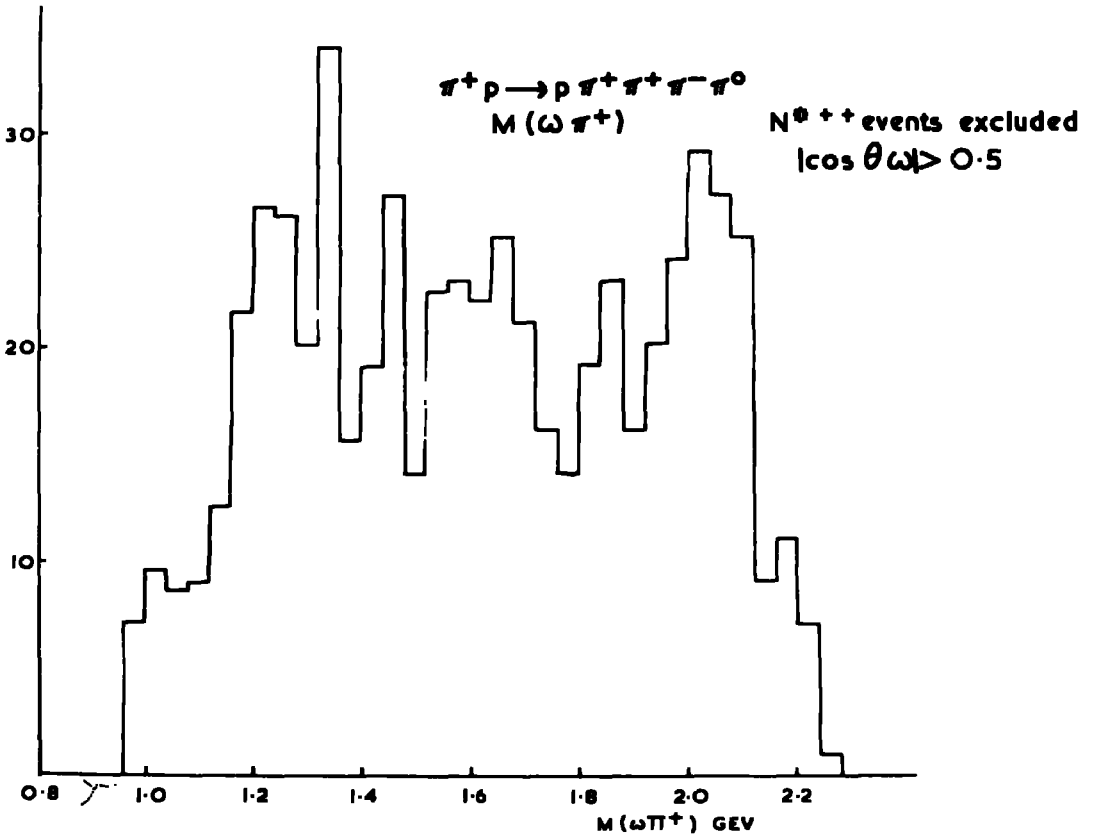
$\pi^+ p \longrightarrow p\,\pi^+\pi^+\pi^-\pi^0$
$M(\omega\pi^+)$
N^{*++} events excluded
$|\cos\theta_{\omega}| > 0.5$
30
20
10
0·8
1·0
1·2
1·4
1·6
1·8
2·0
2·2
$M(\omega\pi^+)$ GEV

Figure 45 shows the Dalitz plot $M^2(P\pi^+)$ versus $M^2(\omega\pi^+)$ for the reaction $\pi^+P \rightarrow P\pi^+\omega$. An approximately uniform distribution along the B^+ mass band is observed. This indicates a J^P assignment of 1^+ for the B meson.

A better selection of the B^+ is observed when restricting to events in which the ω is emitted at large angles with respect to the incident π^+ in the $\omega\pi$ rest frame. This is shown in figure 46 where the $\omega\pi$ mass distribution has been obtained by restricting $|\text{Cos}\theta_\omega| < 0.5$. The complementary distribution for the restriction $|\text{Cos}\theta_\omega| \geq 0.5$ is shown in figure 47. The observed strong decay of the B^+ at large angles supports the idea of its isotropic decay which is predicted by the $J^P = 1^+$ assignment.

4.31 Decay branching ratios of the A_2

The decay branching ratios of the A_2 have been determined from the following observed decay modes of the A_2^+.

(i) In channel (a) the A_2^+ is observed in the decay mode $A_2^+ \rightarrow \rho^o\pi^+$ with the ρ^o decaying into $\pi^+\pi^-$. In section 4.14 the cross-section $\sigma(A_2^+ \rightarrow \rho^o\pi^+)$ has been estimated as (63 ± 10) μb. Under the assumption of isospin I = 1 for the A_2, a signal of equal strength is expected for the unobserved decay mode $A_2^+ \rightarrow \rho^+\pi^o$ with the ρ^+ decaying into $\pi^+\pi^o$. Thus the cross-section $\sigma(A_2^+ \rightarrow \rho^+\pi^o)$ is estimated to be (126 ± 15) μb.

(ii) In channel (b), the A_2^+ is observed in the decay mode $A_2^+ \rightarrow \eta\pi^+$ with the η decaying into $\pi^+\pi^-\pi^o$. From the value obtained in section 4.23 and using a factor 4 to correct for the unseen decays of the η the cross-section $\sigma(A_2^+ \rightarrow \eta\pi^+)$ is found to be (20±8) μb.

(iii) In chapter 5, section 5.6(i) it has been shown that in the reaction $\pi^+p \rightarrow pK^+\bar{K}^o$ the A_2^+ is observed in the decay mode $A_2^+ \rightarrow K^+\bar{K}^o$. The cross-section $\sigma(A_2^+ \rightarrow K^+\bar{K}^o)$ has been estimated after correcting for the unseen decays of the $\bar{K}^o$ and a value of (11±6) μb has been obtained.

From these results the branching ratios of the A_2 for the $\eta\pi$ decay mode relative to the $\rho\pi$ decay mode is found to be

$$\frac{A_2 \rightarrow \eta\pi}{A_2 \rightarrow \rho\pi} = (16\pm6)\%$$

The value of this branching ratio has been determined in a number of experiments and different values ranging from (9±4)% to (30±20)% have been obtained (Morrison, 1967).

The other branching ratio is

$$\frac{A_2 \rightarrow K\bar{K}}{A_2 \rightarrow \rho\pi} = (9\pm4)\%$$

This value may be compared with the values of (5±2)% and (4±2)% which have been obtained in experiments at 4.2 Gev/c and 8 Gev/c π^+p (Morrison, 1967).

The large discrepancies between the results of different experiments in determining the A_2 branching ratios are due to the problem of estimating the background in the $\rho\Pi$ effective mass spectrum.

As in the case of the A_2^+, the A_2^o (which is observed in the $\rho\Pi$ decay mode in the reaction $\Pi^+P \rightarrow N^{*++}A_2^o$ in channel (b))is also expected to be observed in the $K\bar{K}$ decay mode. In chapter 5, section 5.6(ii) where the two reactions $\Pi^+P \rightarrow P\Pi^+K^+K^-$ and $\Pi^+P \rightarrow P\Pi^+K^o\bar{K}^o$ have been described, are shown the two dimensional scatter plots $M(P\Pi^+)$ versus $M(K^+K^-)$ in figure 65(a) and $M(P\Pi^+)$ versus $M(K^o\bar{K}^o)$ in figure 64(a). In both these plots a concentration of events is observed in the N^{*++} band at a $K\bar{K}$ mass value of about 1300 Mev. This gives evidence for the $K\bar{K}$ decay mode of the A_2^o. However a determination of the A_2^o partial cross-section for its $K\bar{K}$ decay mode was not considered reliable because of insufficient data and the problem of background estimation. So the decay branching ratios of the A_2^o are not calculated.

4.32 Isospin of the A_2 meson

It has been shown in section 4.23 that in the $\rho^+\Pi^+$ mass spectrum no signal is observed in the A_2 region which rules out the isospin assignment I = 2 for the A_2 meson.

Recently Baltay et al (1967) have studied the production rates of the A_2 in its different charged states in the reactions $\Pi^+P \rightarrow N^{*++}A_2^o$

and $\pi^+P \rightarrow N^{*+}A_2^+$ and have arrived at the value of I = 1 for the A_2 meson. Under the assumption of isospin conservation the cross-sections are related by Glebsch Gordon co-efficients. If the cross-section for the reaction $\pi^+P \rightarrow N^{*+}A_2^+ \,|_{\rightarrow n\pi^+}\,|_{\rightarrow \rho^0\pi^+}$ is arbitrarily normalised to 1, then under the assumption of I = 1 for the A_2 meson, the values of the cross-sections for the different reactions are expected to be

$$\pi^+P \rightarrow N^{*++}\,|_{\rightarrow P\pi^+}\; A_2^0\,|_{\rightarrow \rho^\pm\pi^\mp} = 9$$

$$\rightarrow N^{*+}\,|_{\rightarrow P\pi^0}\; A_2^+\,|_{\rightarrow \rho^0\pi^+} = 2$$

$$\rightarrow N^{*+}\,|_{\rightarrow \eta\pi^+}\; A_2^+\,|_{\rightarrow \rho^0\pi^+} = 1$$

In the present analysis an attempt has been made to check the above hypothesis.

In figure 48(a) the $\pi^+\pi^+\pi^-$ effective mass distribution is shown for the channel $P\pi^+\pi^+\pi^-\pi^0$ under the condition that the $P\pi^0$ conbination is in the N^* band and that at least one $\pi^+\pi^-$ combination is in the ρ band. The solid line gives the phase space for a $N^*\rho\pi$ final state. The shaded area corresponds to a cut of $|t| < 1.0(\text{Gev/c})^2$. An enhancement in the A_2 region is observed. By counting the number of events in the A_2 region above a smooth background which is suggested by the shaded histogram, the number obtained for the

reaction $\pi^+ P \to \underset{\lfloor\to P\pi^0}{N^{*+}} \;\; \underset{\lfloor\to \rho^0\pi^+}{A_2^+}$ is (40±20) events.

Again, by taking the neutron channel, i.e. the channel $\pi^+ P \to n\pi_1^+\pi_2^+\pi_3^+\pi^-$, the $\pi_2^+\pi_3^+\pi^-$ mass spectrum is shown in figure 48(B) under the condition that $M(n\pi_1^+)$ is in the N^* band and at least one $\pi_{2,3}^+\pi^-$ combination is in the ρ band. The solid line is the phase space for the $N^*\rho\pi$ final state. The shaded area in the histogram corresponds to a cut of $|t| < 1.0$ (Gev/c)². A signal is observed in the A_2 region. By counting the number of events in the A_2 region above a smooth background the number obtained for the reaction $\pi^+ P \to \underset{\lfloor\to n\pi^+}{N^{*+}} \;\; \underset{\lfloor\to \rho^0\pi^+}{A_2^+}$ is (25±10) events.

In section 4.23 the number of events corresponding to the reaction $\pi^+ P \to \underset{\lfloor\to P\pi^+}{N^{*++}} \;\; \underset{\lfloor\to \rho^\pm\pi^\mp}{A_2^0}$ has been obtained as (236±20). With these numbers the experimental ratio is

$$\underset{\lfloor\to P\pi^+}{N^{*++}} \;\; \underset{\lfloor\to \rho^\pm\pi^\mp}{A_2^0} \quad : \quad \underset{\lfloor\to P\pi^0}{N^{*+}} \;\; \underset{\lfloor\to \rho^0\pi^+}{A_2^+} \quad : \quad \underset{\lfloor\to n\pi^+}{N^{*+}} \;\; \underset{\lfloor\to \rho^0\pi^+}{A_2^+}$$

$$= \quad 9 \quad : \quad (1.5 \pm 0.7) \quad : \quad (0.9 \pm 0.4)$$

This result is in good agreement with the ratio of 9 : 2 : 1 expected from the I = 1 assignment for the A_2 meson.

FIG. 48

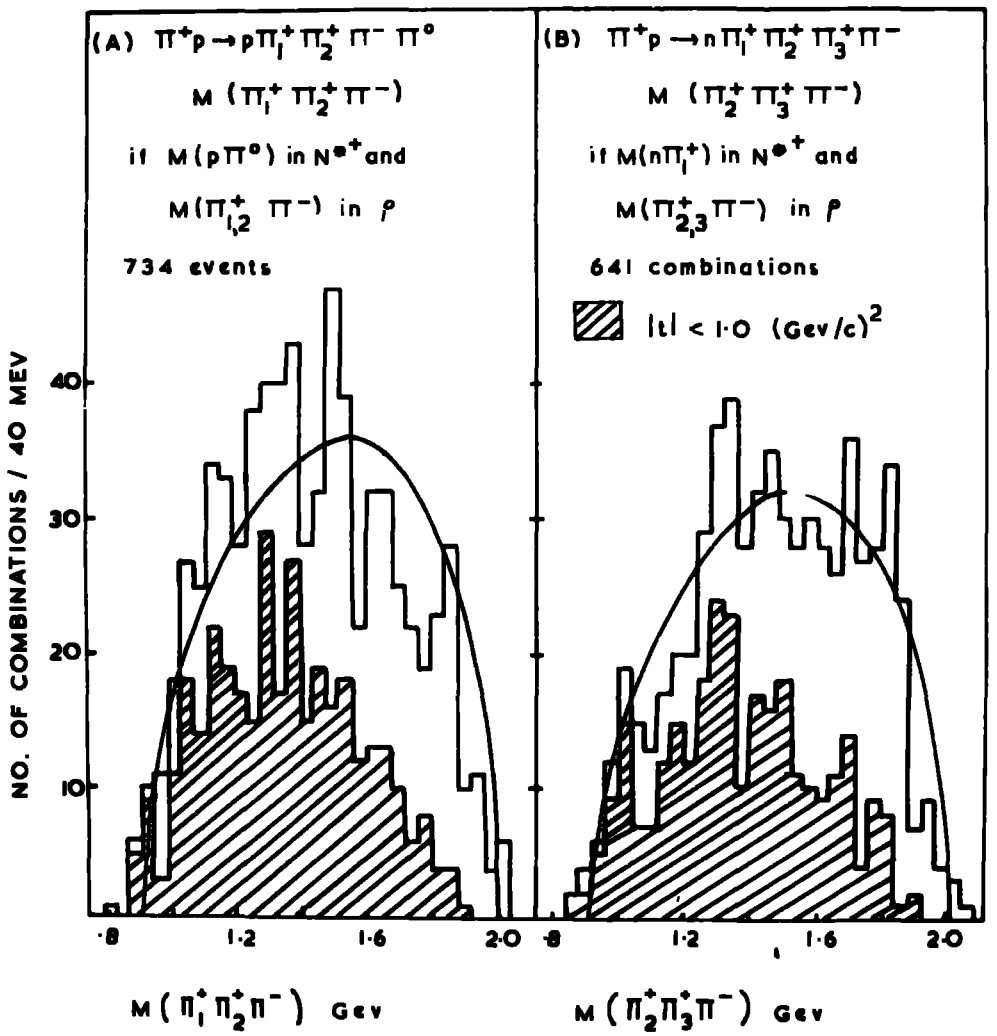
(A) $\pi^+p \to p\pi_1^+\pi_2^+\pi^-\pi^0$
M $(\pi_1^+\pi_2^+\pi^-)$
if M$(p\pi^0)$ in N^{*+} and
M$(\pi_{1,2}^+\pi^-)$ in ρ
734 events
(B) $\pi^+p \to n\pi_1^+\pi_2^+\pi_3^+\pi^-$
M $(\pi_2^+\pi_3^+\pi^-)$
if M$(n\pi_1^+)$ in N^{*+} and
M$(\pi_{2,3}^+\pi^-)$ in ρ
641 combinations
$|t| < 1{\cdot}0$ (Gev/c)^2
NO. OF COMBINATIONS / 40 MEV
40
30
20
10
·8
1·2
1·6
2·0
M $(\pi_1^+\pi_2^+\pi^-)$ Gev
M $(\pi_2^+\pi_3^+\pi^-)$ Gev

CHAPTER 5

Analysis of the Strange Particle Events

5.1 Introduction

In this chapter a description is given of the production of strange particles in the two-prong V^o events together with the events ($\pi^+p \rightarrow p\pi^+K^+K^-$) which were identified in the analysis of the 4 prong events described in Chapter 3. The V^o events were scanned for at least one visible V^o decay. The relative numbers of 2 and 4 prong events with at least one visible V^o are such as to justify a detailed analysis only in the case of the 2 prong events. The cross-sections for the various strange particle reactions are given later and compared with the values obtained in other experiments at different pion momenta. The two particle effective mass distributions in the three and four particle final states with ΛK and $K\bar{K}$ production are studied. In the ΛK channels strong production of the resonances $Y_1^*(1385)$ and $K^*(890)$ is observed. The quasi two-body reactions $\pi^+p \rightarrow Y_1^{*+}K^+$ and $\pi^+p \rightarrow Y_1^{*+}K^{*+}$ are investigated by a comparison of the respective $\frac{d\sigma}{dt}$ distributions with the prediction of the absorption model. In the $K\bar{K}$ channels the dominant features are the production of $N^*(1236)$ and $K^*(890)$. Besides, there is evidence for $\kappa(730)$ production and an indication of the Φ meson.

A short description of the method of analysis and the results are presented in the following sections.

5.2 Method of Analysis

Scan Results (Durham Sample)

Table 8 shows the number of events found in the first scan. The scanning efficiencies have been calculated on the basis of the numbers obtained in scan and rescan. Corrections were made for spurious events, i.e. the events in which the V^o was wrongly associated. These spurious events were detected during the checking of Grind hypotheses. About 10% of the 2 prong 1 V^o events and 25% of the 4 prong 1 V^o events were found to have a 'kink' track which were mostly charge decays.

TABLE 8

Scan Results of V^o Events (Durham Sample)

Type	No. of events found in 1st scan	Scanning Efficiency
2-prong with 1 V^o	232	0.985
2-prong with 2 V^o	18	1.000
4-prong with 1 V^o	49	0.970
4-prong with 2 V^o	3	1.000
6-prong with 1 or 2 V^o	0	

The number of V^o events found in each class was consistent with the scan results of the other collaborating laboratories.

Measurement

The events were measured on the same general principles as the 4 prong events. Additional labelling schemes were made for the V^o and V^+ decay vertices and the outgoing tracks from these vertices. Special labels were used for identified and stopping tracks. A track with a short kink, was assumed to be a charged V^o decay and then only the decay vertex and the charged track issuing out of the point of decay were measured. About 5% of the events were unmeasureable because of short and straight secondaries and faintness of the tracks issuing from a V^o decay vertex. The events were remeasured on the basis of the same tests in Thresh and Grind as were chosen for the 4 prong events (c.f. section 3.7).

Data Processing

As in the case of the 4 prong events, the V^o events were processed in the chain of computer programs Reap-Thresh-Grind-Slice-Sumx. Grind had some additional features for the kinematical fitting of the V^o events, namely:

(i) A fit was given for the V^o vertex. This is a 3 constraint fit as the only unknown at the V^o vertex is the momentum of the V^o.

(ii) Tracks with kinks were considered in the mass assignments to be Σ^+ hyperons. For kinks close to the production vertex, the Σ^+ was reconstructed at the kink from measurements of the track beyond this assumed point/decay. The lifetime of

the Σ^+ is such that its decay length in the chamber is of the order of a few centimetres. For a K^+ mass assignment the track issuing out of the kink was not considered since the lifetime of the K^+ is so great that the majority of them decay outside the chamber or sufficiently remote from the production vertex so that a good measure of the curvature of the track is obtained.

(iii) A single-vertex fit was given in which all the tracks belonging to the primary vertex (including that of any unobserved neutral particle) were used in a constraint fit.

(iv) Finally, a multi-vertex fit was given in which all the tracks of the primary vertex and the V^o vertices were fitted in an overall constraint.

Hypotheses for V^o Events

The general scheme of hypotheses for the V^o events was made for reactions which involved the production of one pair of strange particles. The possible reaction channels tried for the 2 prong V^o events were:

(A) Two prong with One observed V^o

$\pi^+p \rightarrow$

(1) $pK^+\bar{K}^o$

(2) $\pi^+K^+\Lambda^o$

(3) $\pi^+\Sigma^+K^o$

(4) $\pi^+K^+\Sigma^o$

(5) $pK^+K^o(\pi^o)$

(6) $\pi^+K^+\Lambda^o(\pi^o)$

(7) $\pi^+\Sigma^+K^o(\pi^o)$

(8) $\pi^+pK^o(\bar{K}^o)$

(9) $\pi^+\pi^+\Lambda^o(K^o)/\pi^+\pi^+ K^o(\Lambda^o)$

(10) $\pi^+\pi^+K^o(\Sigma^o)$

(11) $\pi^+K^+\bar{K}^o(n)$

(B) Two prong with two observed V^o's

$\pi^+p \rightarrow$

(12) $\pi^+pK^o\bar{K}^o$

(13) $\pi^+\pi^+K^o\Lambda^o$

(14) $\pi^+\pi^+K^o\Sigma^o$

(15) $\pi^+pK^o\bar{K}^o(\pi^o)$

(16) $\pi^+\pi^+\Lambda^oK^o(\pi^o)$

(17) $\pi^+\pi^+K^o\bar{K}^o(n)$

The symbols inside the parentheses indicate the unobserved neutral particles.

In both (A) and (B) all the reactions with no unobserved neutral particle were of the four constraint type and those with an unseen neutral particle were of the one constraint type in the single vertex fit.

Event Identification

The V^o events were identified on the bases of χ^2 probability and compatibility of ionisation. The value of the χ^2 considered was the one obtained for the single vertex fit. Since a single-vertex fit

was either of the one constraint type or of the four constraint type, the χ^2 limits chosen were the same as for the 4 prong events, namely $\chi^2 \leq 6$ for a 1C fit and $\chi^2 \leq 25$ for a 4C fit. The bubble density recognition limit for a proton was about 1300 MeV/c and for a kaon 700 MeV/c of momentum.

The table 9) gives the numbers of the events in the combined sample of the collaboration which represents about 80% of the final statistics.

TABLE 9)

Statistics of the 2 prong V^o Events (Combined Data)

Total No. of Events analysed	No. of fitted Events	No. of NO-FIT Events
1011	791	220

The events classified as NO-FIT events were consistent with more than one unobserved neutral particle.

Ambiguities

About 30% of the fitted events were ambiguous and mostly between two hypotheses. These ambiguities were in addition to the Λ^o/Σ^o ambiguity which cannot be resolved because of the errors present in the measuring techniques employed. The ambiguities were resolved by taking the hypothesis with the highest χ^2 probability. An

exception was made for the two reactions $\pi^+p \rightarrow \pi^+\pi^+K^oA^o$ and $\pi^+p \rightarrow \pi^+K^+A^o\pi^o$ for each of which the number of events was calculated in the following way:

No. of hypotheses	Weight
1	1
2	$\frac{2}{3}$ for the hypothesis with lower χ^2 $\frac{1}{3}$ for the hypothesis with higher χ^2
3	$\frac{1}{3}$ for each hypothesis
4	$\frac{1}{4}$ for each hypothesis

Monte Carlo events generated by Fake for the different final states suggested that about 70% of the ambiguous events were attributed to the right hypothesis by this procedure (Wagini, 1967).

5.3 Cross-sections

The cross-sections for the various final states investigated and the numbers of events upon which the cross-section determinations are based, are listed in Table 10. The numbers of events shown in the table have been corrected for scanning losses from a knowledge of the average scanning efficiencies ~ 95% for 1 V^o and ~ 98% for 2 V^o events. For the determination of the cross-sections the sources of error considered were the uncertainty in the density of liquid hydrogen (c.f. section 3.13) and the uncertainty in the number of events due to the ambiguities present. To account for the unobserved decays in the various channels the following corrections were made:

(i) K^o decays have been weighted by a factor of 3 in order to account for the $\pi^o\pi^o$ and $K_2{}^o$ decay modes.

(ii) To correct for unseen Λ^o, a weighting factor of 3/2 was used because $\frac{2}{3}$ of all Λ^o decay via $\Lambda^o_v \rightarrow p\pi^-$ (v stands for 'visible').

(iii) The cross-section for the reaction $\pi^+p \rightarrow pK^o\bar{K}^o\pi^+$ was determined from the observed number (N_1) of events with two visible K^o decays and the observed number (N_2) of events with one visible K^o decay. The method of calculation was as follows: (the symbols v and i stand for visible and invisible).

$$N(K_{1v}\, K_{1v}) = N_1 \qquad (1)$$

$$N(K_{1v}\, K_{1i}) + N(K_{1v}\, K_2) = N_2 \qquad (2)$$

In a K_1K_1 system the probability for the visible decay of the K_{1v} is $\frac{2}{3}$ and that for the unseen decay of the K_{1i} is $\frac{1}{3}$ so that the number of events in the K_1K_1 channel is given by

$$N(K_1K_1) = 3/2 \cdot\ 3/2 \cdot\ N_1$$

From this the number of $K_{1v}K_{1i}$ events is

$$N(K_{1v}K_{1i}) = 2 \cdot \tfrac{2}{3}\ \tfrac{1}{3}\ N(K_1K_1) = N_1$$

Then from (2)

$$N(K_{1v}K_2) = N_2 - N_1$$

so that

$$N(K_1K_2) = 3/2\ (N_2 - N_1)$$

Furthermore

$$N(K_2K_2) = N(K_1K_1)$$

Thus the total number of events $N(K^O\bar{K}^O)$

is given by

$$N(K^O\bar{K}^O) = N(K_1K_1) + N(K_1K_2) + N(K_2K_2)$$

Hence the cross-section $\sigma(K^O\bar{K}^O)$ is calculated from the relation,

$$\sigma(K^O\bar{K}^O) = 2\sigma(K_1K_1) + \sigma(K_1K_2)$$

where $\sigma(K_1K_1)$ and $\sigma(K_1K_2)$ are calculated as above from N_1 and N_2.

(iv) The cross-section for the $\Lambda^O K^O$ channel was calculated in two different ways:

(a) A weighting factor 3 was used for all events with K_{1v} Λ_i and $K_{1v}\Lambda_v$

(b) Events with $\Lambda_v K_{1i}$ and $\Lambda_v K_{1v}$ were weighted by a factor 3/2.

The cross-section listed in the table is the weighted average of the two values obtained on the basis of (a) and (b).

All events fitting both the Λ^O and Σ^O hypotheses were assigned to the Λ^O channel. Events giving unambiguous Σ^O fits have not been included in the list.

The cross-section for the channel $\pi^+P \rightarrow P\pi^+K^+K^-$ has been estimated on the basis of the 309 events which gave an unambiguous 4C fit to the above channel in a sample of 24000 four prong events.

Thirty-seven events which were ambiguous between the above channel and the $P\pi^+\pi^+\pi^-$ channel (6004 events) were not included.

TABLE 10

Cross-Sections of Strange Particle Productions

(Corrected for unobserved decay modes)

Reaction	This Experiment (5 GeV/c)		Other Experiments Cross-sections (μb)	
	Number of Events	Cross-section μb	(*) 4 GeV/c	(**) 8 GeV/c
$\pi^+ p \rightarrow$				
(1) $(\Lambda^o/\Sigma^o)K^+\pi^+$	95	66±7	81±11	33±7
(2) $(\Lambda^o/\Sigma^o)K^+\pi^+\pi^o$	185	130±9	148±16	76±12
(3) $(\Lambda^o/\Sigma^o)K^o\pi^+\pi^+$	158	82±8	91±10	76±11
(4) $pK^+\bar{K}^o$	37	53±8	43±11	34±8
(5) $pK^+\bar{K}^o\pi^o$	89	105±11	59±14	69±17
(6) $pK^o\bar{K}^o\pi^+$	99	78±12	87±14	88±16
$pK_1^oK_1^o\pi^+$		28±5		
$pK_1^oK_2^o\pi^+$		22±7		
(7) $nK^+\bar{K}^o\pi^+$	71	86±10	80±16	63±18
(8) $pK^+K^-\pi^+$	309	109±27		

(*) Aachen-Hamburg-London-Munchen collaboration: N.C. 43,1010 (1966)

(**) CERN-CRACOW-WARSAW Collaboration : Phys. Letts. 22, 109 (1966)

The amount of 0.6% of such an ambiguity is in good agreement with the percentage predicted by Fake calculations.

Again, Fake calculations suggested that about 1% of the Monte Carlo events of the type $\pi^+p \rightarrow p\pi^+\pi^+\pi^-\pi^0$ give spurious fits to the $p\pi^+K^+K^-$ channel. So, in the sample of about 6300 $p\pi^+\pi^+\pi^-\pi^0$ events in the present analysis one would expect 63 events giving rise to the spurious fit. Since in the analysis 4C fits were chosen in preference to 1C fits, a contamination ~ 20% is estimated in the sample of the selected $p\pi^+K^+K^-$ events. The cross-section has been corrected for this contamination.

5.4 Estimation of Resonances

To look for the production of resonances in the various ΛK and $K\bar{K}$ channels, the two particle effective mass distributions for the various final states are given. The cross-sections for the various resonances have been determined by counting the excess of events in the peak regions over an estimated smooth background. Monte Carlo events for the various final states were generated by FOWL (c.f. section 3.14) to obtain the phase space predictions for the various mass distributions. The smooth curve in each of the plots is the phase space distribution normalised to the experimental histogram outside the peak regions. In the analysis the following mass limited for the Y*(1385) and K*(890) have been used:

FIG. 49 DISTRIBUTION OF $M(\Lambda\pi^+)$

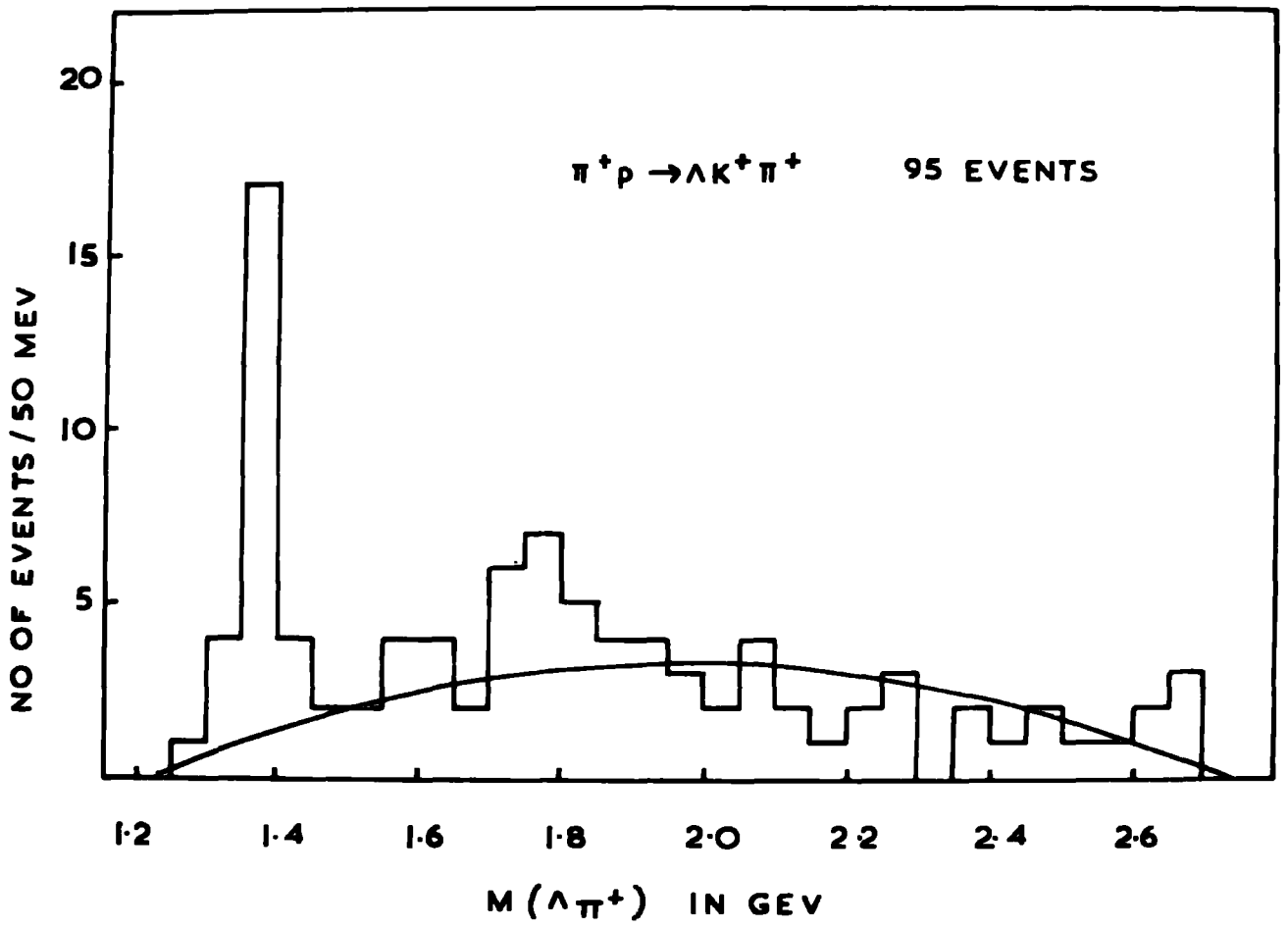

FIG. 50

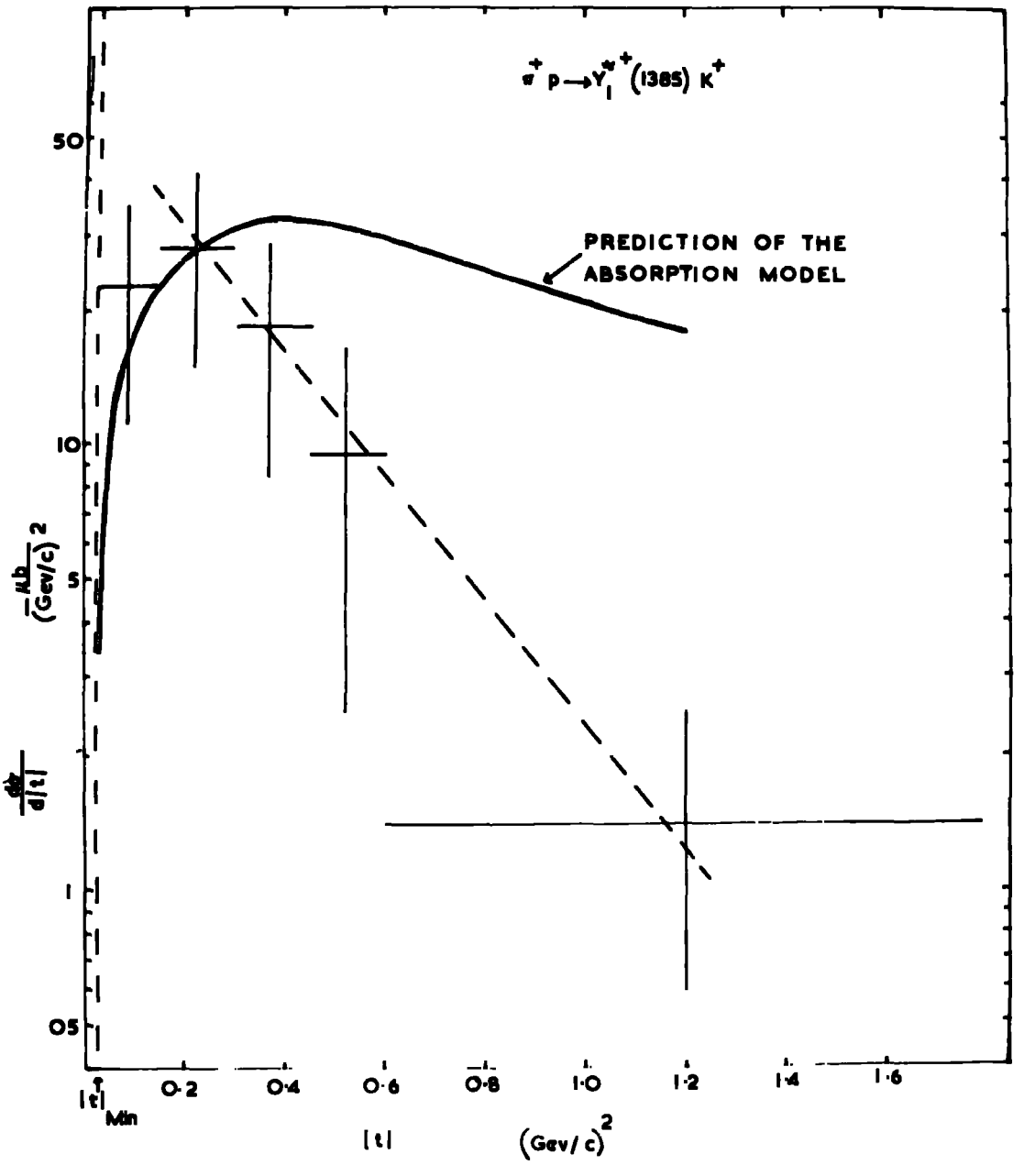
$\pi^+ p \rightarrow Y_1^{*+}(1385)\, K^+$
PREDICTION OF THE ABSORPTION MODEL
50
10
5
1
05
$\frac{d\sigma}{d|t|}$ $\frac{\mu b}{(Gev/c)^2}$
$|t|_{Min}$
0·2
0·4
0·6
0·8
1·0
1·2
1·4
1·6
$|t|$
$(Gev/c)^2$

FIG. 51

FEYNMAN DIAGRAMS

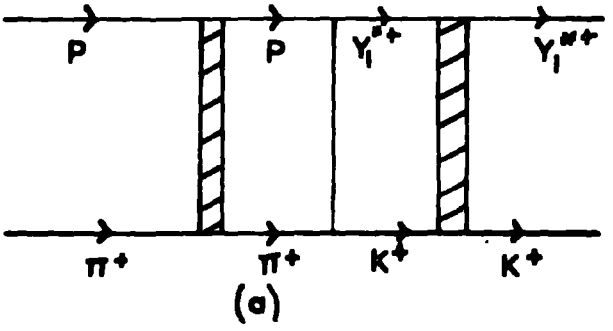

(a)

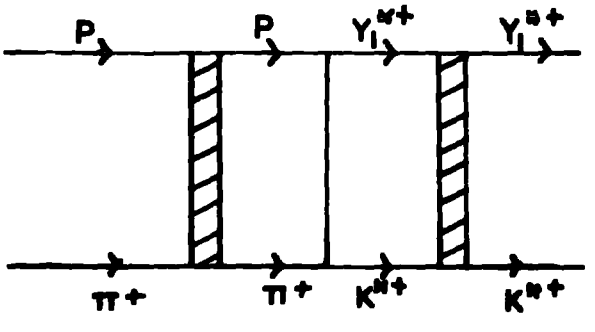

(b)

Y*	:	1325 to 1450 MeV
K*	:	825 to 950 MeV

5.5 Resonance Production in the ΛK channels

(i) The reaction $\pi^+P \rightarrow \Lambda^o K^+ \pi^+$

In this reaction a strong production of $Y_1^{*+}(1385)$ is observed in the $\Lambda^o\pi^+$ effective mass distribution which is shown in figure 49. The small enhancement centering at about 1760 MeV may be due to the $Y_1^{*+}(1765)$. An estimatedexcess of events over the background indicates that (20 ± 2)% of the reaction proceeds via the quasi two-body state

$$(a) \quad \pi^+P \rightarrow Y_1^{*+}(1385)\ K^+$$

The $\frac{d\sigma}{dt}$ distribution for the reaction (a) is shown in figure 50.

Recently, Eysel et al (1967), absorption model calculations have been made for a number of quasi two-body states (see Feymann diagrams in figure 51) in which the effect of the finite width of the resonances has been included by multiplying the stable mass cross-sections by the appropriate Breit-Wigner distribution of the mass of the resonance. The results obtained for the reaction above in which K* exchange is assumed are reproduced in figure 50.

It is seen that the experimental distribution is peaked much more strongly towards lower $|t|$ values than is predicted by the absorption model calculation. The influence of the absorptive effects introduced by the authors is less drastic than is suggested by the experimental

distribution. This behaviour of the absorption model in its present form has been shown to be present in other cases for which a vector meson exchange has been assumed.

The experimental distribution in figure 50 can be fitted by a simple exponential of the form $e^{-a|t|}$ for values of $|t| > 0.2$ (Gev/c)^2 where a is found to be 3.2 (Gev/c)$^{-2}$. This is shown by the dotted line.

(ii) The reactions:

(a) $\pi^+ P \rightarrow \Lambda^o K^o \pi^+ \pi^+$

(b) $\pi^+ P \rightarrow \Lambda^o K^+ \pi^+ \pi^o$

Both the reactions (a) and (b) are dominated by strong production of $Y_1^{*+}(1385)$ and $K^{*+}(890)$, and so they are discussed together. Figure 52(a) shows the triangular mass plots, $M(\Lambda^o\pi^+)$ versus $M(K^o\pi^+)$, with two points per event, for the reaction (a). Figure 52(b) shows the triangular mass plots $M(\Lambda^o\pi^+)$ versus $M(K^+\pi^o)$ for the reaction (b). The projections of the $(\Lambda^o\pi^+)$ mass on the corresponding mass axes for the two reactions are shown in figure 53(a) and figure 53(b) respectively. The projections of the $(K^o\pi^+)$ mass and the $(K^+\pi^o)$ mass for the two reactions are shown in figure 54(a) and figure 54(b).

As can be seen from the figures $Y_1^{*+}(1385)$ is produced at about equal rates in the two reactions. The cross-sections for the production of this resonance were determined to be $(26 \pm 4)\mu b$ in the reaction (a) and $(33 \pm 5)\mu b$ in the reaction (b).

FIG. 52

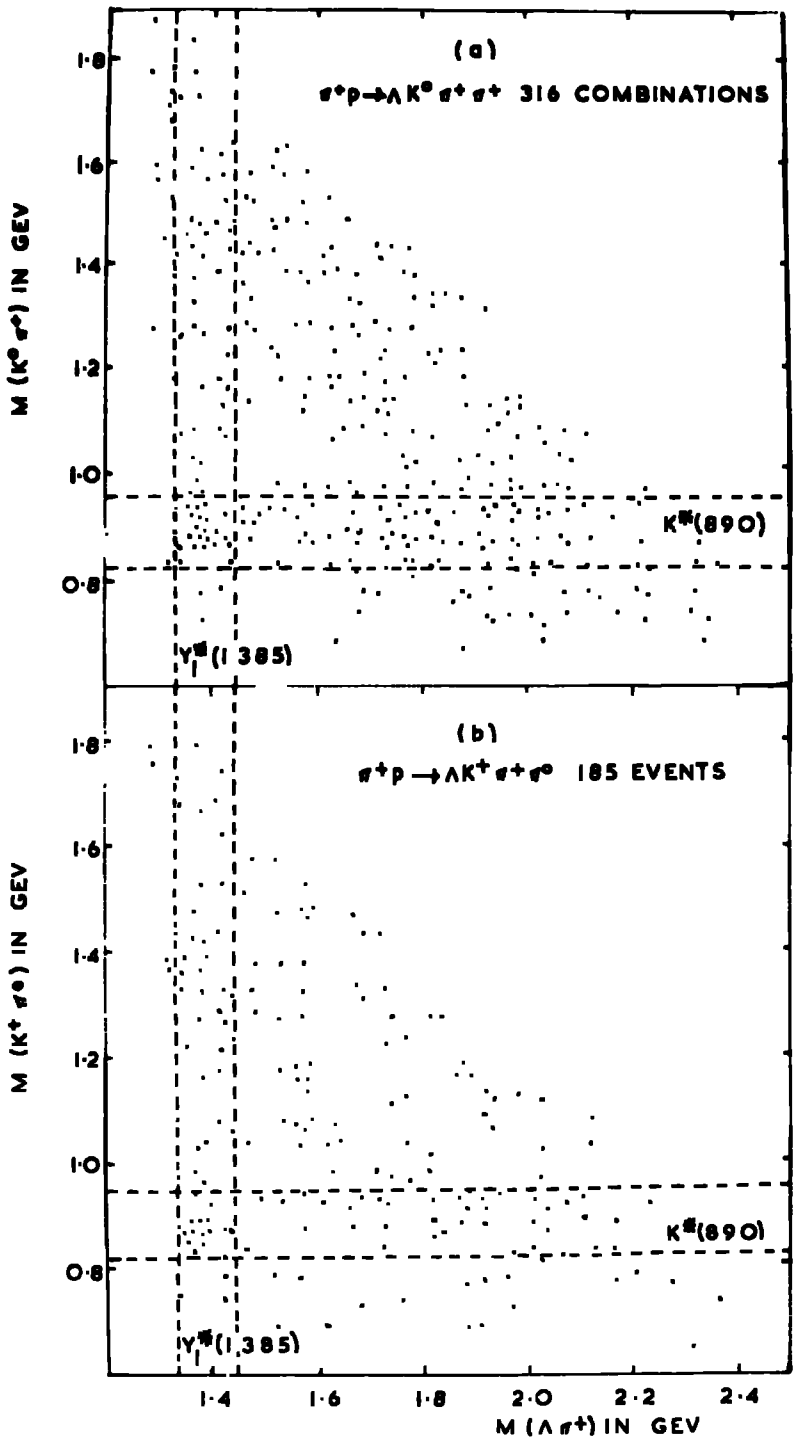
(a)
$\pi^+p \rightarrow \Lambda K^0 \pi^+ \pi^+$ 316 COMBINATIONS
M ($K^0 \pi^+$) IN GEV
1·8
1·6
1·4
1·2
1·0
0·8
$K^*(890)$
$Y_1^*(1385)$
(b)
$\pi^+p \rightarrow \Lambda K^+ \pi^+ \pi^0$ 185 EVENTS
M ($K^+ \pi^0$) IN GEV
1·8
1·6
1·4
1·2
1·0
0·8
$K^*(890)$
$Y_1^*(1385)$
1·4
1·6
1·8
2·0
2·2
2·4
M ($\Lambda \pi^+$) IN GEV

FIG. 53

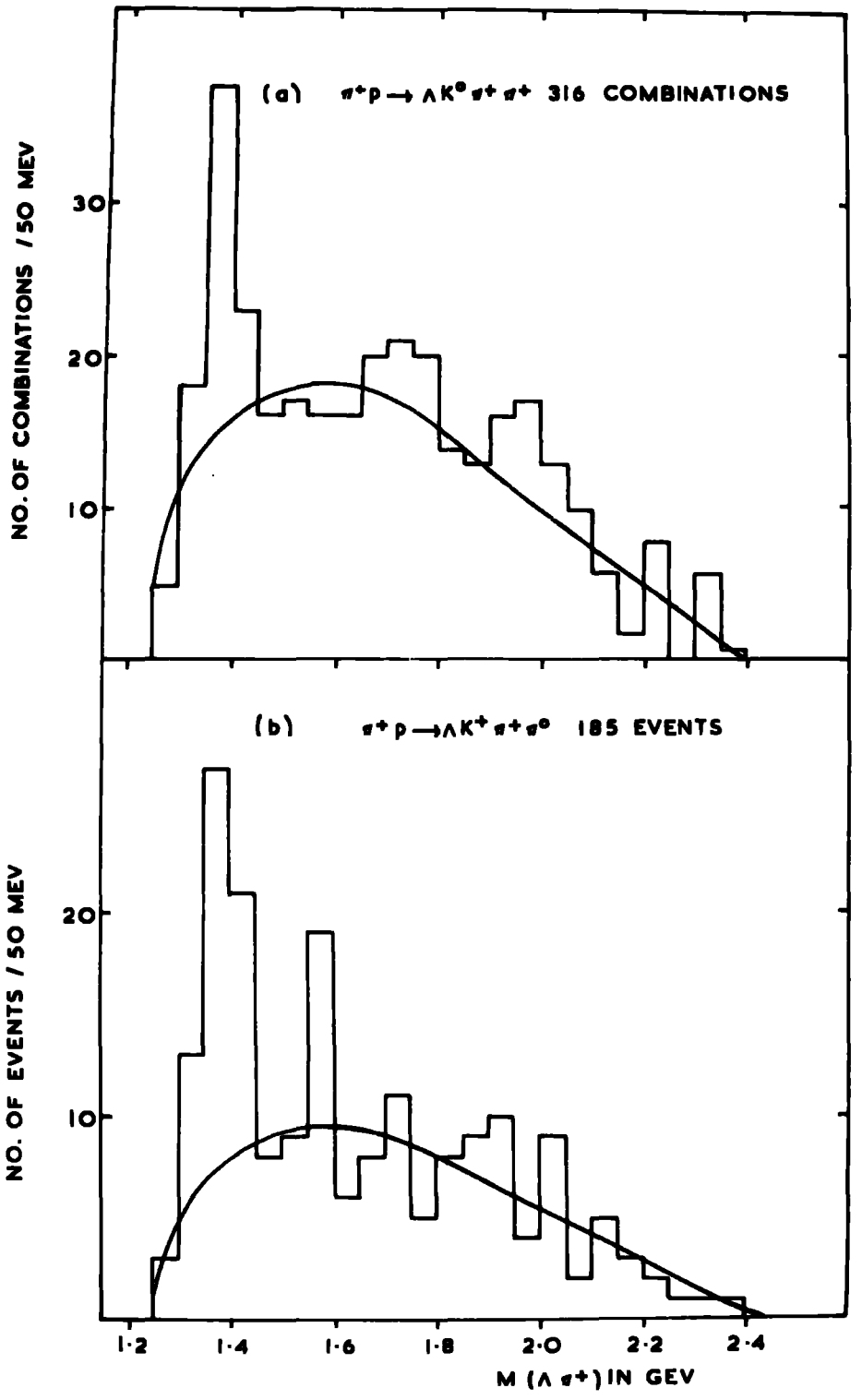
(a) $\pi^+ p \rightarrow \Lambda K^0 \pi^+ \pi^+$ 316 COMBINATIONS
NO. OF COMBINATIONS / 50 MEV
30
20
10
(b) $\pi^+ p \rightarrow \Lambda K^+ \pi^+ \pi^0$ 185 EVENTS
NO. OF EVENTS / 50 MEV
20
10
1·2
1·4
1·6
1·8
2·0
2·2
2·4
M ($\Lambda \pi^+$) IN GEV

FIG. 54

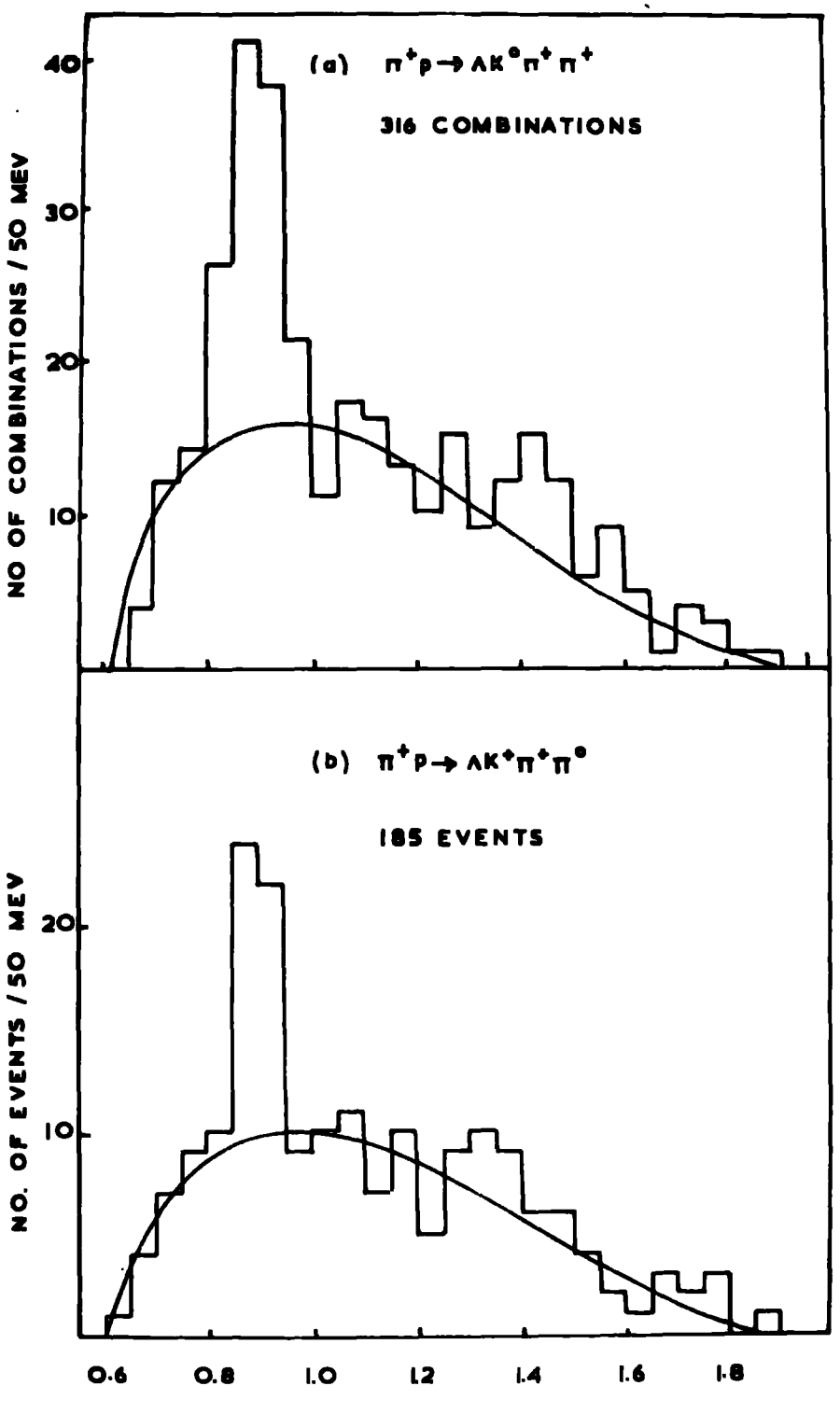
(a) $\pi^+p \rightarrow \Lambda K^0\pi^+\pi^+$
316 COMBINATIONS
NO OF COMBINATIONS / 50 MEV
40
30
20
10
(b) $\pi^+p \rightarrow \Lambda K^+\pi^+\pi^0$
185 EVENTS
NO. OF EVENTS / 50 MEV
20
10
0.6
0.8
1.0
1.2
1.4
1.6
1.8
$M(K\pi)^+$ GEV

The $K^{*+}(890)$ is seen to be produced more strongly in the reaction (a) than in the reaction (b). From isospin considerations one would expect that the $K^{*+}(I, I_3 = \frac{1}{2}, +\frac{1}{2})$ decaying into $\pi^+(I_3=+1)$ $K^o(I_3=-\frac{1}{2})$ mode will be produced at twice the rate of K^{*+} decaying into the $\pi^o(I_3=0)$ $K^+(I_3=\frac{1}{2})$ mode. The partial cross-sections of the $K^{*+}(890)$ in the two reactions were determined to be

$$\sigma\ (K^{*+} \rightarrow \pi^+K^o) = (44 \pm 5)\mu b$$

$$\sigma\ (K^{*+} \rightarrow \pi^oK^+) = (25 \pm 6)\mu b$$

These determinations are in good agreement with the ratio 2 expected from the isospin considerations above. The total cross-section for the reaction $\pi^+P \rightarrow \Lambda^o\pi^+K^{*+}$ is estimated to be $(69\pm8)\mu b$.

(iii) Quasi two-body production

In the two dimensional mass plots of the two channels

$$\pi^+P \rightarrow \Lambda^oK^o\pi^+\pi^+ \text{ and } \pi^+P \rightarrow \Lambda^oK^+\pi^+\pi^o$$

(Figure 52) an accumulation of events is observed in the region in which the bands of $K^{*+}(890)$ and $Y_1^{*+}(1385)$ overlap, giving the evidence for the quasi two-body reaction

$$\pi^+P \rightarrow Y_1^{*+}(1385)\ K^{*+}(890)$$

in both channels. To show this more clearly in a larger sample, the two channels have been taken together and a selection of events has been made under the restriction that one combination of the $(\Lambda^o\pi^+)$ mass lies in the $Y_1^{*+}(1385)$ band defined as $1330 < M(\Lambda^o\pi^+) < 1440$ MeV. In the combined sample of the two channels 114 events satisfy this restriction. The $(K\pi)^+$ mass distribution for these 114

FIG. 55

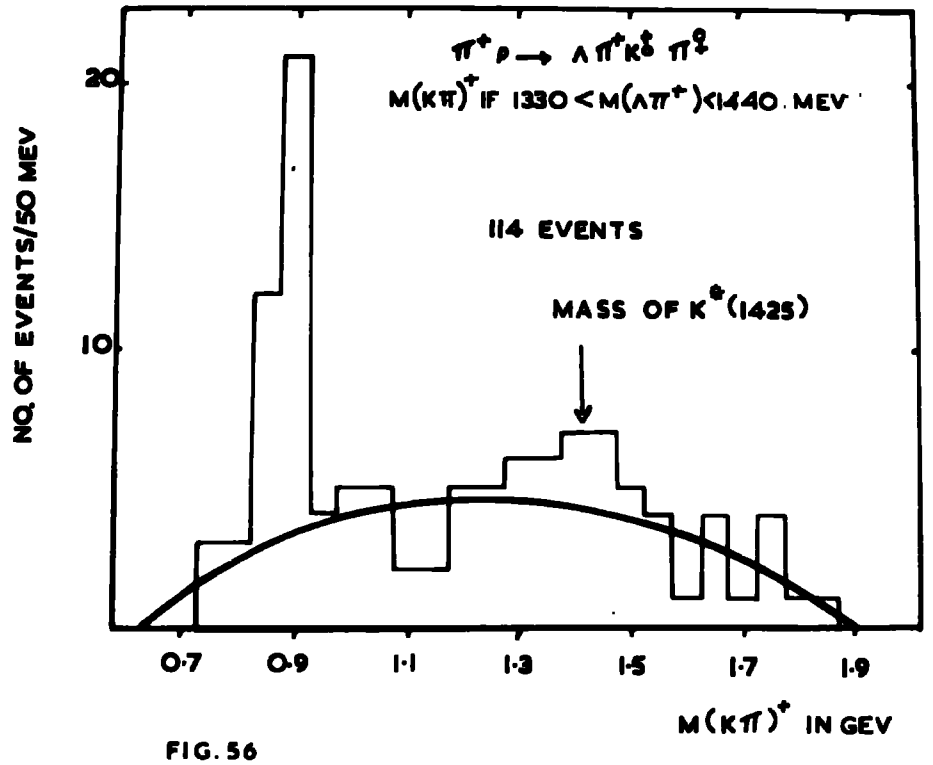
$\pi^+ p \rightarrow \Lambda \pi^+ K^0_S \pi^0_S$
$M(K\pi)^+$ IF $1330 < M(\Lambda\pi^+) < 1440$ MEV
114 EVENTS
MASS OF $K^*(1425)$
NO. OF EVENTS/50 MEV
20
10
0·7
0·9
1·1
1·3
1·5
1·7
1·9
$M(K\pi)^+$ IN GEV

FIG. 56

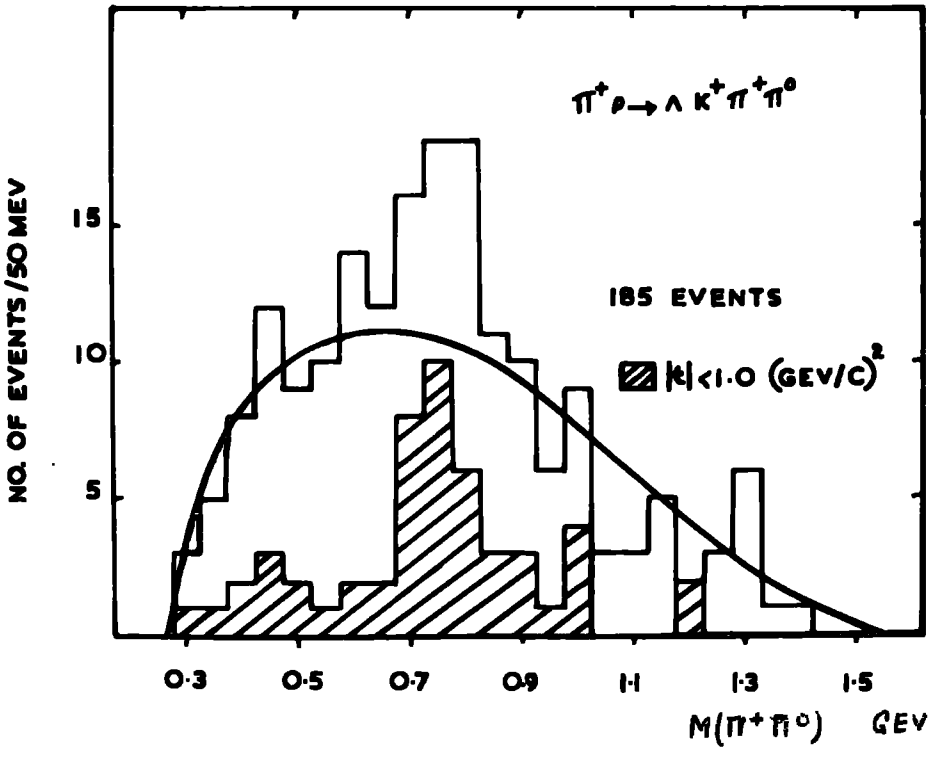
$\pi^+ p \rightarrow \Lambda K^+ \pi^+ \pi^0$
185 EVENTS
$|t| < 1.0$ (GEV/C)^2
NO. OF EVENTS/50 MEV
15
10
5
0·3
0·5
0·7
0·9
1·1
1·3
1·5
$M(\pi^+ \pi^0)$ GEV

events is shown in figure 55. The $K^{*+}(890)$ is seen in this plot with little background. From this plot the number of events contributing to the double resonance production is estimated to be 33±4 and the corresponding cross-section is estimated to be (21±6). Besides the $K^{*+}(890)$ peak a small enhancement is observed which centres at about 1425 MeV. This could be due to the presence of the $K^{*}(1420)$ if not due to some kinematic effect imposed by the restriction.

Application of the Absorption Model

As in the case of the reaction $\pi^+p \rightarrow Y_1^{*+}(1385)\ K^+$ discussed in section 5.5(i) it is of interest to compare the predictions of the absorption model calculated by Eysel et al (1967) with the experimental $\frac{d\sigma}{dt}$ distribution of the reaction $\pi^+p \rightarrow Y_1^{*+}(1385)$ $K^{*+}(890)$. The lowest mass that can be exchanged in this reaction is a K meson. The experimental values of $\frac{d\sigma}{dt}$ for this reaction has been calculated under the assumption that the background can be neglected. The experimental distribution is shown in figure 57. The smooth curve represents the predictions of the absorption model as calculated by the authors. The shape of the curve is in good agreement with the experimental distribution. However, it is necessary to scale down the calculated values of $\frac{d\sigma}{dt}$ by factor ~ 8.0 before the calculations and the observations can be brought into agreement. This, as stated by the authors may be due to uncertainties in the value of the coupling constant for the PKY_1^* vertex which is

8 JUL 1968

FIG. 57

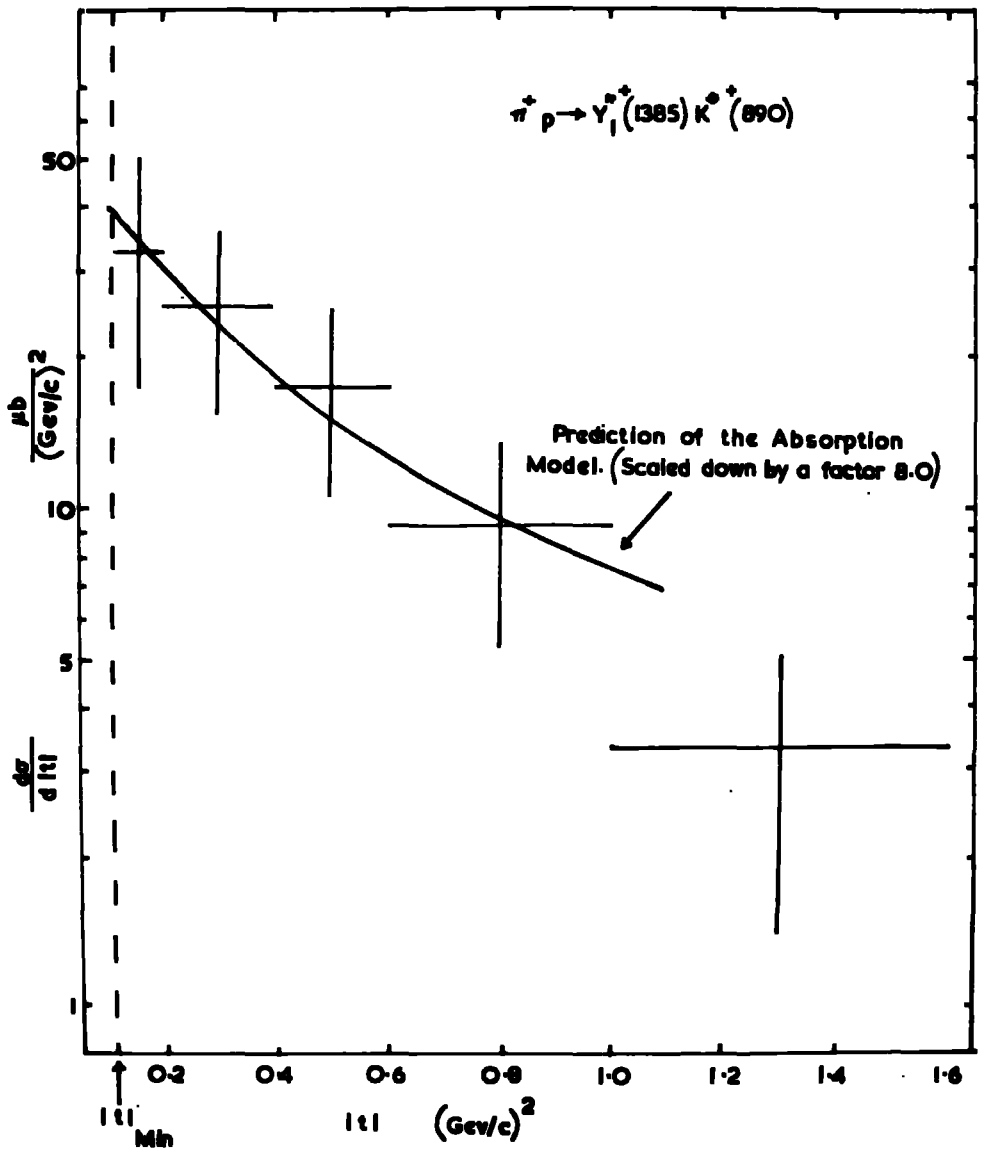
$\pi^+ p \rightarrow Y_1^{*+}(1385)\, K^{*+}(890)$
Prediction of the Absorption Model. (Scaled down by a factor 8.0)
$\frac{d\sigma}{d|t|}$
$\frac{\mu b}{(Gev/c)^2}$
50
10
5
1
0·2
0·4
0·6
0·8
1·0
1·2
1·4
1·6
$|t|_{Min}$
$|t|$ $(Gev/c)^2$

used in the calculation.

In the 8 GeV/c π^+P experiment, the t-dependence of the same reaction has been found to be in better agreement with the predicted values, the scale factor needed being about 2.5 (Eysel et al, 1967). It is thus evident that the discrepancy between the predicted and the experimental values is energy dependent.

The experimental distribution in figure 57 can be fitted by the exponential $\frac{d\sigma}{dt} = \text{Const.}\ e^{-a|t|}$ and a value, $a = 2.0\left(\frac{\text{GeV}}{c}\right)^{-2}$ is obtained.

The production of ρ^+

The $(\pi^+\pi^o)$ effective mass distribution for the reaction $\pi^+P \rightarrow \Lambda^o K^+\pi^+\pi^o$ is shown in figure 56. The ρ^+ meson is seen to be produced. The shaded histogram is the distribution for events in which the square of the four-momentum transfer to the $(\pi^+\pi^o)$ combination is less than 1.0 $(\text{Gev}/c)^2$. The ρ^+ is seen to be more pronounced which indicates peripheral production.

No other resonance is observed in this channel or in the $\Lambda^o K^o \pi^+\pi^+$ channel. The K(730) which has been reported in the reaction $\pi^+P \rightarrow \Lambda^o K^o \pi^+\pi^+$ at 3.2 GeV/c by Cason et al (1966) is not observed in the ΛK channel in this analysis.

Table 11 gives the cross-sections of resonance production in the various ΛK channels discussed above.

TABLE 11

Cross-sections of Resonance Production in ΛK channels

Channel	Reaction	Cross-section (μb)
$\Lambda^o K^+ \pi^+$	$\pi^+ P \rightarrow Y_1^{*+}(1385)\ K^+$ $\quad\quad\quad\quad\quad\quad \lfloor\!\rightarrow \Lambda^o \pi^+$	14 ± 4
$\Lambda^o K^+ \pi^+ \pi^o$	$\pi^+ P \rightarrow Y_1^{*+}\ K^+ \pi^o$ $\quad\quad\quad\quad\quad\quad \lfloor\!\rightarrow \Lambda^o \pi^+$	33 ± 5
	$\pi^+ P \rightarrow \Lambda^o \pi^+ K^{*+}(890)$ $\quad\quad\quad\quad\quad\quad \lfloor\!\rightarrow K^+ \pi^o$	25 ± 6
	$\pi^+ P \rightarrow \Lambda^o K^+ \rho^+$ $\quad\quad\quad\quad\quad\quad\quad\quad \lfloor\!\rightarrow \pi^+ \pi^o$	13 ± 4
$\Lambda^o K^o \pi^+ \pi^+$	$\pi^+ P \rightarrow Y_1^{*+}(1385)\ K^o \pi^+$	26 ± 4
	$\pi^+ P \rightarrow \Lambda^o \pi^+ K^{*+}(890)$ $\quad\quad\quad\quad\quad\quad\quad\quad \lfloor\!\rightarrow K^o \pi^+$	44 ± 5
$\Lambda^o K^+ \pi^+ \pi^o$ $\Lambda^o K^o \pi^+ \pi^+$	$\pi^+ P \rightarrow Y_1^{*+}(1385) K^{*+}(890)$	21 ± 6

5.6 Resonance production in the $K\bar{K}$ channels

The resonances observed in the various channels discussed in this section are the $N^{*++}(1236)$, $K^{*}(890)$ and the A_2^{+}. Evidence is also found for the $Y^{*}_{o}(1520)$, $\Phi(1019)$ and $\kappa(730)$.

(i) The reaction $\pi^{+}p \rightarrow pK^{+}\bar{K}^{o}$

The $K^{+}\bar{K}^{o}$ effective mass distribution for this reaction is shown in figure 58. A broad enhancement centering at about the A_2 mass (1310 MeV) is observed. The shaded histogram is drawn for events in which the squared four-momentum transfer to the $K^{+}\bar{K}^{o}$ combination, $|t| < 1.0\ (GeV/c)^2$. The enhancement has been interpreted as the $K\bar{K}$ decay mode of the A_2. An estimated excess of events above the smooth background drawn in the figure gives 8 ± 4 events. This leads to a cross-section of $\sigma(A_2^{+} \rightarrow K^{+}\bar{K}^{o})$ of $(11\pm6)\mu b$. This result has been used to calculate the branching ratio

$$\frac{A_2 \rightarrow K\bar{K}}{A_2 \rightarrow \rho\pi} = (9 \pm 4)\%$$

(c.f. section 4.31).

(ii) The reactions

(a) $\pi^{+}p \rightarrow p\pi^{+}K^{+}K^{-}$

(b) $\pi^{+}p \rightarrow p\pi^{+}K^{o}\bar{K}^{o}$

The prominent features of the two reactions are the production of $N^{*++}(1236)$ and $K^{*}(890)$. Both of them are produced preferentially at low momentum transfer. The $N^{*++}(1236)$ is produced more strongly in (a) than in (b). The two other reactions of the above type namely,

FIG. 58

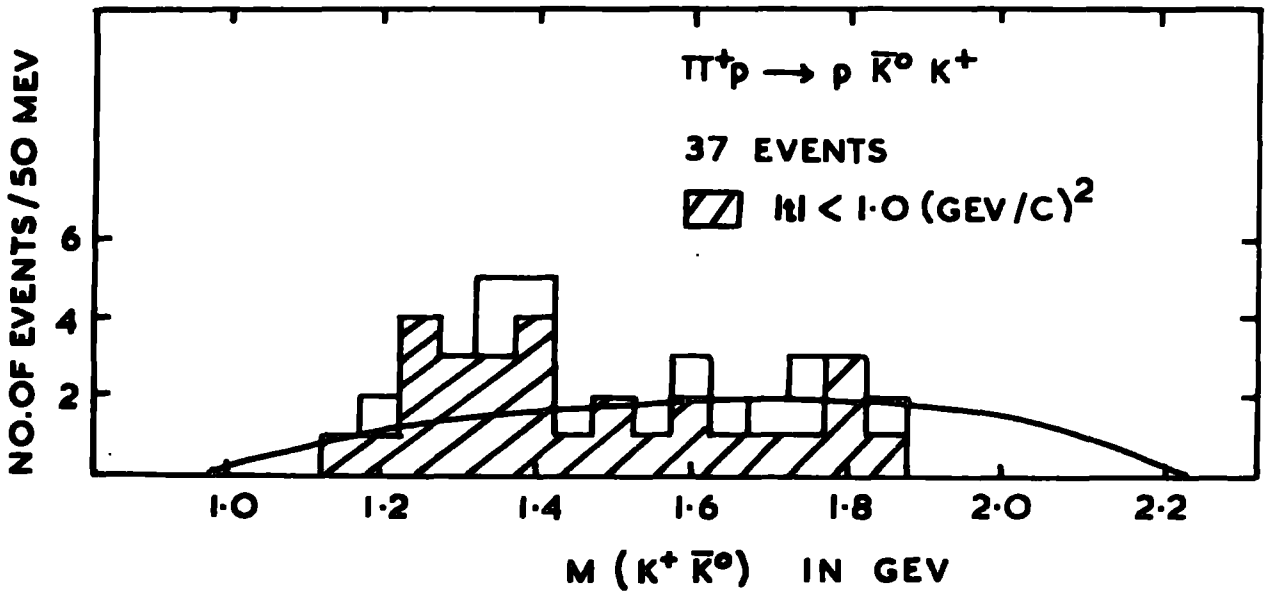
$\pi^+ p \rightarrow p\ \bar{K}^0\ K^+$
37 EVENTS
$|t| < 1.0\ (GEV/c)^2$
NO. OF EVENTS / 50 MEV
2
4
6
1·0
1·2
1·4
1·6
1·8
2·0
2·2
M ($K^+ \bar{K}^0$) IN GEV

FIG. 59

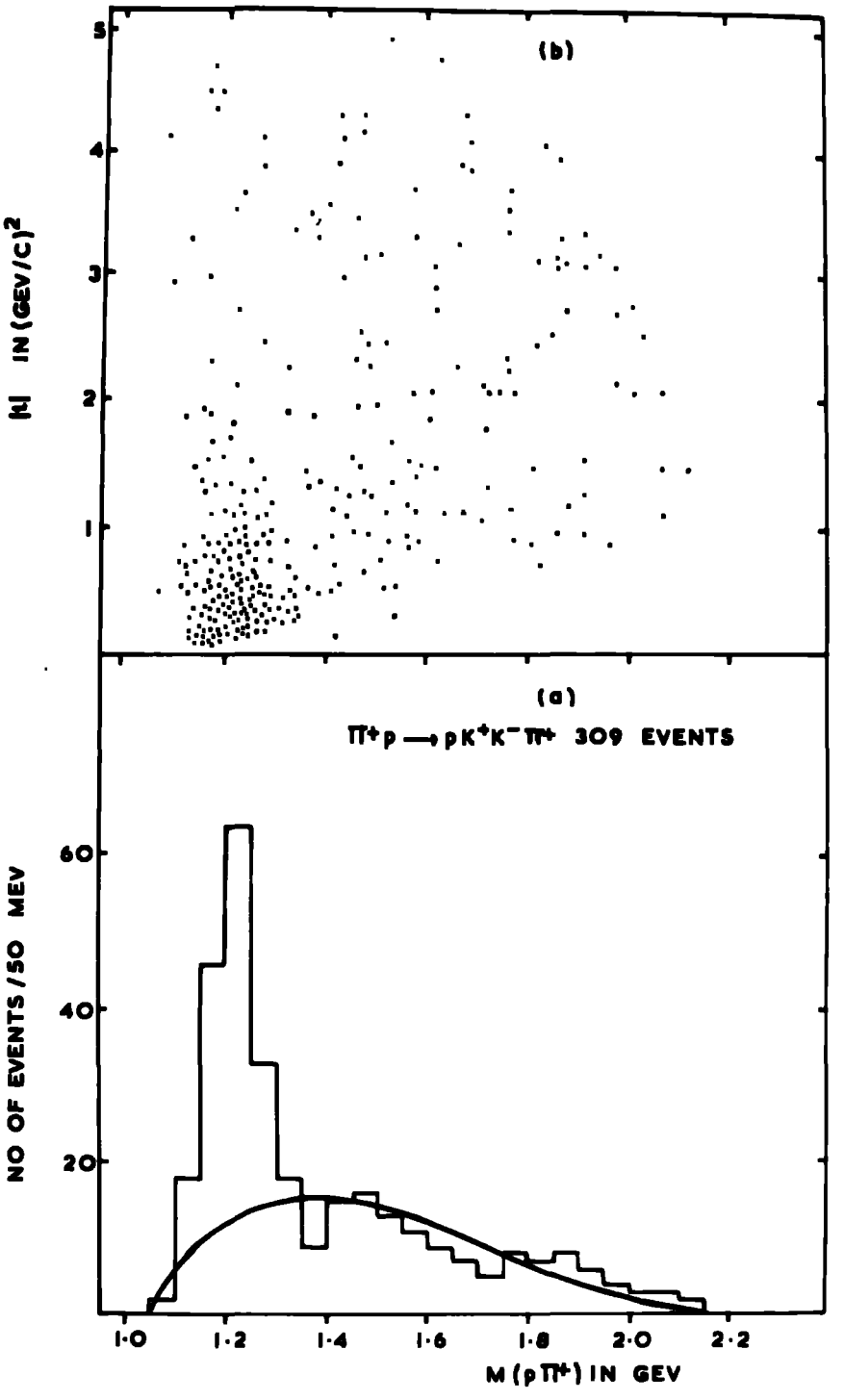
(b)
|t| IN (GEV/C)²
5
4
3
2
1
(a)
π⁺p → pK⁺K⁻π⁺ 309 EVENTS
NO OF EVENTS/50 MEV
60
40
20
1·0
1·2
1·4
1·6
1·8
2·0
2·2
M(pπ⁺) IN GEV

$$\pi^+p \rightarrow pK^+\bar{K}^o\pi^o \quad \text{and} \quad \pi^+p \rightarrow n\pi^+K^+\bar{K}^o$$

do not show any significant resonance production.

Figure 59(a) shows the $p\pi^+$ effective mass distribution for the reaction (a) and the corresponding Chew-Low plot is shown in figure 59(b). The $N^{*++}(1236)$ shows strongly and particularly at $|t| < 1.0$ $(GeV/c)^2$. The $K^-\pi^+$ effective mass distribution and the corresponding Chew-Low plot for this reaction are shown in figure 60(a) and figure 60(b). The shaded area in the $K^-\pi^+$ mass distribution corresponds to events for which the π^+ does not form a $p\pi^+$ effective mass in the N^{*++} band which is defined as $1120 < M(p\pi^+) < 1320$ MeV. The $K^{*o}(890)$ is more significantly observed in the shaded histogram. The Chew-Low plot shows that it is produced preferentially at low $|t|$ values.

For the reaction (b) the $p\pi^+$ effective mass distribution and the corresponding Chew-Low plot are shown in figure 61(a) and figure 61(b). The $N^{*++}(1236)$ is seen to be produced predominantly at low momentum transfer in this reaction. The $K^o\pi^+$ effective mass distribution and the corresponding Chew-Low plot for this channel are shown in figure 62(a) and figure 62(b). The shaded part of the histogram corresponds to events for which the $p\pi^+$ effective mass does not lie in the N^* band defined above. The $K^{*+}(890)$ observed here is also seen to be produced preferentially at small momentum transfer.

FIG. 60

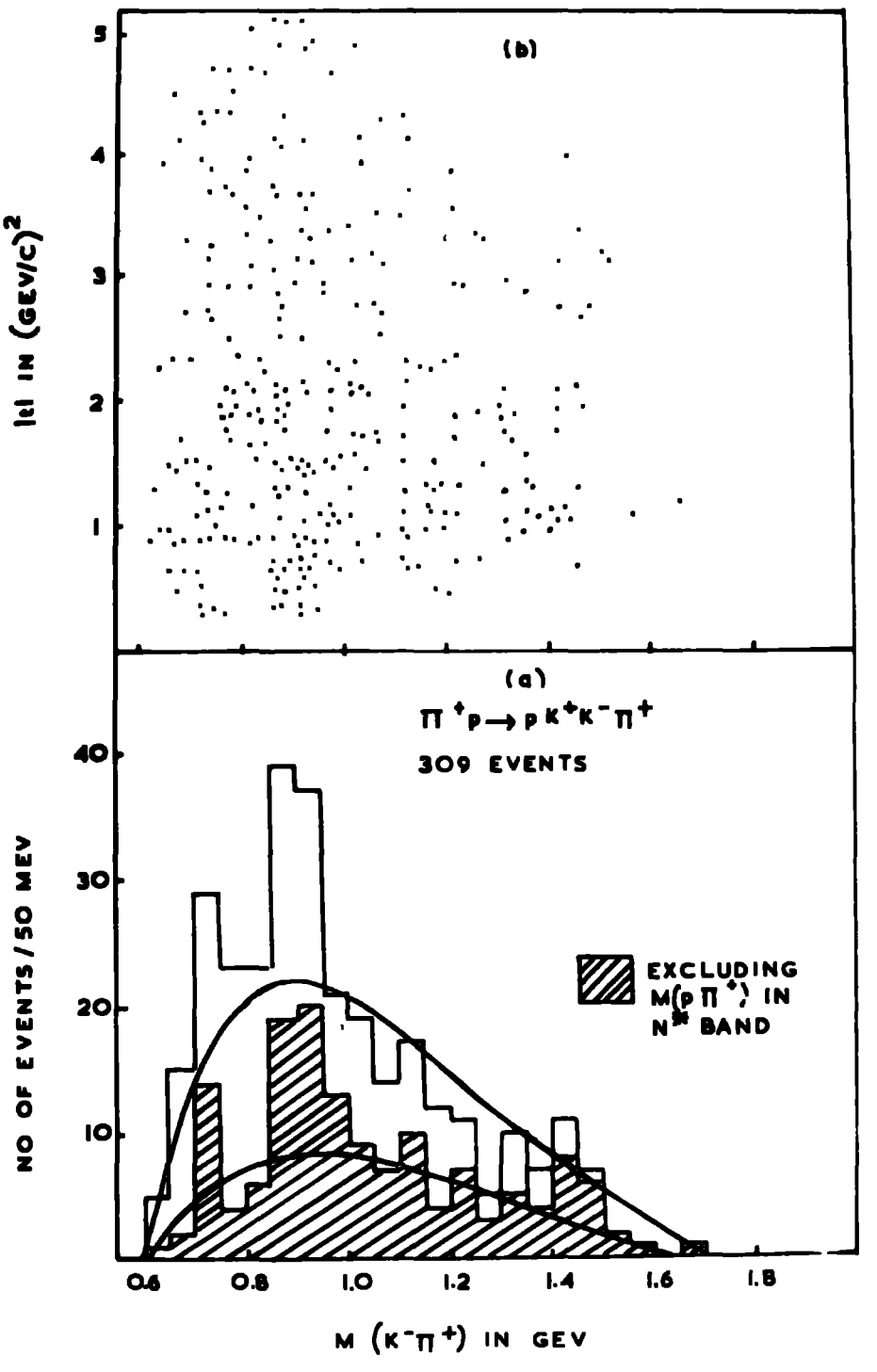
(b)
|t| IN (GEV/c)²
5
4
3
2
1
(a)
π⁺p → pK⁺K⁻π⁺
309 EVENTS
EXCLUDING M(pπ⁺) IN N* BAND
NO OF EVENTS/50 MEV
40
30
20
10
0.6
0.8
1.0
1.2
1.4
1.6
1.8
M (K⁻π⁺) IN GEV

FIG. 61

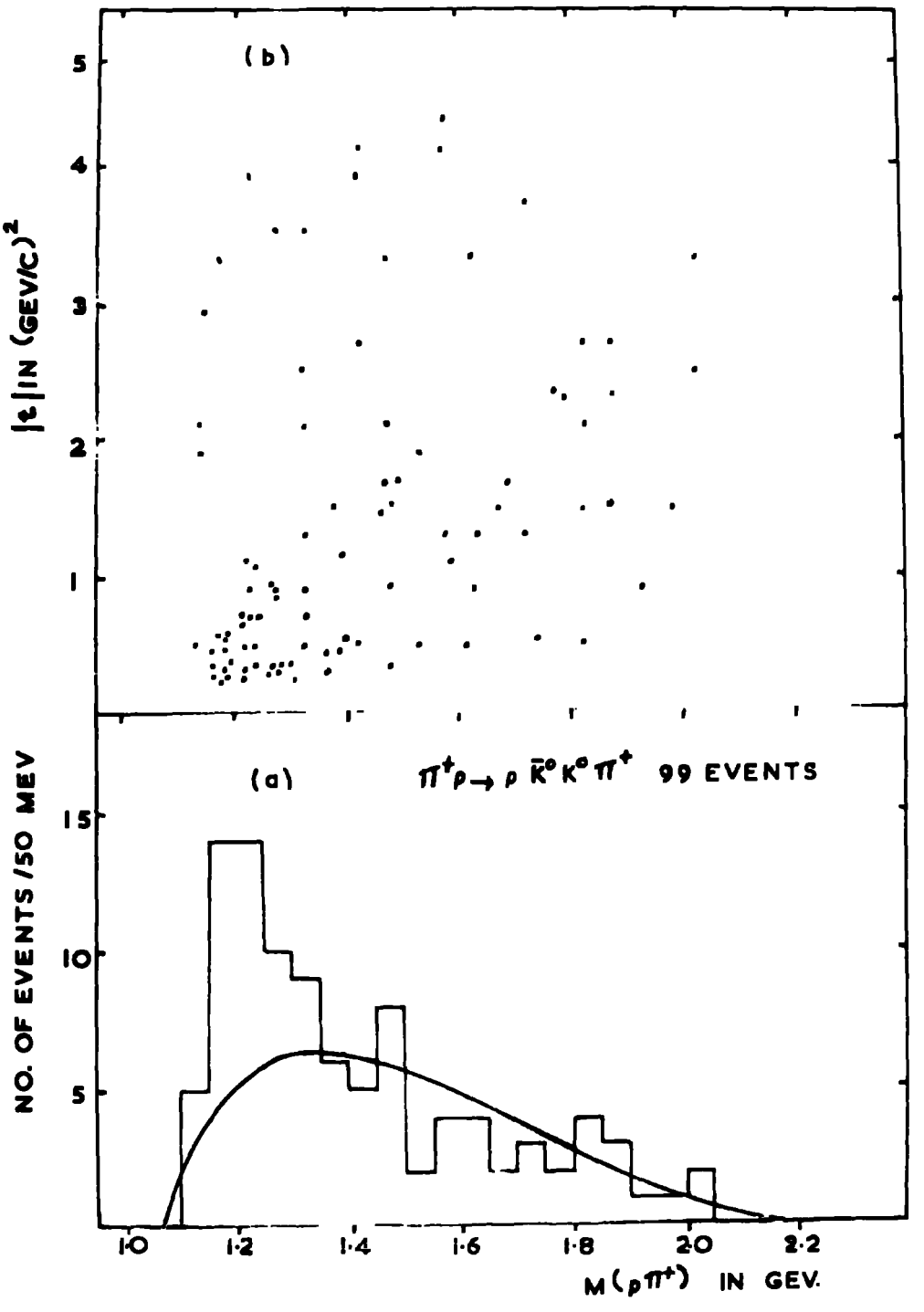
(b)
$|t|$ IN (GEV/C)^2
5
4
3
2
1
(a)
$\pi^+ p \rightarrow p\ \bar{K}^0 K^0 \pi^+$ 99 EVENTS
NO. OF EVENTS /50 MEV
15
10
5
1·0
1·2
1·4
1·6
1·8
2·0
2·2
M($p\pi^+$) IN GEV.

The smooth curves drawn in all the mass distributions are the statistical phase space predictions normalised to the smooth background outside the peak regions. The cross-sections for the $N^{*++}(1236)$ and the $K^{*}(890)$ in both the reactions (a) and (b) have been estimated by counting the number of events above the calculated background. The values of the cross-sections are given in Table 12.

(iii) The κ(730)

An enhancement known as the Kappa in the KΠ effective mass at about 730 MeV has been reported in a number of experiments; the recent ones are the $\Pi^{+}P$ experiments at 8 GeV/c (Brandt et al, 1966) and at 3.2 GeV/c (Cason et al, 1966).

The nature of the Kappa enhancement is not yet clear. It is not certain whether the Kappa is a resonance which is produced in an energy-dependent production mechanism or whether an energy dependent Kinematic effect is responsible for the Kappa peak. This is because, although the Kappa appears at about the same mass and width in many reactions, it does not appear in many of the same reactions at somewhat different energies.

In the present experiment, the evidence for the Kappa is shown in the $K^{-}\Pi^{+}$ effective mass distribution (figure 60(a)) of the channel $\Pi^{+}P \rightarrow P\Pi^{+}K^{+}K^{-}$. A narrow peak at the position of the κ(730) is observed which becomes even more pronounced after removing the N^{*++} events (shaded histogram). No evidence for the Kappa is seen in the $PK^{o}\bar{K}^{o}\Pi^{+}$ channel (figure 62(a)) and this is in agreement with the result reported at 8 GeV/c $\Pi^{+}P$ experiment (Brandt et al, 1966).

FIG. 62

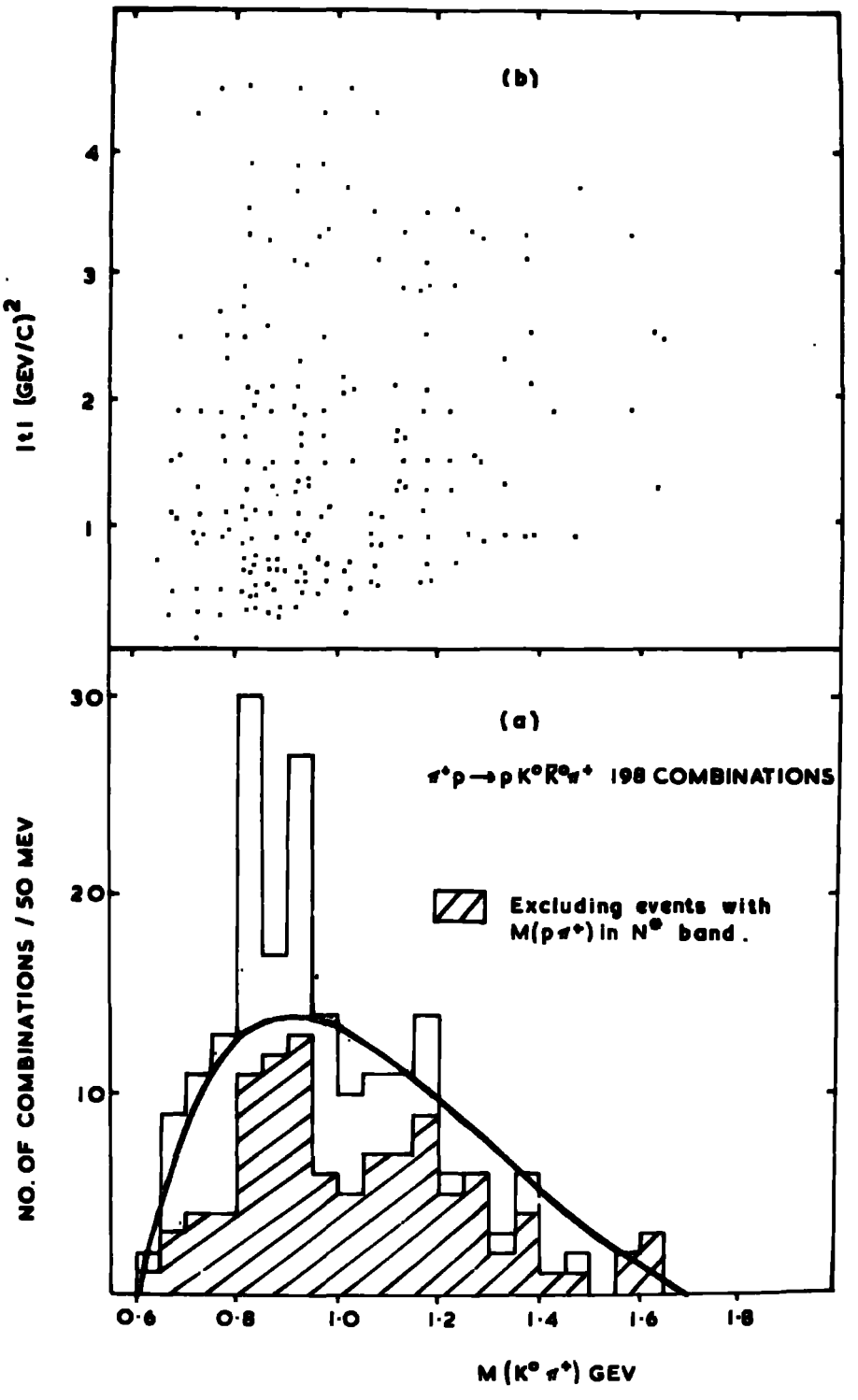
(b)
4
3
2
1
|t| (GEV/C)²
(a)
π⁺p → p K⁰ K⁰ π⁺ 198 COMBINATIONS
Excluding events with M(pπ⁺) in N* band.
30
20
10
NO. OF COMBINATIONS / 50 MEV
0·6
0·8
1·0
1·2
1·4
1·6
1·8
M (K⁰ π⁺) GEV

FIG. 63 DISTRIBUTION OF $M(\bar{K}^0\pi^0)$

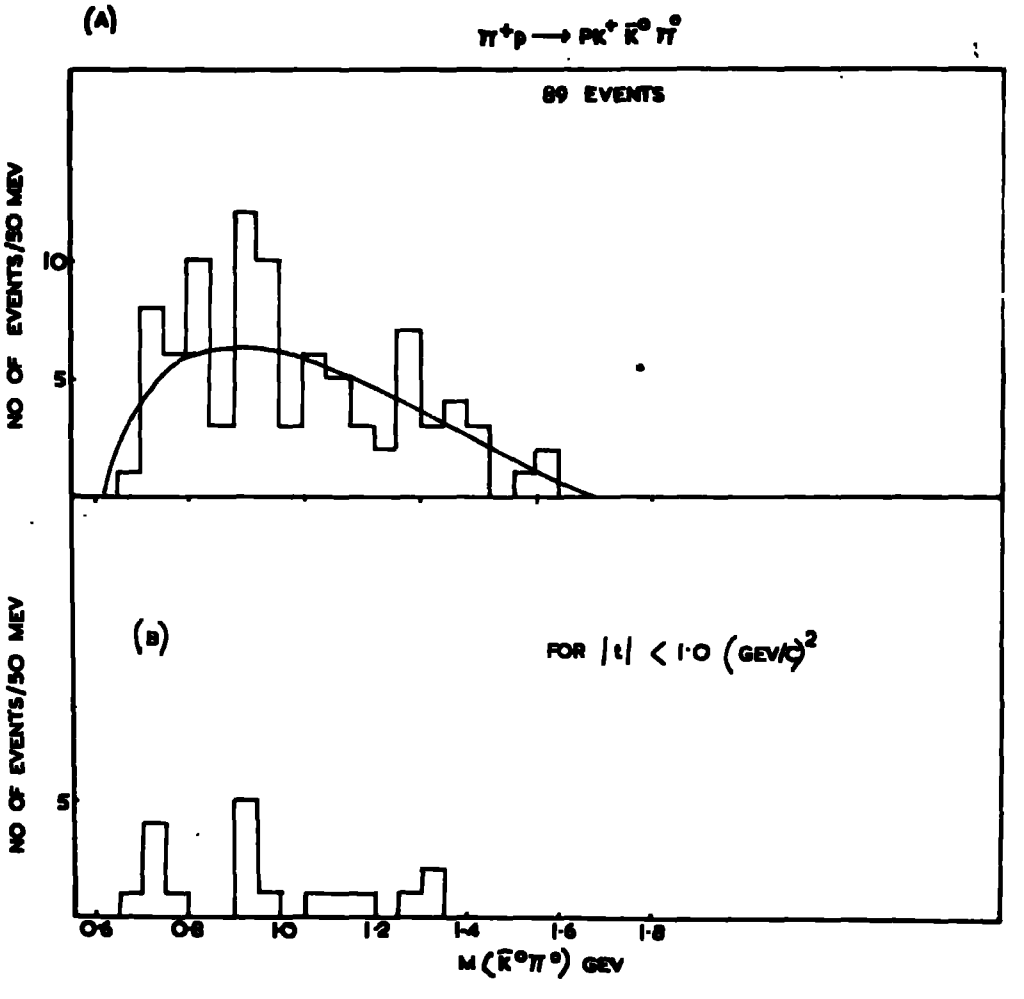

If the Kappa is considered as a real resonance with isospin of $I = \frac{1}{2}$ (i.e. the same as the K^*) then from isospin consideration it is expected that the Kappa (as well as the K^*) should be produced in the channels $P\pi^+K^+K^-$ and $PK^+\bar{K}^0\pi^0$ with a frequency of 2 to 1. Therefore, for comparison, the $\bar{K}^0\pi^0$ effective mass distribution is shown for the channel $PK^+\bar{K}^0\pi^0$ in figure 63(A). The distribution in figure 63(B) corresponds to a cut in the square four-momentum transfer of $|t| < 1.0$ GeV^2. From figure 63(A) the cross-section for the production of the $K^{*o}(890)$ is estimated to be

$$\sigma(K^{*o} \rightarrow K^-\pi^+) = (6 \pm 3)\mu b$$

corresponding to (5 ± 2) events. Twice this cross-section is in good agreement with the value

$$\sigma(K^{*o} \rightarrow K^-\pi^+) = (13 \pm 3)\mu b$$

obtained for the $P\pi^+K^+K^-$ channel.

The relative number of events in the Kappa region as seen in figure 60(a) and figure 63(A) for the two channels is within the large statistical error also compatible with the expected branching ratio. Thus it appears that the Kappa production is observed in the $P\pi^+K^+K^-$ channel

(iv) Production of the $\Phi(1019)$ meson

The conclusive evidence for the $\Phi(1019)$ meson was given by Connolly et al, (1963) in the K^-P experiment at 2.24 and 2.5 GeV/c. By analysing the channels $K^-P \rightarrow \Lambda K^0\bar{K}^0$ and $K^-P \rightarrow \Lambda K^+K^-$ they observed

an enhancement in the $K\bar{K}$ mass distribution. That the observed enhancement, though produced so close to the threshold was a resonance and not an effect of a final state $K\bar{K}$ scattering was proved by the authors who also determined the ~~quantum~~ quantum numbers of the Φ. From the observed branching ratios of the decay modes, the C-parity of the Φ was determined to be -1.

For a neutral $K^{o}\bar{K}^{o}$ system, the charge conjugation parity C and the space parity P are related as

$$C = P = (-1)^{\ell}$$

A C = -1 assignment for the Φ produced in the $K^{o}\bar{K}^{o}$ channel allows the decay mode $\Phi \rightarrow K_1K_2$ only and forbids $\Phi \rightarrow K_1K_1$ or K_2K_2 (Matthews, 1963). The production of the $\Phi(1019)$ meson in the $K^{o}\bar{K}^{o}$ and $K^{+}K^{-}$ channels in the present analysis is described below.

$K^{o}\bar{K}^{o}$ Channel

Figure 64(a) shows the two dimensional scatter plot M ($P\pi^{+}$) versus M($K^{o}\bar{K}^{o}$) for the channel $P\pi^{+}K^{o}\bar{K}^{o}$ and figure 64(b) shows the projection on the M($K^{o}\bar{K}^{o}$) axis. The shaded area in the $K^{o}\bar{K}^{o}$ effective mass distribution corresponds to those events in which only one K^{o} is seen to decay in the chamber. The Φ is seen to be produced with little background in the shaded histogram. The nature of the distributions show that the background estimation under the Φ peak is uncertain to a large extent. An estimated excess of the number of events is (5 ± 3) above the phase space curve. This curve has been normalised to the number of events outside the peak region for

FIG. 64

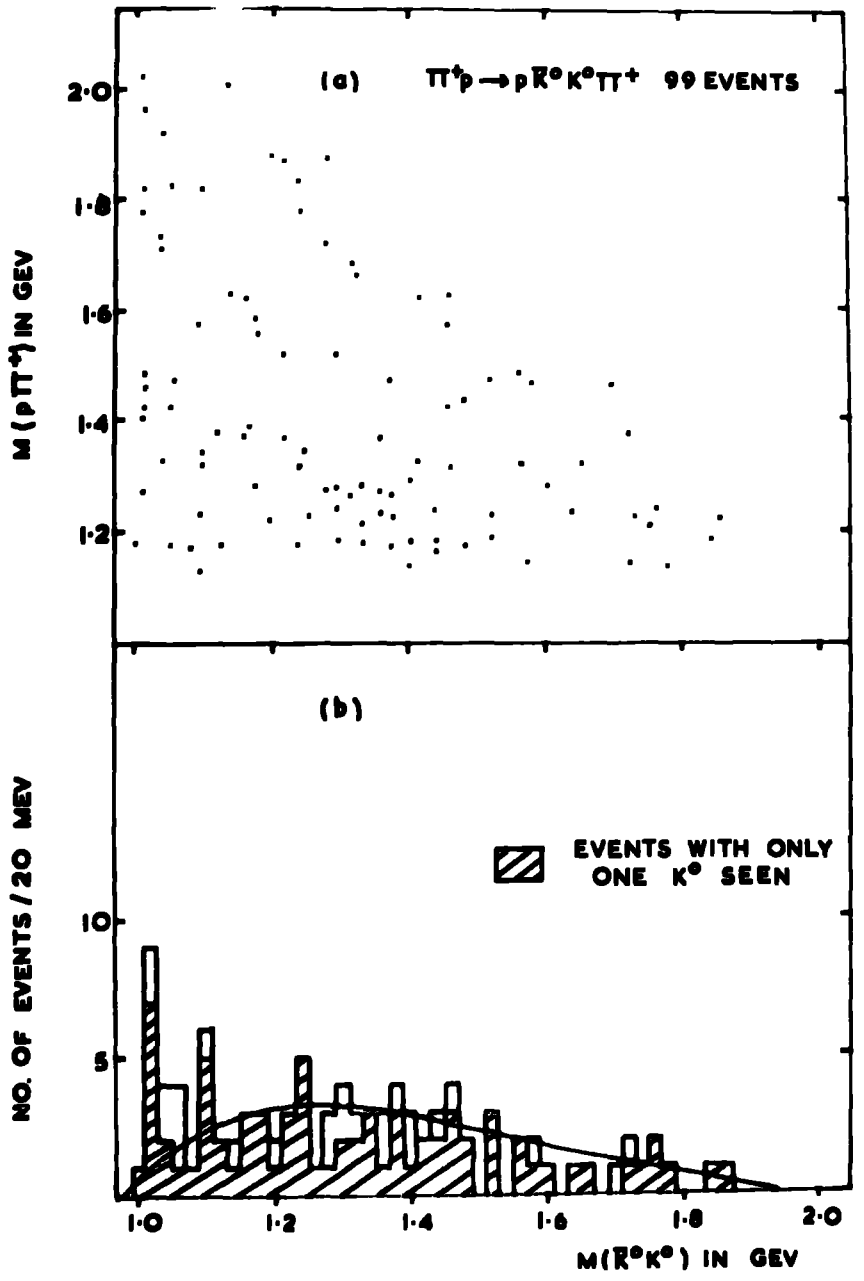
(a) $\pi^+p \rightarrow p\bar{K}^0K^0\pi\pi^+$ 99 EVENTS
2·0
1·8
1·6
1·4
1·2
M(pπ⁺) IN GEV
(b)
EVENTS WITH ONLY ONE K⁰ SEEN
10
5
NO. OF EVENTS/20 MEV
1·0
1·2
1·4
1·6
1·8
2·0
M($\bar{K}^0K^0$) IN GEV

the unshaded histogram. The corresponding cross-section for production of the Φ is $(3 \pm 2)\mu b$ for events of the K_1K_2 type.

K^+K^- Channel

Figure 65(a) shows the two dimensional scatter plot $M(P\pi^+)$ versus $M(K^+K^-)$ for the $P\pi^+K^+K^-$ channel. The projection for the K^+K^- effective mass is shown in figure 65(b) in which a narrow peak indicating the production of $\Phi(1019)$ is observed. The partial cross-section for the Φ in this channel has been determined to be $\sigma(\Phi \rightarrow K^+K^-) = (4 \pm 2)\ \mu b$. The total cross-section for the reaction $\pi^+P \rightarrow P\pi^+\Phi$ with the Φ decaying into K_1K_2 or K^+K^- is determined to be

$$\sigma\ (\Phi \rightarrow K\bar{K}) = (7 \pm 3)\mu b.$$

Since both the $N^{*++}(1236)$ and $\Phi(1019)$ are seen to be produced in the $K^0\bar{K}^0$ and K^+K^- channels an indication for the quasi two-body reaction $\pi^+P \rightarrow N^{*++}\Phi$ was looked for. The scatter plots in figure 64(a) and figures 65(a) do not give any indication that the Φ is produced preferentially in the N^* band. One can only estimate an upper limit of the cross-section. The upper limit to the cross-section of a resonance is defined as the value obtained by taking twice the square root of the number of events in the mass region of the resonance and which corresponds approximately to a 95% confidence limit. On this basis the upper limit of the cross-section for the double resonance $N^{*++}\Phi$ is estimated to be

$$\sigma\ (N^{*++}\Phi) < 3\ \mu b.$$

FIG. 65

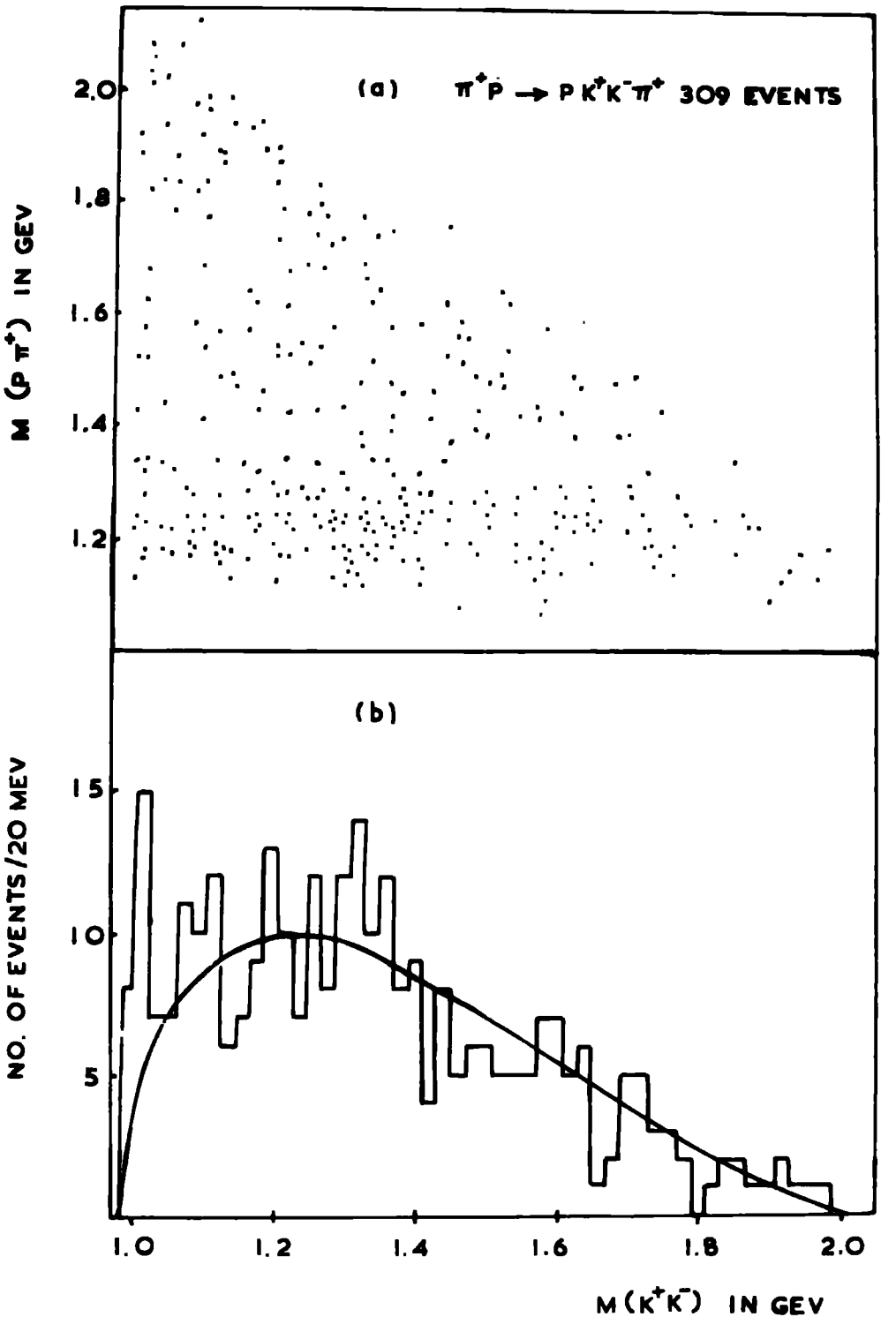
(a) $\pi^+ p \rightarrow p K^+ K^- \pi^+$ 309 EVENTS
M ($p\pi^+$) IN GEV
2.0
1.8
1.6
1.4
1.2
(b)
NO. OF EVENTS/20 MEV
15
10
5
1.0
1.2
1.4
1.6
1.8
2.0
M(K^+K^-) IN GEV

This value may be compared with the upper limit of 4 μb which has been quoted for this process in the 8 GeV/c π^+P experiment (Brandt et al, 1966).

(v) Production of the Y_o^* (1520)

In the $P\pi^+K^+K^-$ channel the Y_o^* (1520) is observed in the PK^- effective mass distribution shown in figure 66. The shaded area in the figure corresponds to a cut in the squared four-momentum transfer of $|t| < 1.0$ (GeV/c)^2. The figure shows that most of the $Y_o^*(1520)$ is produced at low momentum transfer. The cross-section has been determined to be

$$\sigma\ (Y_o^* \rightarrow PK^-) \ = \ (11 \pm 3)\ \mu b.$$

Except for statistically insignificant enhancements at their expected mass value the $Y_1^*(1660)$ and $Y_1^*(1765)$ which are known to exist have not been seen in the PK^o or $P\bar{K}^o$ effective mass distributions of the channels $P\pi^+K^o\bar{K}^o$ and $PK^+\bar{K}^o\pi^o$.

The cross-sections of the observed resonances in the various $K\bar{K}$ channels are listed in Table 12.

FIG. 66

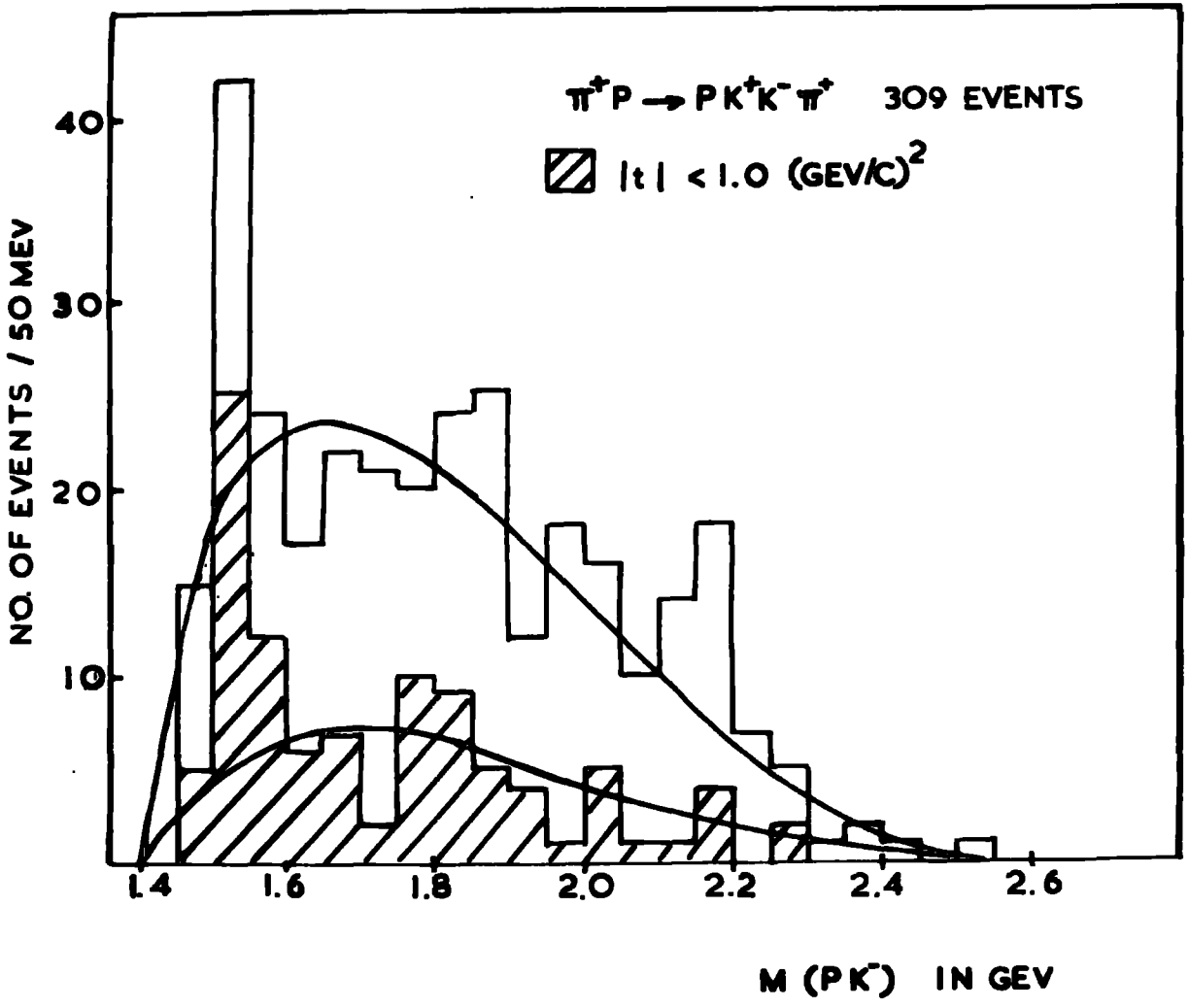
$\pi^+ P \rightarrow P K^+ K^- \pi^+$ 309 EVENTS
$|t| < 1.0$ (GEV/C)^2
NO. OF EVENTS / 50 MEV
40
30
20
10
1.4
1.6
1.8
2.0
2.2
2.4
2.6
M (PK^-) IN GEV

TABLE 12

Cross-sections of Resonance Production in $K\bar{K}$ Channels

Channel	Reaction	Cross-section (μb)
$PK^+\bar{K}^0$	$\pi^+P \rightarrow P\,A_2^+$ $\hookrightarrow K^+\bar{K}^0$	11±6
$PK^0\bar{K}^0\pi^+$	$\pi^+P \rightarrow N^{*++}(1236)\;K^0\bar{K}^0$ $\hookrightarrow P\pi^+$	16±4
	$\pi^+P \rightarrow PK^0K^{*+}(890)$ $\hookrightarrow K^0\pi^+$	17±5
	$\pi^+P \rightarrow P\pi^+\phi$ $\hookrightarrow K_1^0K_2^0$	3±2
$P\pi^+K^+K^-$	$\pi^+P \rightarrow N^{*++}(1236)\;K^+K^-$ $\hookrightarrow P\pi^+$	41±10
	$\pi^+P \rightarrow PK^+\bar{K}^{*0}(890)$ $\hookrightarrow K^-\pi^+$	13±3
	$\pi^+P \rightarrow Y^{*0}(1520)\;K^+\pi^+$ $\hookrightarrow PK^-$	11±3
	$\pi^+P \rightarrow P\pi^+\phi$ $\hookrightarrow K^+K^-$	4±2

CONCLUSION

In this thesis an account has been given of the production of resonances in the following channels of 5 Gev/c π^+p interactions:

(a) $\pi^+p \rightarrow p\pi^+\pi^+\pi^-$

(b) $\pi^+p \rightarrow p\pi^+\pi^+\pi^-\pi^o$

(c) $\pi^+p \rightarrow p\pi^+K^+K^-$

(d) $\pi^+p \rightarrow$ 2-prong + 1 or 2 visible V^o decays.

In channel (a) a strong production of the $N^{*++}(1236)$, ρ^o and a significant amount of the f^o and A_2^+ mesons are observed. The A_1 signal is not detected in this analysis. Asymmetry is observed in the decay of the f^o.

In channel (b) besides a strong production of the $N^{*++}(1236)$ and ω^o, the ρ meson in its three charged modes, the $A_2^o \rightarrow \rho\pi$, $A_2^+ \rightarrow \eta\pi^+$ and the $B^+ \rightarrow \omega\pi^+$ are also observed. The fact that the B^+ signal is improved when selecting events corresponding to its large decay angles (i.e. $|\cos\theta_\omega| < 0.5$) supports the assumption that the ω and π are in a relative s-state.

In channels (a) and (b) there are significant contributions of the quasi two body states $\pi^+p \rightarrow N^{*++}\rho^o$, $\pi^+p \rightarrow N^{*++}\omega^o$ and $\pi^+p \rightarrow N^{*++}\eta^o$. The strong peripheral nature of these reactions should make it possible to obtain a pure sample of each in order to study the predictions of a theoretical model such as the absorption model. This model has met with some success in interpreting the first two of the above reactions in the 8 Gev/c π^+p experiment

(A-B-C Collaboration, 1966).

The relative cross-sections of the $A_2^o \rightarrow \rho^{\pm}\pi^{\mp}$ and $A_2^+ \rightarrow \rho^o\pi^+$ which are observed are in agreement with the values expected from the assignment of isospin I = 1 for the A_2 meson. The decay branching ratios of the A_2 for its $\eta\pi$ and $K\bar{K}$ decay modes relative to the $\rho\pi$ decay mode are comparable with the values quoted by Rosenfield et al (1967).

In the strange particle channels (c) and (d) the calculated values of the cross-sections support the observed trend that the γK^+ cross-section is smaller than the $\gamma K\bar{K}$ cross-section (Brandt et al., 1966). The resonances observed in the various channels are the $N^{*++}(1236)$, $Y_1^*(1385)$, $K^*(890)$, $\Phi(1019)$ and $A_2 \rightarrow K\bar{K}$. Besides these the production of the $\kappa(730)$ is also observed. The $\frac{d\sigma}{d|t|}$ distributions of the two-body states $\pi^+P \rightarrow Y_1^{*+}(1385)\ K^+$ and $\pi^+P \rightarrow Y_1^{*+}(1385)\ K^{*+}(890)$ have been compared with the predictions of the absorption model as calculated by Eysel et al. (1967). The calculated and the experimental values are hardly in agreement with each other.

ACKNOWLEDGEMENTS

The author wishes to thank Professor G. D. Rochester for his encouragement and interest in the work. He wishes to thank his supervisor Dr. J. V. Major for his guidance and help throughout the work. He would also like to thank his colleagues in the High Energy Physics Group for their assistance with various stages of the work.

His thanks are due to the technical staff of the Physics Department, in particular to Mrs. E. Errington, Miss T. Jobling, Miss J. Watson, Miss C. Petch, Miss J. Bowey and Miss D. Richmond for their painstaking work in scanning and measuring the events. He would like to thank Mrs. J. Moore for her careful typing of this thesis.

The author wishes to thank his wife Halima for her constant encouragement during his long absence from her and the family.

Finally, he would like to thank the Government of East Pakistan, the Education Department in particular, for the grant of the scholarship and the deputation abroad.

REFERENCES

A-B-B-B-H-L-M Collaboration,

Physical Review, 138, B897 (1965).

A-B-B-H-M Collaboration,

Nuovo Cimento, IL 44A, 530 (1966).

A-B-C Collaboration,

Physics Letters, 12, 356 (1964).

Physics Letters, 19, 608 (1965).

Physics Letters, 22, 533 (1966).

Amaldi U., and Sellari, F.,

Nuovo Cimento, 31, 360 (1964).

Baltay, C., et al.,

Physics Letters, 25, 160 (1967).

Bartke, J.,

Nuclear Physics, 82, 673 (1966).

Brandt, S., et al.,

Physics Letters, 22, 230 (1966).

Briggs, G. A.,

Ph.D. Thesis, 1966, Durham University.

Burhop, E.H.S.,

Proceedings of 1962 Easter School for Physicists, CERN 63 - 3, 279 (1963).

Cason, N.M., et al.,

Physical Review Letters, 17, 838 (1966).

References continued

Chew, C.F., and Frautschi, S.C.,

Physical Review Letters, 7, 394 (1961).

CERN/TC/NBC, 63-2 (1963).,

The magnetic field of the British 1.5 m bubble chamber.

CERN/TC/NBC, 64-1 (1964),

Parameters of 1.5 m Hydrogen Bubble Chamber.

Cocconi, G., et al.,

Physical Review Letters, 7, 450 (1961)

Connolly et al.,

Physical Review Letters, 10, 371 (1963).

Eysel, F., et al.,

Z. F. Physik, 199, 411 (1967).

Fermi, E.,

Progress In Theoretical Physics (Japan), 5, 570 (1950).

Fleury et al.,

Observations of Nuclear Isobars in $\pi^+ d$ Interactions at 5 Gev/c - Contribution to International Heidelberg Conference (1967).

Hohler, G., et al.,

Physics Letters, 20, 79 (1966).

Jackson, J. D.,

Nuovo Cimento, 34, No. 6, 1644 (1964).

Reviews of Modern Physics, 37, 484 (1965).

References continued

Keil, E., and Neale, W. W.,

CERN/TC/02, 63-3 (1963).

Kellnar, G.,

CERN/TC/NBC, 65-4 (1965).

Kitchen, C. A.,

Ph.D. Thesis, 1967, Durham University.

Lichtenberg, D. B., and Williams, P.K.,

Physical Review, 139, B179 (1965).

Lynch, G.,

UCRL, 10335 (1962).

Maor, U.,

CERN/TC/Physics, 66-26, 9 (1966).

Maris, A., et al.,

Physics Letters, 11, 381 (1963).

Matthews, P.T.,

Brandeis Summer Institute In Theoretical Physics (1963), Vol. 1, Page 132.

Morrison, D.R.O.,

CERN/TC/Physics, 66-20 (1966).

Physics Letters, 25B, 238 (1967).

Peyrou, C.,

Proceedings of International Conference on Instrumentation for High Energy Physics, page 157, Berkeley (1960).

Phillips, R.J.N., and Rarita, W.,

Physical Review Letters, 15, 807 (1965).

Rosenfield, A.H., et al.,

Reviews of Modern Physics, 39, 1 (1967).

References continued

Schotanus, D.J.,

The Beam Momentum of the 5 Gev/c π^+P Experiment, HEN-33, Internal Report, Nijmegen.

Slattery, et al.,

Nuovo Cimento, IL 3, 377 (1967).

Svensson, B.E.Y.,

Nuovo Cimento, 37, 714 (1965).

Wagini, B.,

Diplomarbeit, Bonn (1967).

Welford, W. T.,

Applied Optics, 2, 981 (1963).